QUANTITATIVE IN VITRO AND IN VIVO CHARACTERIZATION OF NEAR INFRARED MOLECULAR IMAGING AGENTS FOR ENHANCED DISEASE DETECTION

By

SHELBY KATHERINE WYATT

Dissertation

Submitted to the Faculty of the
Graduate School of Vanderbilt University
in partial fulfillment of the requirements
for the degree of
DOCTOR OF PHILOSOPHY

in

Biomedical Engineering

May, 2007

Nashville, Tennessee

Approved by:

Darryl J. Bornhop

Todd D. Giorgio

John C. Gore

E. Duco Jansen

J. Oliver McInytre

ACKNOWLEDGEMENTS

The completion of this dissertation would not have been possible without the assistance of many people. I would first like to thank my PhD advisors, Dr. Darryl Bornhop and Dr. Todd Giorgio, for all of their guidance and support as well as the many incredible opportunities they have provided during my tenure as a graduate student. I would also like to thank Dr. John Gore, Dr. E. Duco Jansen and Dr. J. Oliver McIntyre for their participation on my PhD committee and their invaluable expertise. Over the past several years I have exploited their open door policies and have benefited greatly from their comments, questions, and overall guidance.

I would also like to thank the past and present members of the Bornhop and Giorgio laboratories for their assistance, friendship and support (both in terms of research and life in general). I would particularly like to thank Dr. H. Charles Manning, Mingfeng Bai, Stephanie Bailey and A. Coe Foutch for their significant contributions to this work. I would also like to specifically acknowledge Ashley Weiner (now PhD) for allowing me to complain and providing unending encouragement over the past several months as we finished our dissertations together. Congratulations!

A number of fruitful collaborations have truly inspired these projects. I thank the many talented scientists with whom I have had the pleasure to work, including Drs. Laura McIntosh, Pascal Gallant, and Guobin Ma from ART Advanced Research Technologies, Inc; Drs. J. Oliver McIntyre, Richard Whitesell, Al Powers, Todd Peterson, Ron Baldwin, M. Noor Tantaway, Reid Thompson, Moneeb Ehtesham, and Khubaib Mapara from Vanderbilt University. I'd also like to acknowledge the past and present members of the

VUIIS Center for Small Animal Imaging support staff including Jarrod True, Heather Scott and Jennifer Begtrup for their hard work as well as their selfless and kind demeanor; your assistance is very much appreciated.

This research would not have been possible without funding support from ART Advanced Research Technologies, Inc., the Department of Defense, the National Science Foundation, and the National Institutes of Health.

There are a number of friends inside and outside of Vanderbilt University and VUIIS as well as from my undergraduate career at Johns Hopkins University that have provided a social outlet, priceless friendships, and constant support. You've been there for me through good times and bad and for that I am truly grateful.

I would like to specifically thank Tuhin Sinha for his motivation, endless encouragement, and support, particularly over the past year and a half. Your friendship, sense of humor, and amazing outlook have certainly influenced my life.

And, finally, I must acknowledge the incredible members of my family, especially my parents Tom and Beany, my sister Jessica and my grandparents Peggy, Jr. and Jenny. I would not be the person that I am today without the unconditional love, encouragement, inspiration, support, advice, understanding, and friendship that you have provided throughout my entire life. You mean more to me than you will ever know.

TABLE OF CONTENTS

LIST OF FIGURES

LIST OF TABLES

NOMENCLATURE

ALA	5-aminolevulinic acid
ANOVA	analysis of variance
BBB	blood brain barrier
CMF-PBS	calcium- and magnesium-free phosphate buffered saline
CT	computer tomography
ctH_2O	concentration of water in the tissue
ctHHb	concentration of deoxy-hemoglobin in the tissue
DMEM	Dulbecco’s Modified Eagle Medium
DMSO	dimethylsulfoxide
DNA	deoxyribonucleic acid
DOS	diffuse optical spectroscopy
DOT	diffuse optical tomography
Eu^{3+}	europium
EGF	epidermal growth factor
EGFr	epidermal growth factor receptor
EPR	enhanced permeability and retention
FBS	fetal bovine serum
FDA	Food and Drug Administration
^{18}FDG	2-[^{18}F]fluoro-2deoxy-D-glucose
FOV	field of view
Gd^{3+}	gadolinium

H&E	hematoxylin and eosin
Hb	deoxyhemoglobin
HbO_2	oxyhemoglobin
H_2O	water
HPLC	high performance liquid chromatography
ICG	indocyanine green
iCT	intraoperative computed tomography
iMRI	intraoperative magnetic resonance imaging
iUS	intraoperative ultrasound
Ln	lanthanide
MAP	maximum a posteriori
MI	molecular imaging
MR	magnetic resonance
MRI	magnetic resonance imaging
MS	mass spectrometry
NHS	N-hydroxysuccinimide
NIR	near infrared
NMR	nuclear magnetic resonance
OR	operating room
PBR	peripheral benzodiazepine receptor
PET	positron emission tomography
pi	post-injection
Qdots	quantum dots

RNA	ribonucleic acid
ROI	region of interest
SPECT	single photon emission computed tomography
TOI	tissue optical index
TPSF	temporal point spread function
UV	ultraviolet
μ_a	absorption coefficient
$\mu_s^{'}$	reduced scattering coefficient

CHAPTER I

INTRODUCTION

Objectives

The emerging field of molecular imaging (MI) aims to noninvasively, quantitatively and repetitively monitor biological processes *in vivo* to detect disease, probe its basis, and study relevant biochemical pathways at the molecular level. Since molecular targets (including cell surface and intracellular receptors, proteins, enzymes, DNA and RNA) undergo alterations prior to morphological or physical transformations, MI should aid in early detection and improved diagnosis of disease. The use of MI may therefore result in improved clinical outcomes and enhanced long-term patient survival. In addition, the capability to monitor lesion physiology *in vivo* allows further characterization of disease, which may facilitate therapeutic efficacy monitoring, speed drug discovery, and potentially lead to patient-specific treatment regimens. Recently, the ability to specifically label tumor cells has allowed enhanced tumor margin definition and surgical resection guidance.

Optical MI, particularly in the near infrared (NIR) wavelength region, is an inexpensive technique that provides relatively high sensitivity without the use of ionizing radiation. Fluorescence imaging is rapid, allowing for dynamic, real-time monitoring of agent biodistribution and clearance profiles and is commonly performed concurrently on multiple animals in a relatively high-throughput manner. In addition, the use of multiple bandpass filters or a liquid crystal tunable filter allows spectral discrimination and the ability to sequentially monitor multiple optical reporters at different wavelengths. Although typical *in vivo* optical imaging performed at the anatomical scale tends to suffer from relatively low spatial resolution, photon penetration can be long when working in the NIR tissue transparency window (λ ~ 650-900 nm). Here, photon absorption by hemoglobin and water is low, scattering is reduced and tissue autofluorescence is minimal, allowing photons to interrogate as much as centimeters of tissue.

The ultimate success of optical MI is depends on the development, characterization and optimization of probes as well as superior instrumentation to accurately detect, localize and quantify these unique MI compounds. The objectives of this dissertation were directed at quantitative *in vitro* and *in vivo* evaluation of two novel MI probes developed in our laboratory: the peripheral benzodiazepine receptor (PBR)-targeted NIR MI agent (NIR-conPK11195) and a potential optical analogue to the 2-[^{18}F]fluoro-2deoxy-D-glucose (^{18}FDG) positron emission tomography (PET) agent, NIR-glucosamine.

Specific Aims

Specific Aim 1: Determine the utility of using a peripheral benzodiazepine receptor-targeted near infrared molecular imaging agent, NIR-conPK11195, for screening a pre-clinical model of breast cancer

The peripheral benzodiazepine receptor (PBR) represents an attractive target for MI due to its overexpression in a variety of neurodegenerative diseases and cancers, including breast cancer. Clinically, the expression of PBR appears to correlate with disease stage, aggressive phenotype and clinical prognosis. Capitalizing on this expression profile and the low absorption and increased photon penetration depth in the NIR tissue transparency window, our laboratory has developed a PBR-targeted NIR MI agent (NIR-conPK11195). The quantitative evaluation of the *in vitro* and *in vivo* uptake of NIR-conPK11195 in a human metastatic breast adenocarcinoma (MDA-MB-231) model of breast cancer is presented in Chapter III.

Specific Aim 2: Evaluate the applicability of using a lanthanide chelate-based PBR-targeted molecular imaging probe (Eu^{3+}-conPK11195) as a topical agent for brain tumor demarcation and a PBR-targeted near infrared molecular imaging agent (NIR-conPK11195) to study breast cancer metastases to the brain

Both primary brain tumors and secondary brain metastases are often treated by maximum surgical resection followed by chemotherapy and/or radiation. The extent of surgical resection has been shown to correlate with improved clinical prognosis, increased time to recurrence and overall patient survival. However, the degree of surgical resection is often compromised due to difficulties in accurately determining tumor location and ill-defined tumor boundaries as well as the desire to preserve eloquent brain tissue. In an effort to overcome some of the limitations of the commonly used image-guided surgery techniques, two PBR-targeted MI agents (Eu^{3+}-conPK11195 and NIR-conPK11195) were assessed for their applicability to aid in primary brain tumor demarcation and the study of brain metastases, respectively. These observations are reported in Chapter IV.

Specific Aim 3: Determine if a NIR-labeled glucosamine derivative has the potential to serve as an optical analogue to the 2-[^{18}F]fluoro-2deoxy-D-glucose (^{18}FDG) positron emission tomography (PET) agent

While 2-[^{18}F]fluoro-2-deoxy-D-glucose (^{18}FDG) positron emission tomography (PET) has inherently high sensitivity and demonstrated clinical applicability, the imaging technique has several limitations. These drawbacks include the exposure to ionizing radiation, difficulty of compound synthesis, requirement of a local cyclotron, short halflife of ^{18}F (110 minutes) and relatively low spatial resolution. In an attempt to overcome some of the major limitations of PET, our laboratory and others have developed potential optical analogues of ^{18}FDG. Chapter V presents the quantitative *in vitro* and *in vivo* assessment of NIR-glucosamine in an SW480 mouse model of human colorectal adenocarcinoma.

CHAPTER II

BACKGROUND AND SIGNIFICANCE

Cancer: Early Detection Improves Clinical Outcome and Patient Survival

The American Cancer Society estimates that approximately 559,650 Americans will die from cancer in 2007, representing the second leading cause of death in the United States (1). In addition, another 1,444,920 new cancer diagnoses are expected this year alone (1). Since treatment is more likely to be successful if initiated in the early stages of cancer, clinical outcomes could be improved by using novel strategies aimed at detecting initial cellular and molecular changes prior to the development of tumor-related symptoms or palpable tumor mass.

Molecular Imaging

The emerging field of molecular imaging (MI) aims to noninvasively, quantitatively and repetitively monitor biological processes *in vivo* to detect disease, probe its basis, and study relevant biochemical pathways at the molecular level (2). Since molecular targets (including cell surface and intracellular receptors, proteins, enzymes, DNA and RNA) undergo alterations prior to morphological or physical transformations, MI should aid in early detection and improved diagnosis of disease (2-4). The use of MI may therefore result in improved clinical outcomes and enhanced long-term patient survival. In addition, the capability to monitor lesion physiology *in vivo* allows further characterization of disease, which may facilitate therapeutic efficacy monitoring, speed drug discovery, and potentially lead to patient-specific treatment regimens. Recently, the ability to specifically label tumor cells by MI has provided enhanced tumor margin definition and surgical resection guidance (5).

Although a number of potential MI modalities exist; nuclear imaging, magnetic resonance imaging (MRI), and optical imaging represent the three major MI techniques currently in use (2, 4, 6-9). These imaging techniques differ in a variety of ways, including sensitivity, spatial and temporal resolution, penetration depth, exploited energies (ionizing or non-ionizing), throughput, cost, and availability of injectable and biocompatible molecular probes [reviewed in (4, 6)].

Radionuclide Imaging

Nuclear MI techniques rely on the production of two or a single γ-ray from radioisotope decay. The detection of these γ-rays is achieved by positron emission tomography (PET) or single photon emission computed tomography (SPECT), respectively (4). PET requires the labeling of molecules with a positron-emitting isotope, such as ^{18}F, ^{11}C, ^{13}N, ^{15}O, ^{68}Ga, or ^{64}Cu. The emitted positron annihilates with an electron, producing two 511 keV photon γ-rays ~180° apart, which are then detected by a cylindrical ring of scintillation crystals. The ability to detect coincident photons eliminates the need for collimation to determine direction of flight and original location and ultimately allows for quantitative distribution measurements. Conversely, SPECT utilizes γ-emitting isotopes, such as ^{99m}Tc, ^{111}In, ^{123}I, which emit a single high-energy photon, ranging from 70 to 400 keV (4). The detection of a single photon in SPECT imaging, rather than two coincident photons in PET, requires physical, geometric collimation to determine location and does not allow for full quantification of reporter concentration. However, γ-emitting isotopes are more readily available than positron-emitting isotopes and typically have longer half-lifes ($t_{1/2}$ = hours to days) than PET labels (ex. $t_{1/2}$ of ^{18}F = 110 minutes) (6, 8). Additionally, SPECT radioisotopes enable simultaneous detection of multiple probes with different γ-ray energies, whereas positron-emitting isotopes all generate photons of equivalent energy (511 keV). Both PET and SPECT suffer from the disadvantage of exposure to ionizing radiation.

The sensitivity of PET is on the order of 10^{-11} to 10^{-12} M, regardless of reporter probe depth since the depth of γ-ray penetration is virtually unlimited (6, 8). The spatial resolution of most clinical PET scanners is approximately $(6\text{-}8)^3$ mm^3, whereas typical microPET scanners have a spatial resolution of approximately 2^3 mm^3 (6, 8). The time required to collect enough information to produce a PET image is typically seconds to minutes.

SPECT sensitivity is an order of magnitude poorer than PET due to the absorption of photons by the mechanical collimator and is on the order of 10^{-10} to 10^{-11} M (6, 8). Although there is a fundamental tradeoff between sensitivity and spatial resolution when designing the collimator, the spatial resolution of SPECT typically ranges from 1 to 2 mm (6, 8). Similar to PET, the time needed to acquire a useful image using SPECT is on the order of minutes.

Magnetic Resonance Imaging

Magnetic resonance imaging (MRI) is based on the principle that unpaired nuclear spins, or magnetic dipoles, align themselves when exposed to a strong magnetic field. These magnetic dipoles subsequently return to their original orientation following perturbation by a radiofrequency pulse. The change in electromagnetic flux is detected by the radiofrequency coil, which is then converted to a rate of relaxation by the MR scanner. This rate of relaxation varies in different environments, producing different MR signals, and ultimately resulting in image contrast. Exogenous agents based on paramagnetic and superparamagnetic metal cations can be used to enhance MR contrast in tissue by influencing proton relaxation rates (6, 10, 11).

The spatial resolution of MRI (10-100 μm for small animals to mm for humans) and the ability to simultaneously obtain both molecular and anatomical information are clear advantages over radionuclide and optical imaging modalities (4, 6). However, the sensitivity of MRI (mM to μM) is several orders of magnitude less than both radionuclide and optical imaging (pM to nM). Thus, significantly larger quantities of injected molecular probes or much longer scan times are typically necessary to acquire an image with reasonable signal to noise. Other disadvantages of MRI include the relatively high cost and complexity of MR scanners, particularly when compared to optical imaging.

Optical Molecular Imaging

Optical information may be obtained from endogenous tissue contrast (12-20), bioluminescence (21-25) or exogenous fluorescent MI probes using a variety of optical imaging technologies (26, 27). These optical techniques either exploit light interaction with tissue (absorption, scattering, photon transmission or reflectance) or measure photon emission (fluorescence or (bio)luminescence) (27, 28).

Endogenous tissue contrast results from one of three processes: absorption, scattering, or autofluorescence. Since oxyhemoglobin, deoxyhemoglobin and water are primarily responsible for the absorption of photons in tissue, measuring the absorption coefficient at specific wavelengths allows for quantification of hemoglobin and water concentration and ultimately provides information about vascularization, perfusion, and hypoxia (12-16). Elastic scattering measurements provide alternative information, specifically regarding tissue structure, intracellular composition, and organelle concentration (14, 15), while inelastic scattering information provides a biochemical "fingerprint" (17). Finally, autofluorescence results from specific endogenous fluorophores including nicotinamide (NAD[H]), flavins, collagen, and elastin (18-20). The concentration of these compounds varies with disease progression, resulting in a measurable spectroscopic change. However, autofluorescence techniques suffer from a lack of specificity and relatively low signal-to-noise ratios due to small fluorophore concentrations as well as high scattering and reflection backgrounds (26). In addition, the quantification of these measurements is hindered by the tissue absorption and scattering of both the excitation and emitted light.

Bioluminescence represents another form of optical imaging, which measures the photon emission from cells that have been genetically modified to express luciferases. A number of luciferase genes exist and even more have been genetically engineered, allowing for spectrally-shifted, multi-reporter tracking (21-24). In general, the energy-dependent, enzymatic reaction between luciferase enzymes and their substrates results in photon emission between 480 and 670 nm (21, 24).

Bioluminescence differs from fluorescence in that the photon emission results from an oxidation/reduction reaction rather than from exposure to excitation light. Because the bioluminescent signal originates from a specific enzyme-substrate interaction, combined with the fact that mammalian tissue does not autoluminesce, the emitted light is essentially background free (6, 8). Although this minimal background level results in a high SNR and allows for detection of significantly lower signals, bioluminescence imaging suffers from low photon penetration depth in tissue (1-2 cm) due to significant photon absorption and scattering. This depth limitation is also a factor in fluorescence imaging. However, the photon penetration depth can be significantly improved by working in the near infrared (NIR) tissue transparency window ($\lambda \sim 650$ – 900 nm (29); discussed below).

Bioluminescence also suffers from low spatial resolution and the unlikelihood of clinical translation due to the required transgenic modification of cells, the difficulty to measure deep in tissue, and the high cost of substrate. However, the ease, speed and high-throughput of operation make bioluminescence highly suitable for evaluating pre-clinical animal models, specifically for noninvasive imaging of tumors, cell trafficking, monitoring of gene expression, and monitoring of tumor growth or regression following treatment (6, 22, 23, 25).

Fluorescence MI, particularly in the near infrared (NIR) wavelength region, is an inexpensive technique that provides relatively high sensitivity without the use of ionizing radiation (4, 27). Fluorescence imaging is rapid, allowing for dynamic, real-time monitoring of agent biodistribution and clearance profiles and is commonly performed concurrently on multiple animals in a relatively high-throughput manner. In addition, the use of multiple bandpass filters or a liquid crystal tunable filter allows spectral discrimination and the ability to sequentially monitor multiple optical reporters at different wavelengths (30). Although optical imaging suffers from relatively low spatial resolution, photon penetration can be long when working in the NIR tissue transparency window [$\lambda \sim 650\text{-}900$ nm] (29). Here, photon absorption by hemoglobin and water is low, scattering is reduced and tissue autofluorescence is minimal, allowing photons to interrogate as much as centimeters of tissue (29, 31).

Fluorescence MI techniques typically utilize exogenous fluorescent probes, which fall into one of three categories: non-specific, targeted, or “smart”/activatable (26, 27, 32). Non-specific or non-targeted probes represent the most common contrast agents. These agents reveal varied compartmental distribution, providing information related to physiological processes such as changes in blood volume, perfusion, permeability and blood flow (4, 11). However, since these changes typically occur fairly late in the progression of disease, probes that are cellularly- or molecularly-targeted may provide earlier disease detection.

Targeted MI probes provide molecular specificity by combining a signaling moiety (ex. fluorophore) with a targeting functionality such as a ligand, peptide, antibody, sugar or other small molecule (26, 33-35). These targeted agents can be further characterized as direct binding and indirect binding probes. Direct binding probes include antibody and receptor ligand-based probes that bind stoichiometrically to their targets, while indirect binding probes measure the target enzyme activity.

Molecular specificity can also be achieved with activatable or “smart” probes (26, 32, 36). These agents are normally quiet, not producing an observable fluorescence signal, until activated by a specific enzyme target. The signal-to-noise ratio is therefore increased relative to other targeted MI probes, which provide a signal regardless of target interaction.

The ultimate success of optical MI depends on the development, characterization and optimization of probes as well as superior instrumentation to accurately detect, localize and quantify these unique MI compounds. The objectives of this dissertation were directed at quantitative *in vitro* and *in vivo* evaluation of two novel MI probes developed in our laboratory: the peripheral benzodiazepine receptor (PBR)-targeted NIR MI agent (NIR-conPK11195) and a potential optical analogue to the 2-[^{18}F]fluoro-2deoxy-D-glucose (^{18}FDG) positron emission tomography (PET) agent, NIR-glucosamine. The significance and a brief review of the literature are provided below for each of the specific aims.

Breast Cancer: Significance

Breast cancer represents the most frequently diagnosed cancer in women and the second most common cancer type responsible for women's deaths (1). In 2006, the American Cancer Society estimated that 212,920 women and 1,720 men would be newly diagnosed with breast cancer in the United States alone, while another 40,970 women and 460 men were expected to die from breast cancer (1). However, the five-year survival rate surpasses 95% if breast cancer is detected in its early stages (1, 37).

Typical Breast Cancer Detection Methods

X-ray mammography is currently the most common and most effective breast cancer screening technique (38). However, x-ray mammography has limited success in the case of younger women and women on hormone replacement therapies due to denser breast tissue. In fact, the sensitivity and specificity of x-ray mammography in women with extremely dense breasts is only 63% and 89%, respectively, compared to 87% and 97% in women with fattier breast tissue (39). In addition, x-ray mammography requires breast compression and employs ionizing radiation.

The use of MRI for breast cancer diagnosis has been explored, but is not approved for breast cancer screening by the US Food and Drug Administration (FDA) (38). Although most of the investigations involve small patient numbers and typically only include high risk women, the sensitivity of MRI appears to be consistently greater than both x-ray mammography and ultrasound [reviewed in (38)]. MRI does, however, demonstrate relatively lower specificity than x-ray mammography and is limited by its high cost and longer imaging times (38).

Ultrasound has played a more pivotal role in the discrimination between cysts and solid lesions, than in breast cancer screening (38). The use of ultrasound to delineate benign from malignant tumors has also been demonstrated (40). However, breast cancer detection using ultrasound is limited by the difficulties in image interpretation and the inability to consistently detect microcalcifications (38).

Optical Breast Cancer Detection Methods

NIR methodologies for breast cancer screening have also been explored (12, 14, 15, 34, 41). The optical imaging techniques are typically rapid, noninvasive, inexpensive, relatively sensitive, and not limited by mammographic density. Several of these techniques exploit intrinsic contrast mechanisms (12, 14, 15), while others obtain contrast through exogenous fluorescent contrast agents (34, 41).

Time-Domain Optical Mammography

Advanced Research Technologies' Softscan platform is a four-wavelength time domain optical imaging system that measures NIR parameters related to the main breast components (water, lipids, and deoxy- and oxy-hemoglobin) (15). Diffuse optical spectroscopy (DOS) and diffuse optical tomography (DOT) algorithms are used to analyze the temporal data and determine the absorption (μ_a) and reduced scattering (μ_s') coefficients. The physiologic properties of breast tissue are described by μ_a, which enables quantification of oxyhemoglobin (HbO_2), deoxyhemoglobin (Hb) and water (H_2O) concentration. The structural properties of breast tissue are described by μ_s, which allows estimation of the scattering amplitude (a) and scattering power (b). From these parameters, the total hemoglobin content ($HbT = HbO_2 + Hb$), the tissue hemoglobin oxygen relative saturation ($StO_2 = HbO_2/HbT$), and lipid percentage ($Li = -0.50 \times b + 0.90$) can be approximated.

To demonstrate the Softscan's ability to describe breast composition and differentiate between benign and malignant tumors, ART performed a pilot study including 49 pre- and post-menopausal women of various demographics (15). First, the bulk optical and physiologic properties of normal breast tissue were determined to be within expected physiologic range, in agreement with published results, and consistent with demographic trends. Next, the detection and characterization of breast tumors was evaluated in 11 malignant and 12 benign tumor cases. Combined, the benign and malignant tumors both exhibited a significantly higher blood volume and water content than the surrounding normal tissue, as expected from increased angiogenesis (Hb), edema (H_2O) and cellularity (H_2O). However, the diseased tissues were not discriminated from normal breast based on oxygen saturation. When stratified into benign and malignant pathologies, additional differences became apparent. The total hemoglobin contrast ratio between the suspicious lesion and the surrounding normal tissue was greater in the malignant population than in the benign population. This contrast is even more pronounced and statistically significant for deoxyhemoglobin alone.

Frequency-Domain Photon Migration and Steady-State Tissue Spectroscopy

Tromberg and colleagues also measure intrinsic optical properties of breast tissue in the NIR wavelength region by combining frequency-domain photon migration and continuous wave tissue spectroscopy in an attempt to distinguish between diseased and normal tissue (12, 14). Their broadband DOS measurements provide complete spectral information from 650 to 1,000 nm and potentially more accurate concentration determinations than the Softscan, which only measures optical properties at four distinct wavelengths (14, 15). In addition, the authors developed the tissue optical index (TOI) to monitor response to chemotherapy; TOI = (ctHHb x ctH$_2$O)/(% lipid) where ctHHb is the concentration of deoxy-hemoglobin in the tissue, ctH_2O is the concentration of water in the tissue and % lipid is the percent of lipids in the tissue.

Two studies demonstrated the ability of broadband DOS to differentiate between malignant breast tumors (stage II/III) and normal breast tissue in 12 pre-menopausal women (12) and 57 pre- and post-menopausal women (14). In both investigations, the concentration of deoxy-hemoglobin, oxy-hemoglobin, water and lipids as well as scattering power demonstrated significant contrast from tissue in the contralateral normal breast. The average Hb, HbO_2, and H_2O concentrations were significantly increased in the tumor region relative to the normal tissue, indicative of increased angiogenesis, edema and cellularity. The scattering power was also increased in the tumor regions, which presumably results from the greater epithelial and collagen content. Conversely, the percent lipid was decreased in the tumor regions, suggesting displacement of adipose tissue by the tumor mass. Interestingly, tissue hemoglobin saturation was statistically similar for both tumor and normal tissues; this finding is in agreement with the Softscan results presented by Intes (15). Finally, by combining several of these parameters into the TOI, the tumor to normal contrast was enhanced to almost 10-fold in the pre-menopausal population and approximately 3-fold in the larger patient population. This TOI is then used to monitor one patient’s response to adjuvant chemotherapy over an eight day treatment regime and demonstrated a 60% decrease in TOI. The authors do point out, however, that this composite contrast is highly variable in both studies.

Indocyanine Green (ICG)

The use of an intravenously injected exogenous contrast agent for breast cancer detection was demonstrated by Ntziachristos *et al* (41). The three case studies evaluated the ability of ICG-enhanced DOT to image malignant breast lesions. Overall, the ICG contrast enhancement appeared to accurately localize the infiltrating ductal carcinoma and fibroadenoma as determined by Gadolinium-enhanced MRI coregistration; the healthy breast tissue exhibited only minor contrast enhancements, which presumably resulted from small vasculature. The authors also attempted to quantify μ_a, but were unable to validate its accuracy.

EGF-Cy5.5

The NIR fluorophore-labeled epidermal growth factor (EGF-Cy5.5) represents another example of an exogenous NIR contrast agent. EGF is a ligand for the EGF receptor (EGFr), which is overexpressed in many malignant tumors including breast cancer (34). The specificity of EGF-Cy5.5 to EGFr was evaluated in human mammary cancer cells that were EGFr+ (MDA-MB-468) or EGFr- (MDA-MB-435). *In vitro* fluorescence microscopy confirmed uptake of EGF-Cy5.5 by MDA-MB-468 cells, but not MDA-MB-435 cells, while neither cell line appeared to be labeled by the free Cy5.5 dye. In addition, EGF-Cy5.5 labeling was inhibited by an anti-EGFr antibody and excess EGF ligand, suggesting EGFr specificity. The *in vivo* results corroborated the *in vitro* findings in mice bearing MDA-MB-468 and MDA-MB-435 xenografts. Furthermore, the uptake kinetics of EFG-Cy5.5 appeared to differentiate the EGFr+ and EGFr- tumors.

The Peripheral Benzodiazepine Receptor (PBR) and NIR-conPK11195 (Specific Aim I)

The peripheral benzodiazepine receptor (PBR) represents an attractive target for MI of disease. The PBR is a transmitochondrial membrane protein that is involved in a number of cellular process including steroidogenesis, cholesterol transport, cellular proliferation and apoptosis (42). Although PBR is naturally expressed at various levels in many normal tissues, PBR has been shown to be highly upregulated in a variety of neurodegenerative diseases and cancers including breast cancer (42-44). Clinically, the expression of PBR appears to correlate with disease stage, aggressive phenotype, and clinical prognosis (45, 46). Capitalizing on this expression profile and the low absorption and increased photon penetration depth in the NIR tissue transparency window (29), our laboratory has developed a PBR-targeted NIR MI agent (NIR-conPK11195). The quantitative evaluation of the *in vitro* and *in vivo* uptake of NIR-conPK11195 in a human metastatic breast adenocarcinoma (MDA-MB-231) model of breast cancer was accomplished through Specific Aim I, which is reported in Chapter III.

Brain Tumors: Significance

Both primary brain tumors and secondary brain metastases are often treated by maximum surgical resection followed by chemotherapy and/or radiation [reviewed in (47-50)]. Surgical resection provides cytoreduction of tumor mass as well as immediate symptomatic benefits including the reduction of intracranial hypertension, seizures and neurological deficits from the mass effect of the tumor (50, 51). Importantly, the extent of surgical resection has been shown to correlate with clinical prognosis, recurrence and overall patient survival (47-50). However, the degree of surgical resection is often compromised due to difficulties in accurately determining tumor location and ill-defined tumor boundaries. Thus, a number of imaging modalities have been employed to aid in intraoperative tumor localization in an attempt to perform more aggressive resections while preserving normal brain tissue.

Typical Intraoperative Methods for Brain Tumor Demarcation

Since neurosurgeons are often unable to solely rely upon the visual appearance or gross anatomy of the suspected lesion to achieve complete resection, surgical navigation systems are commonly used to aid in tumor localization. These surgical navigation systems use fiducial marking schemes and sophisticated algorithms to register an intraoperative probe to preoperative computed tomography (CT) or magnetic resonance (MR) images in three dimensions [reviewed in (52)]. However, the effectiveness of this technique is limited by the sensitivity of the preoperative imaging modality (CT or MRI) as well as spatial inaccuracies due to registration errors and intraoperative brain deformation (52).

The use of intraoperative ultrasound (iUS) takes advantage of the hyperechoic nature of tumor tissues to provide real-time feedback regarding tumor boundaries and extent of resection (53). However, additional echogenic signals resulting from the contused brain and irrigation fluid as well as astrocytosis from previously irradiated brain and peritumoral edema decrease the accuracy of iUS, particularly as surgery progresses (53, 54). The difficulties in iUS interpretation also limit its widespread clinical incorporation.

Intraoperative computed tomography (iCT) and intraoperative magnetic resonance imaging (iMRI) also provide real-time (or near real-time) information regarding tumor location and tissue characterization. In addition, these imaging modalities aid in the identification of surrounding anatomical markers (52, 55). However, iMRI systems are expensive, not particularly compatible with standard operating room (OR) equipment, and limit patient access, while iCT systems expose the patient and OR personnel to ionizing radiation.

Optical Intraoperative Methods for Brain Tumor Demarcation

In an effort to overcome some of the limitations of the commonly used image-guided surgery methods described above, a number of optical methods have also been explored for intraoperative brain tumor demarcation. These optical techniques include both intrinsic contrast mechanisms and intravenously administered fluorescent contrast agents.

Optical Spectrocopy

Intraoperative optical spectroscopy detects the intrinsic spectral differences between diseased and normal tissue using a combination of 337-nm excitation fluorescence and diffuse white light reflectance spectroscopy (18-20). These spectral characteristics, mainly peak location and line shape, have been correlated with histopathology from punch-biopsies taken from the interrogated tissue. Tissue-specific spectral comparisons were subsequently used to develop empirical discrimination algorithms for tissue segmentation (18-20). In a 24-patient study, Toms *et al* demonstrated 80% sensitivity and 89% specificity in discriminating solid gliomas from normal brain as well as 94% sensitivity and 93% specificity in delineating infiltrating tumor margins from normal brain using this technique (20).

Overall, optical spectroscopy represents a low cost, portable and easily integrated intraoperative imaging modality, especially relative to iCT or iMRI. Although the reported accuracy measurements are slightly low for clinical incorporation, ongoing improvements in data acquisition, data analysis, and algorithm development (based on larger sample populations) should increase the accuracy of this technique. Another clinical limitation of optical spectroscopy results from the use of a fiber-optic probe for light delivery and detection. The probe-based system requires tissue contact, interrogates only a small (600 x 670 µm) tissue area and does not provide spatial information. However, translation of probe-based optical spectroscopy to spectral imaging, which provides spectroscopic characterization at each pixel, has recently been explored (56).

Fluorescein-Based Agents

The use of an exogenous fluorescent contrast agent to discriminate between malignant and normal tissues dates back to at least 1947 when Moore reported the use of intravenously injected sodium fluorescein (57). In this study, the histological diagnosis of malignancy appeared to correlate with the vivid fluorescence of tumor tissues examined three to eight hours postinjection of sodium fluorescein (57). Out of twelve brain and spinal cord tumors examined, eleven cases demonstrated good correlation, one demonstrated poor correlation, and no failures were reported (57).

Sodium fluorescein (FLS-Na) has since been conjugated to human serum albumin (FLS-HSA) in an effort to enhance tumor-specificity and duration of fluorescence-enhanced contrast in a mouse xenograft model of human glioma (58). Although the brightness ratio of tumor to peripheral tissue was increased from 1.6 (FLS-Na) to at least 2.5 by using the HSA-conjugated fluorescein, the preclinical and clinical relevance of this probe is limited. In this study, FLS-HSA was excited through a bandpass of 450 – 490 nm and its emission collected between 500 – 530 nm. The depth of photon penetration through tissue is on the order of mm in this wavelength region and the autofluorescence of tissue is particularly high. Thus, to obtain adequate fluorescence signal, the authors sacrificed three mice at each time point and exposed the subcutaneous tumor nodules prior to imaging. In addition, the FLS-HSA contrast enhancement was not appreciable after approximately six hours post-injection, further limiting the intraoperative application of this molecule.

5-Aminolevulinic Acid (ALA)-Induced Porphyrin Fluorescence

Another fluorescence-guided surgical technique takes advantage of the malignant tumor-specific synthesis and intracellular accumulation of fluorescent porphyrins following administration of 5-aminolevulinic acid (ALA) (59, 60). In a preliminary investigation (60), bright reddish fluorescence was clearly visualized in the viable tumor tissues, which enabled detection of fluorescently labeled residual tumor and resulted in more complete tumor resection in seven of the nine patients studied; no residual tumor was apparent via intraoperative fluorescence or postoperative MR images. The location of the residual tumor in the other two patients precluded the ability to obtain complete surgical resection in order to preserve language function. However, the fluorescence-guided surgical protocol was not able to distinguish low-grade glioma from normal brain tissue, presumably due to the lack of blood-brain-barrier (BBB) breakdown in low grade lesions. In addition, grossly necrotic tumor tissue did not demonstrate fluorescence accumulation as one might expect; this is less important for fluorescence-guided surgical resection as necrotic tissue is relatively easy to distinguish from normal brain. The overall accuracy of porphyrin-enhanced tumor demarcation was determined by histological analysis of 89 biopsies, which resulted in 85% sensitivity, 100% specificity, and 90% accuracy (60). The sensitivity suffered from false-negative necrotic tissues and sparse densities of tumor cells in some samples.

To further assess the surgical resection improvement and long-term advantages associated with ALA-guided resections, Stummer and colleagues have since performed a one-site prospective study on 52 glioblastoma multiforme patients (61) and a multicenter phase III trial on 270 patients (5). Overall, the patient population that underwent ALA-guided surgery demonstrated an almost two-fold increase in percentage of complete resections as assessed by early postoperative MR scans than patients assigned to conventional white light microsurgery. The remaining residual tumors in the fluorescence-guided population were also smaller in volume. Furthermore, the fluorescence guided surgical resections resulted in an almost 2-fold increase in the 6-month progression free survival.

The use of ALA-induced porphyrin fluorescence to guide intraoperative surgical resection of malignant tumors shows promise and continues to be under active investigation. The increased intratumoral synthesis of the photosensitizing porphyrin enables tumor-specific labeling (60) rather than nonspecific uptake and decreased clearance of ICG due to the enhanced permeability and retention effect present in tumors (62) or the phagocytosis-dependent uptake of CLIO-Cy5.5 (63, 64) or quantum dots (65) by activated macrophages and microglia (discussed below). However, the use of ALA-induced porphyrin fluorescence may be restricted to high grade tumors with a disrupted BBB. In addition, the spectroscopic properties of porphyrins (strong absorption between 380 – 420 nm with emission peaks at 635 nm and 704 nm) severely limit the photon penetration depth (66).

Indocyanine Green (ICG)

In an effort to capitalize on the tissue transparency window (29), Haglund *et al* evaluated the ability of intravenously injected indocyanine green (ICG) to localize tumors and their margins in a rat glioma model (67). In this study, the peak optical change at six seconds post-injection was greater in the tumor regions (40.5 ± 9.6%) than in the surrounding tissue (16.4 ± 6.8%) and contralateral normal brain (9.7 ± 4.7%). In addition, the rate of fluorescence change over the first four seconds and the final signal plateau differentiate the three brain regions. These tumor-specific dynamic characteristics of ICG uptake and clearance presumably result from slower blood flow in tumor tissues, increased permeability and resulting extravasation from tumor capillaries as well as an increased rate of and overall uptake by the tumor tissues (67). To assess the accuracy of using ICG to delineate glial tissue from normal brain, the authors attempted surgical resection in the absence of fluorescence-guided cues, performed ICG-enhanced optical imaging and blindly biopsied tissues from the resulting tumor and normal brain regions. The histological samples revealed a sensitivity of 89.5% and specificity of 93%. Finally, the authors demonstrated the ability to discriminate tumor from normal tissue through the cranium and reported a significantly increased peak optical change in the tumor tissues relative to the signal emanating from the normal brain.

In a follow-up study, Haglund *et al* reported enhanced optical imaging of human gliomas using ICG in a preliminary study involving nine patients (68). The dynamic nature of ICG uptake and clearance again appeared to differentiate between normal brain, low-grade astrocytomas and malignant astrocytomas. In one patient, the ICG-enhanced imaging was performed after a preliminary gross-total resection attempt. After imaging, blinded biopsies were performed on tumor and normal tissues in the resection cavity, which appeared to accurately correlate with histology.

These combined results show promise for the clinical use of ICG for tumor demarcation, but it remains unclear how effective the use of ICG will be to distinguish small tumor islets or single infiltrating cells from normal tissue. Although the NIR spectroscopy of ICG enables increased tissue penetration (29), the detection limits of this technique and the contrast threshold necessary to discriminate tumor tissues should be addressed. In addition, this imaging procedure suffers from a short temporal contrast enhancement of 2 – 10 minutes. This limited window of differentiation between tumor and normal tissues suggests that subsequent re-injection of ICG will be necessary following a surgical resection attempt, resulting in increased cost and surgical duration. The use of targeted NIR agents should allow for enhanced tumor-specificity, increased sensitivity, and prolonged fluorescence-based resection cues.

Cy5.5-CLIO

To enable both preoperative MRI and intraoperative NIR brain tumor delineation using a single probe, Kircher and colleagues developed Cy5.5-CLIO (63). This multimodal nanoparticle was synthesized by covalently attaching the NIR fluorochrome Cy5.5 to a superparamagnetic iron oxide core coated with crosslinked dextran (63, 64). Accumulation of Cy5.5-CLIO in the tumor tissue of GFP-expressing 9L glioma-bearing rats appeared as a hypointense region on a T2-weighted MR image. The MR contrast correlated well with both *ex vivo* hematoxylin and eosin (H&E) staining and DAB-amplified Prussian blue staining for iron. The intraoperative use of Cy5.5-CLIO was then demonstrated by visual and quantitative comparisons of the extent of tumor labeled with Cy5.5-CLIO relative to the true tumor size as determined by the “gold standard” GFP signal. The Cy5.5-CLIO slightly overestimates the extent of tumor volume, which is justified by the uptake of Cy5.5-CLIO by microglia and the extension of microglia beyond the tumor margin. The microglia-specific sequestration of Cy5.5-CLIO is demonstrated by laser scanning confocal microscopy following anti-CD11b staining for microglia and macrophages. Interestingly, the Cy5.5-CLIO accumulation did not show a strong correlation to the GFP-positive tumor cells, but rather only to the CD11b-positive microglia and macrophages.

An extension of this study assessed the effects of host response on the uptake of CLIO-Cy5.5, demonstrated a non-user-based quantitation algorithm to determine margin accuracy, determined cellular specificity of CLIO-Cy5.5 uptake via fluorescence-activated cell sorter (FACS) analysis, described the distribution of host cells within the context of the tumors, and examined additional primary and metastatic brain tumor models (64). CLIO-Cy5.5 accumulation was apparent in both tumor-bearing immunocompromised mice and immunocompetent rats. However, a larger population of microglia and macrophages was present in the immunocompetent rats, resulting in a slightly greater tumor margin overestimation (mean overestimation = 24 µm) relative to the immunocompromised mice (mean overestimation = 2 µm). Overall, the tumor margin estimations based on a predefined threshold were a maximum of 65 µm overestimated and 64 µm underestimated in the nude mice versus a maximum of 151 µm overestimated and 57 µm underestimated in the rat model. Contrary to previous observations (63), Trehin *et al* report CLIO-Cy5.5 uptake in tumor cells as well as $CD11b^+$ microglia and macrophages. Finally, the authors demonstrate labeling of intracranial CT26 colon and Gli36 glioma models.

The CLIO-Cy5.5 agent provides a number of advantages over previously described optical demarcation techniques. First, the multimodal nature of the single nanoparticles allows preoperative MRI contrast and intraoperative NIR signal from the same cells. CLIO-Cy5.5 also provides the same NIR advantages as ICG including minimal tissue autofluorescence as well as decreased absorption and scattering, resulting in photon penetration through several centimeters of tissue (29). Unlike ICG, CLIO-Cy5.5's long circulation and slow degradation/clearance provide a longer fluorescence-enhanced surgical window (12 - 48 hours) than the ICG study (10 minutes in most cases). However, the ability to image this agent *in vivo* remains to be seen. In addition, the authors suggest that the discrepancy in tumor cell uptake (64) or lack thereof (63) can be explained by the differing sensitivities of fluorescence microscopy and FACS analysis and contend that fluorescence microscopy may not be able to detect low CLIO-Cy5.5

concentrations in a high percentage of cells. However, the FACS analysis indicates that the tumor cells in both the nude mouse and rat glioma models had greater relative median fluorescence than the CD11b$^+$ cells. Furthermore, the intraoperative use of Cy5.5-CLIO would require a substantial concentration of agent in the tumor cells to provide clinical relevance if currently only detectable by FACS analysis. Finally, the increased photon penetration of Cy5.5-CLIO may actually decrease the meaningful spatial resolution for intraoperative tumor resection. A targeted approach with higher signal to noise should provide increased sensitivity and additional tumor-specificity.

Quantum Dots (Qdots)

Recently, the intravenous administration of an alternative nanocrystal, specifically a NIR-emitting Quantum dot (Qdot), enabled fluorescence-enhanced detection of implanted tumors and some satellite lesions in brain tumor-bearing rodents (65). Conversely, no Qdot-specific fluorescence was observed in the brain tissue surrounding the tumor or contralateral normal brain hemispheres of the tumor-bearing rodents as well as in the brain tissues of non-tumor-bearing animals. Consistent with other reports of nanoparticle uptake and internalization including the CLIO-Cy5.5 probe (63, 64), Qdots appeared to localize to tumor-infiltrating CD11b$^+$ macrophages and microglia (65).

Qdots provide some advantages over traditional fluorophores including size-tunable broad excitation spectra and narrow emission peaks, intrinsic brightness and superior photostability (65). NIR Qdots also have the advantage of increased tissue penetration of emission light due to the decreased absorption and scattering in the NIR tissue transparency window (29), as previously discussed for ICG and Cy5.5. However, unlike ICG and Cy5.5, NIR Qdots are much more efficiently excited in the UV wavelength region than by red-shifted wavelengths, dramatically decreasing the penetration depth of its excitation light (when excited with UV) or substantially reducing the absorbed photons and subsequent emission intensity (when excited with red-shifted light). In addition, the cadmium selenide cores have the potential for significant toxicity, particularly with an insufficient protective coating. Alternative nanoparticles with NIR emission capabilities have recently been developed (69). And finally, a targeted approach that would enable labeling of the tumor cells themselves in addition to the tumor-infiltrating macrophages and microglia would provide greater sensitivity and specificity of the tumor demarcation.

NIR-conPK11195 for Brain Tumor Demarcation (Specific Aim II)

Previous studies have demonstrated cellular uptake and PBR-specificity of Eu^{3+}-conPK11195 and NIR-conPK11195 in C6 rat glioma cells (70) and MDA-MB-231 human metastatic breast adenocarcinoma cells (Chapter III of this dissertation), respectively. In addition, NIR-conPK11195 has demonstrated preferential labeling of MDA-MB-231 cells *in vivo* with an 11-fold contrast enhancement over normal tissue and a 5- to 7-fold enhancement over free NIR dye (Chapter III). Through Specific Aim II, we report an extension of these results and evaluate the applicability of using Eu^{3+}-conPK11195 as a topical agent for brain tumor demarcation and NIR-conPK11195 as a molecular imaging agent to study breast cancer metastases to the brain (Chapter IV).

2-[^{18}F]Fluoro-2-Deoxy-D-Glucose (^{18}FDG) Positron Emission Tomography

The most commonly used radiopharmaceutical, 2-[^{18}F]fluoro-2-deoxy-D-glucose (^{18}FDG), is valuable in oncologic diagnostics and therapeutic efficacy monitoring based on its versatility and sensitive detection of increased metabolic activity by positron emission tomography (PET) (71, 72). The preferential uptake and accumulation of ^{18}FDG in cancerous tissues results from increased glycolysis by tumor cells. Upregulation of glucose transporter proteins (GLUTs) and the presence of a highly active hexokinase are responsible for the enhanced glucose metabolism of malignant tumor cells. The cellular uptake of ^{18}FDG occurs via these GLUTs. Once internalized, ^{18}FDG is phosphorylated by hexokinase to ^{18}FDG-6-phosphate in a similar manner as glucose. However, unlike glucose-6-phosphate, ^{18}FDG-6-phosphate cannot be further metabolized due to the lack of a hydroxyl group at the C-2 position, resulting in intracellular accumulation of ^{18}FDG-6-phosphate and tumor-specific PET signal (71, 72).

While ^{18}FDG-PET has inherently high sensitivity and demonstrated clinical applicability, the imaging technique has several limitations. These drawbacks include the exposure to ionizing radiation, difficulty of compound synthesis, requirement of a local cyclotron, short halflife of ^{18}F (110 minutes) and relatively low spatial resolution. In an attempt to overcome some of the major limitations of PET, our laboratory and others have developed potential optical analogues of ^{18}FDG including 2-[N-(7-nitrobenz-2-oxa-1,3-diazol-4-yl)amino]-2-deoxy-D-glucose (2-NBDG) (35, 73-77), pyropheophorbide 2-deoxyglucosamide (Pyro-2DG) (78, 79), fluorescent dendritic arrays of glucosamine (80), and Cy5.5-D-glucosamine (Cy5.5-2DG) (81).

Optical ^{18}FDG Analogues

2-[N-(7-nitrobenz-2-oxa-1,3-diazol-4-yl)amino]-2-deoxy-D-glucose (2-NBDG)

To evaluate glucose uptake activity and rapidly assess cell viability, Yoshioka *et al* synthesized 2-[N-(7-nitrobenz-2-oxa-1,3-diazol-4-yl)amino]-2-deoxy-D-glucose (2-NBDG) by conjugating 4-chloro-7-nitrobenz-2-oxa-1,3-diazole (NBD-Cl) to D-glucosamine (35). 2-NBDG effectively labeled live *Escherichia coli* B (*E. coli*) cells, but not dead cells, which was confirmed by propidium iodide staining. Since D-glucose, but not L-glucose, competitively inhibited 2-NBDG uptake, the mechanism of 2-NBDG accumulation was attributed to the glucose transporting system. In a follow-up study, mass spectrometry was employed to demonstrate that 2-NBDG can be phosphorylated to 2-NBDG-6-phosphate in *E. coli* cells (74). Combined, these results suggest that 2-NBDG functions as a fluorescent derivative of D-glucose and may be useful as a metabolic indicator.

2-NBDG has subsequently been used to evaluate glucose uptake and cellular viability in several cell lines including yeast cells (73, 76), GLUT2-overexpressing pancreatic β cells (75) and tumor cells (77). In each case, the uptake of 2-NBDG was competitively inhibited by D-glucose, but not L-glucose. Another known GLUT inhibitor, cytochalasin B, almost completely blocked 2-NBDG uptake in the GLUT2-overexpressing pancreatic β cells (75).

Although 2-NBDG appears to label metabolically active cells via GLUT-mediated uptake and likely accumulates through hexokinase phosphorylation, the spectroscopic properties (λ_{ex} = 475 nm and λ_{em} = 550 nm) render the 2-NBDG probe a poor choice for *in vivo* imaging. In addition, the uptake of 2-NBDG has not been compared to the uptake of free NBD. Comparison to the unconjugated fluorophore is particularly important at high agent concentrations, such as the ones used in these studies (10 – 600 µM), due to potential non-specific binding.

Pyropheophorbide 2-Deoxyglucosamide (Pyro-2DG)

In an attempt to exploit the intracellular trapping of 2-deoxyglucose and the relative tissue transparency in the NIR wavelength region, Zhang *et al* developed a pyropheophorbide derivative of (Pyro-2DG). Pyro-2DG, which functions as both a NIR imaging and photodynamic therapy agent, was evaluated in a 9L rat glioma model (78, 79) and a c-Myc-induced mammary tumor model (79). Fluorescence imaging demonstrated preferential uptake of Pyro-2DG in the tumor tissue relative to the surrounding muscle tissue with a 10:1 tumor to normal contrast ratio in both tumor models approximately two hours post-injection. Conversely, the uptake of the 2DG-lacking Pyro-acid resulted in only a 1.5:1 tumor to normal ratio (79). The photoactivation of Pyro-2DG resulted in point-specific mitochondrial damage that was not observed in the control animals lacking Pyro-2DG or the Pyro-2DG-injected animals that were not photoirradiated (79). In addition, the redox ratio (a measure of energy metabolism) was highly correlated to Pyro-2DG uptake, but not Pyro-acid (79). Finally, preliminary confocal microscopy studies suggest that Pyro-2DG uptake was competitively inhibited by D-glucose (78).

Fluorescent Dendritic Arrays of Glucosamine

Samuel Achilefu's group has synthesized dendritic arrays of glucosamine based on an inner NIR carbocyanine core including mono-, di-, tri-, tetra-, hexa-, and octa-D(+)-glucosamine-containing derivatives of cypate (80). Although the number of glucosamines conjugated to the multicarboxylate probe does not appear to correlate with tumor uptake, each of the dendritic glucosamine arrays provided some tumor signal. The maximum tumor uptake at twenty-four hours post-injection resulted from the di- and tri-glucosamine probes. However, the diglucosamine derivative also demonstrated substantial retention in the kidneys as well as the skin. The high fluorescence signal in the skin is particularly disadvantageous since increased background fluorescence will decrease tumor to normal tissue contrast, crucial for noninvasive optical imaging. The monoglucosamine and tetraglucosamine agents primarily accumulated in the liver, with considerably less uptake in the tumors. Finally, the octaglucosamine probe accumulated in the tumor within six hours post-injection but was mainly retained in the kidneys 24 hours post-injection. The octaglucosamine also suffered from skin retention and therefore low tumor to normal contrast.

The lack of correlation between the number of tethered glucosamines and tumor uptake of glucosamine-containing derivatives of cypate reveals the crucial need for optimization of probes for particular biomedical applications (80). For example, the triglucosamine-containing derivative of cypate demonstrated the highest tumor accumulation in combination with decreased normal tissue uptake, suggesting a role for tumor-specific labeling. And, although the tetraglucosamine probe primarily accumulated in the liver, the agent retention in the blood for over 24 hours could prove useful for imaging vasculature or monitoring blood flow (80). However, the mechanisms of uptake and accumulation of the glucosamine-containing cypate derivatives remain unknown. Thus, these multivalent molecular beacons may actually not represent glucose analogues.

Cy5.5-D-glucosamine (Cy5.5-2DG)

After demonstrating the D-glucose (but not L-glucose) inhibited uptake of 2-NBDG in U87MG human glioblastoma cells, Chen *et al* developed and evaluated Cy5.5-2DG for use as an optical glucose analogue (81). First, fluorescence microscopy demonstrated that Cy5.5-2DG labeled a variety of tumor cell lines at 37°C, but was only marginally taken up at 4°C, suggesting an active uptake mechanism. However, the free NIR dye (Cy5.5-NHS) was equally effective at labeling the tumor cells in a temperature-dependent manner and the Cy5.5-2DG uptake was not inhibited by D-glucose, indicating that GLUTs are likely not involved. Next, the authors were unable to demonstrate that Cy5.5-2DG can be phosphorylated to Cy5.5-2DG-6-phosphate by MALDI-TOF-MS analysis, suggesting that Cy5.5-2DG may not be metabolized by hexokinase. Finally, the *in vivo* results demonstrated tumor-specific accumulation of both Cy5.5-2DG and Cy5.5-NHS. In terms of tumor to normal contrast, the Cy5.5-NHS actually performed better than Cy5.5-2DG, but ^{18}FDG provided better tumor contrast than either Cy5.5-2DG or Cy5.5-NHS. These observations were corroborated in an A375M melanoma tumor model.

Overall, Cy5.5-2DG and Cy5.5-NHS appear to label tumors *in vivo* with fairly high specificity and long retention times, but Cy5.5-DG does not appear to act as an optical analogue to ^{18}FDG. The authors attribute the difference in 2-NBDG and Cy5.5-2DG GLUT/hexokinase-specificity to the size of the fluorophore conjugated to the glucosamine.

NIR-glucosamine as a Potential Optical Analogue to ^{18}FDG (Specific Aim III)

Based on the literature precedence regarding optical analogues to ^{18}FDG, our laboratory has developed an alternative NIR deoxyglucose analogue by conjugating D-glucosamine to LI-COR Biosciences' IRDye$^{\text{TM}}$ 800CW. The IRDye$^{\text{TM}}$ 800CW is a cyanine-like dye that is highly water soluble and relatively stable. IRDye$^{\text{TM}}$ 800CW capitalizes on the increased photon penetration in the NIR tissue transparency window and is slightly red-shifted relative to Cy5.5. This red-shift in excitation and emission eliminates the fluorescence contribution from the autofluorescence of typical alfalfa-based rodent chow, which is often seen in the Cy5.5 wavelength region, and is more suitable for *in vivo* imaging (34). In chapter V, we report the *in vitro* and *in vivo* characterization of NIR-glucosamine in an SW480*neo* mouse model of human colon cancer that corroborates and expands upon the Cy5.5-2DG observations (81).

References

1. Society, A. C. Cancer Facts and Figures 2007. Atlanta: American Cancer Society, 2007.

2. Herschman, H. R. Molecular imaging: Looking at problems, seeing solutions. Science, *302:* 605-608, 2003.

3. Evelhoch, J. L., Gillies, R. J., Karczmar, G. S., Koutcher, J. A., Maxwell, R. J., Nalcioglu, O., Raghunand, N., Ronen, S. M., Ross, B. D., and Swartz, H. M. Applications of magnetic resonance in model systems: Cancer therapeutics. Neoplasia, *2:* 152-165, 2000.

4. Hengerer, A., Wunder, A., Wagenaar, D. J., Vija, A. H., Shah, M., and Grimm, J. From genomics to clinical molecular imaging. Proceedings of the Ieee, *93:* 819-828, 2005.

5. Stummer, W., Pichlmeier, U., Meinel, T., Wiestler, O. D., Zanella, F., Hans-Jurgen, R., and Grp, A.-G. S. Fluorescence-guided surgery with 5-aminolevulinic acid for resection of malignant glioma: a randomised controlled multicentre phase III trial. Lancet Oncology, *7:* 392-401, 2006.

6. Massoud, T. F. and Gambhir, S. S. Molecular imaging in living subjects: seeing fundamental biological processes in a new light. Genes & Development, *17:* 545-580, 2003.

7. Dzik-Jurasz, A. S. K. Molecular imaging in vivo: an introduction. British Journal of Radiology, *76:* S98-S109, 2003.

8. Cassidy, P. J. and Radda, G. K. Molecular imaging perspectives. Journal of the Royal Society Interface, *2005:* 1-12, 2005.

9. Benaron, D. A. The future of cancer imaging. Cancer and Metastasis Reviews, *21:* 45-78, 2002.

10. Nasongkla, N., Bey, E., Ren, J. M., Ai, H., Khemtong, C., Guthi, J. S., Chin, S. F., Sherry, A. D., Boothman, D. A., and Gao, J. M. Multifunctional polymeric micelles as cancer-targeted, MRI-ultrasensitive drug delivery systems. Nano Letters, *6:* 2427-2430, 2006.

11. Weissleder, R. Scaling down imaging: Molecular mapping of cancer in mice. Nature Reviews Cancer, *2:* 11-18, 2002.

12. Tromberg, B. J., Cerussi, A., Shah, N., Compton, M., Durkin, A., Hsiang, D., Butler, J., and Mehta, R. Imaging in breast cancer - Diffuse optics in breast cancer: detecting tumors in pre-menopausal women and monitoring neoadjuvant chemotherapy. Breast Cancer Research, *7:* 279-285, 2005.

13. Ntziachristos, V. and Chance, B. Probing physiology and molecular function using optical imaging: applications to breast cancer. Breast Cancer Research, *3:* 41-46, 2001.

14. Cerussi, A., Shah, N., Hsiang, D., Durkin, A., Butler, J., and Tromberg, B. J. In vivo absorption, scattering, and physiologic properties of 58 malignant breast tumors determined by broadband diffuse optical spectroscopy. Journal of Biomedical Optics, *11:* 044005, 2006.

15. Intes, X., Djeziri, S., Ichalalene, Z., Mincu, N., Wang, Y., St-Jean, P., Lesage, F., Hall, D., Boas, D., Polyzos, M., Fleiszer, D., and Mesurolle, B. Time-domain optical mammography SoftScan: Initial results (vol 12, pg 934, 2005). Academic Radiology, *12:* 1355-1355, 2005.

16. Zhu, Q., Cronin, E. B., Currier, A. A., Vine, H. S., Huang, M. M., Chen, N. G., and Xu, C. Benign versus malignant breast masses: Optical differentiation with US-guided optical imaging reconstruction. Radiology, *237:* 57-66, 2005.

17. Mahadevan-Jansen, A., Mitchell, W. F., Ramanujam, N., Utzinger, U., and Richards-Kortum, R. Development of a fiber optic probe to measure NIR Raman spectra of cervical tissue in vivo. Photochemistry and Photobiology, *68:* 427-431, 1998.

18. Lin, W. C., Toms, S. A., Motamedi, M., Jansen, E. D., and Mahadevan-Jansen, A. Brain tumor demarcation using optical spectroscopy; an in vitro study. Journal of Biomedical Optics, *5:* 214-220, 2000.

19. Lin, W. C., Toms, S. A., Johnson, M., Jansen, E. D., and Mahadevan-Jansen, A. In vivo brain tumor demarcation using optical spectroscopy. Photochemistry and Photobiology, *73:* 396-402, 2001.

20. Toms, S. A., Lin, W. C., Weil, R. J., Johnson, M. D., Jansen, E. D., and Mahadevan-Jansen, A. Intraoperative optical spectroscopy identifies infiltrating glioma margins with high sensitivity. Neurosurgery, *57(4 Suppl):* 382-391, 2005.

21. Zhao, H., Doyle, T. C., Coquoz, O., Kalish, F., Rice, B. W., and Contag, C. H. Emission spectra of bioluminscent reporters and interaction with mammalian tissue determine the sensitivity of detection in vivo. Journal of Biomedical Optics, *10:* 041210, 2005.

22. Contag, C. H. and Ross, B. D. It's not just about anatomy: In vivo bioluminescence imaging as an eyepiece into biology. Journal of Magnetic Resonance Imaging, *16:* 378-387, 2002.

23. Thorne, S. H. and Contag, C. H. Using in vivo bioluminescence imaging to shed light on cancer biology. Proceedings of the Ieee, *93:* 750-762, 2005.

24. Promega Promega Protocols and Applications Guide. Chapter 8: Bioluminescence Reporters. Vol. 2005.

25. Virostko, J. M., Powers, A. C., and Jansen, E. D. Bioluminescent imaging of transplanted pancreatic islets. Lasers in Surgery and Medicine 10-10, 2004.

26. Bremer, C., Ntziachristos, V., and Weissleder, R. Optical-based molecular imaging: contrast agents and potential medical applications. European Radiology, *13:* 231-243, 2003.

27. Ntziachristos, V. Fluorescence molecular imaging. Annual Review of Biomedical Engineering, *8:* 1-33, 2006.

28. Weissleder, R. and Ntziachristos, V. Shedding light onto live molecular targets. Nature Medicine, *9:* 123-128, 2003.

29. Weissleder, R. A clearer vision for in vivo imaging. Nature Biotechnology, *19:* 316-317, 2001.

30. Mansfield, J. R., Gossage, K. W., Hoyt, C. C., and Levenson, R. M. Autofluorescence removal, multiplexing, and automated analysis methods for in-vivo fluorescence imaging. Journal of Biomedical Optics, *10:* 041207, 2005.

31. Ntziachristos, V., Ripoll, J., and Weissleder, R. Would near-infrared fluorescence signals propagate through large human organs for clinical studies? Optics Letters, *27:* 333-335, 2002.

32. McIntyre, J. O., Fingleton, B., Wells, K. S., Piston, D. W., Lynch, C. C., Gautam, S., and Matrisian, L. M. Development of a novel fluorogenic proteolytic beacon for in vivo detection and imaging of tumour-associated matrix metalloproteinase-7 activity. Biochemical Journal, *377:* 617-628, 2004.

33. Manning, H. C., Smith, S. M., Sexton, M., Haviland, S., Bai, M., Cederquist, K., Stella, N., and Bornhop, D. J. A peripheral benzodiazepine receptor targeted agent for in vitro imaging and screening. Bioconjugate Chemistry, *17:* 735-740, 2006.

34. Ke, S., Wen, X. X., Gurfinkel, M., Charnsangavej, C., Wallace, S., Sevick-Muraca, E. M., and Li, C. Near-infrared optical imaging of epidermal growth factor receptor in breast cancer xenografts. Cancer Research, *63:* 7870-7875, 2003.

35. Yoshioka, K., Takahashi, H., Homma, T., Saito, M., Oh, K. B., Nemoto, Y., and Matsuoka, H. A novel fluorescent derivative of glucose applicable to the assessment of glucose uptake activity of Escherichia coli. Biochimica Et Biophysica Acta-General Subjects, *1289:* 5-9, 1996.

36. Weissleder, R. and Mahmood, U. Molecular imaging. Radiology, *219:* 316-333, 2001.

37. National Breast Cancer Foundation, I., Vol. 2007, 2007.

38. Elmore, J. G., Armstrong, K., Lehman, C. D., and Fletcher, S. W. Screening for breast cancer. Jama-Journal of the American Medical Association, *293:* 1245-1256, 2005.

39. Carney, P. A., Miglioretti, D. L., Yankaskas, B. C., Kerlikowske, K., Rosenberg, R., Rutter, C. M., Geller, B. M., Abraham, L. A., Taplin, S. H., Dignan, M., Cutter, G., and Ballard-Barbash, R. Individual and combined effects of age, breast density, and hormone replacement therapy use on the accuracy of screening mammography. Annals of Internal Medicine, *138:* 168-175, 2003.

40. Stavros, A. T., Thickman, D., Rapp, C. L., Dennis, M. A., Parker, S. H., and Sisney, G. A. Solid Breast Nodules - Use of Sonography to Distinguish Benign and Malignant Lesions. Radiology, *196:* 123-134, 1995.

41. Ntziachristos, V., Yodh, A. G., Schnall, M., and Chance, B. Concurrent MRI and diffuse optical tomography of breast after indocyanine green enhancement. Proceedings of the National Academy of Sciences of the United States of America, *97:* 2767-2772, 2000.

42. Papadopoulos, V., Baraldi, M., Guilarte, T. R., Knudsen, T. B., Lacapere, J. J., Lindemann, P., Norenberg, M. D., Nutt, D., Weizman, A., Zhang, M. R., and Gavish, M. Translocator protein (18 kDa): new nomenclature for the peripheral-type benzodiazepine receptor based on its structure and molecular function. Trends in Pharmacological Sciences, *27:* 402-409, 2006.

43. Han, Z. Q., Slack, R. S., Li, W. P., and Papadopoulos, V. Expression of peripheral benzodiazepine receptor (PBR) in human tumors: Relationship to breast, colorectal, and prostate tumor progression. Journal of Receptors and Signal Transduction, *23:* 225-238, 2003.

44. Venneti, S., Lopresti, B. J., and Wiley, C. A. The peripheral benzodiazepine receptor (Translocator protein 18 kDa) in microglia: From pathology to imaging. Progress in Neurobiology, 2006.

45. Hardwick, M., Fertikh, D., Culty, M., Li, H., Vidic, B., and Papadopoulos, V. Peripheral-type benzodiazepine receptor (PBR) in human breast cancer: Correlation of breast cancer cell aggressive phenotype with PBR expression, nuclear localization, and PBR-mediated cell proliferation and nuclear transport of cholesterol. Cancer Research, *59:* 831-842, 1999.

46. Maaser, K., Grabowski, P., Sutter, A. P., Hopfner, M., Foss, H. D., Stein, H., Berger, G., Gavish, M., Zeitz, M., and Scherubl, H. Overexpression of the peripheral benzodiazepine receptor is a relevant prognostic factor in stage III colorectal cancer. Clinical Cancer Research, *8:* 3205-3209, 2002.

47. Lefranc, F., Sadeghi, N., Camby, I., Metens, T., Dewitte, O., and Kiss, R. Present and potential future issues in glioblastoma treatment. Expert Review of Anticancer Therapy, *6:* 719-732, 2006.

48. Weil, R. J., Palmieri, D. C., Bronder, J. L., Stark, A. M., and Steeg, P. S. Breast cancer metastasis to the central nervous system. American Journal of Pathology, *167:* 913-920, 2005.

49. Nathoo, N., Toms, S. A., and Barnett, G. H. Metastases to the brain: current management perspectives. Expert Rev. Neurotherapeutics, *4:* 633-640, 2004.

50. Soffietti, R., Ruda, R., and Mutani, R. Management of brain metastases. Journal of Neurology, *249:* 1357-1369, 2002.

51. Toms, S. A., Ferson, D. Z., and Sawaya, R. Basic surgical techniques in the resection of malignant gliomas. Journal of Neuro-Oncology, *42:* 215-226, 1999.

52. Peters, T. M. Image-guidance for surgical procedures. Physics in Medicine and Biology, *51:* R505-R540, 2006.

53. Sosna, J., Barth, M. M., Kruskal, J. B., and Kane, R. A. Intraoperative sonography for neurosurgery. Journal of Ultrasound in Medicine, *24:* 1671-1682, 2005.

54. Leroux, P. D., Berger, M. S., Ojemann, G. A., Wang, K., and Mack, L. A. Correlation of Intraoperative Ultrasound Tumor Volumes and Margins with Preoperative Computerized-Tomography Scans - an Intraoperative Method to Enhance Tumor Resection. Journal of Neurosurgery, *71:* 691-698, 1989.

55. Black, P. M., Moriarty, T., Alexander, E., Stieg, P., Woodard, E. J., Gleason, P. L., Martin, C. H., Kikinis, R., Schwartz, R. B., and Jolesz, F. A. Development and implementation of intraoperative magnetic resonance imaging and its neurosurgical applications. Neurosurgery, *41:* 831-842, 1997.

56. Gebhart, S. C., Majumder, S. K., and Mahadevan-Jansen, A. Comparison of spectral variation from spectroscopy to spectral imaging. Applied Optics, *46:* 1343-1360, 2007.

57. Moore, G. E. Fluorescein as an agent in the differentiation of normal and malignant tissues. Science, *106:* 130-131, 1947.

58. Ichioka, T., Miyatake, S. I., Asai, N., Kajimoto, Y., Nakagawa, T., Hayashi, H., and Kuroiwa, T. Enhanced detection of malignant glioma xenograft by fluorescein-human serum albumin conjugate. Journal of Neuro-Oncology, *67:* 47-52, 2004.

59. Kennedy, J. C. and Pottier, R. H. Endogenous Protoporphyrin-Ix, a Clinically Useful Photosensitizer for Photodynamic Therapy. Journal of Photochemistry and Photobiology B-Biology, *14:* 275-292, 1992.

60. Stummer, W., Stocker, S., Wagner, S., Stepp, H., Fritsch, C., Goetz, C., Goetz, A. E., Kiefmann, R., and Reulen, H. J. Intraoperative detection of malignant gliomas by 5-aminolevulinic acid-induced porphyrin fluorescence. Neurosurgery, *42:* 518-525, 1998.

61. Stummer, W., Novotny, A., Stepp, H., Goetz, C., Bise, K., and Reulen, H. J. Fluorescence-guided resection of glioblastoma multiforme by using 5-aminolevulinic acid-induced porphyrins: a prospective study in 52 consecutive patients. Journal of Neurosurgery, *93:* 1003-1013, 2000.

62. Iyer, A. K., Khaled, G., Fang, J., and Maeda, H. Exploiting the enhanced permeability and retention effect for tumor targeting. Drug Discovery Today, *11:* 812-818, 2006.

63. Kircher, M. F., Mahmood, U., King, R. S., Weissleder, R., and Josephson, L. A multimodal nanoparticle for preoperative magnetic resonance imaging and intraoperative optical brain tumor delineation. Cancer Research, *63:* 8122-8125, 2003.

64. Trehin, R., Figueiredo, J. L., Pittet, M. J., Weissleder, R., Josephson, L., and Mahmood, U. Fluorescent nanoparticle uptake for brain tumor visualization. Neoplasia, *8:* 302-311, 2006.

65. Popescu, M. A. and Toms, S. A. In vivo optical imaging using quantum dots for the management of brain tumors. Expert Review of Molecular Diagnostics, *6:* 879-890, 2006.

66. Stummer, W., Stepp, H., Moller, G., Ehrhardt, A., Leonhard, M., and Reulen, H. J. Technical principles for protoporphyrin-IX-fluorescence guided microsurgical resection of malignant glioma tissue. Acta Neurochirurgica, *140:* 995-+, 1998.

67. Haglund, M. M., Hochman, D. W., Spence, A. M., and Berger, M. S. Enhanced optical imaging of rat gliomas and tumor margins. Neurosurgery, *35:* 930-941, 1994.

68. Haglund, M. M., Berger, M. S., and Hochman, D. W. Enhanced optical imaging of human gliomas and tumor margins. Neurosurgery, *38:* 308-317, 1996.

69. Ren, L., Zhang, Q. Q., and Chow, G. M. Synthesis, characterization and preliminary toxicity assays of NIR-active Au-silicate nanoparticles through a sol-gel processing. Journal of Sol-Gel Science and Technology, *39:* 269-274, 2006.

70. Manning, H. C., Goebel, T., Thompson, R. C., Price, R. R., Lee, H., and Bornhop, D. J. Targeted molecular imaging agents for cellular-scale bimodal imaging. Bioconjugate Chemistry, *15:* 1488-1495, 2004.

71. Pauwels, E. K. J., Ribeiro, M. J., Stoot, J. H. M. B., McCready, V. R., Bourguignon, M., and Maziere, B. FDG accumulation and tumor biology. Nuclear Medicine and Biology, *25:* 317-322, 1998.

72. Gambhir, S. S. Molecular imaging of cancer with positron emission tomography. Nature Reviews Cancer, *2:* 683-693, 2002.

73. Yoshioka, K., Oh, K. B., Saito, M., Nemoto, Y., and Matsuoka, H. Evaluation of 2-[N-(7-nitrobenz-2-oxa-1,3-diazol-4-yl)amino]-2-deoxy-D-glucose, a new fluorescent derivative of glucose, for viability assessment of yeast Candida albicans. Applied Microbiology and Biotechnology, *46:* 400-404, 1996.

74. Yoshioka, K., Saito, M., Oh, K. B., Nemoto, Y., Matsuoka, H., Natsume, M., and Abe, H. Intracellular fate of 2-NBDG, a fluorescent probe for glucose uptake activity, in Escherichia coli cells. Bioscience Biotechnology and Biochemistry, *60:* 1899-1901, 1996.

75. Yamada, K., Nakata, M., Horimoto, N., Saito, M., Matsuoka, H., and Inagaki, N. Measurement of glucose uptake and intracellular calcium concentration in single, living pancreatic beta-cells. Journal of Biological Chemistry, *275:* 22278-22283, 2000.

76. Oh, K. B. and Matsuoka, H. Rapid viability assessment of yeast cells using vital staining with 2-NBDG, a fluorescent derivative of glucose. International Journal of Food Microbiology, *76:* 47-53, 2002.

77. O'Neil, R. G., Wu, L., and Mullani, N. Uptake of a fluorescent deoxyglucose analog (2-NBDG) in tumor cells. Molecular Imaging and Biology, *7:* 388-392, 2005.

78. Zhang, M., Zhang, Z. H., Blessington, D., Li, H., Busch, T. M., Madrak, V., Miles, J., Chance, B., Glickson, J. D., and Zheng, G. Pyropheophorbide 2-deoxyglucosamide: A new photosensitizer targeting glucose transporters. Bioconjugate Chemistry, *14:* 709-714, 2003.

79. Zhang, Z. H., Li, H., Liu, Q., Zhou, L. L., Zhang, M., Luo, Q. M., Glickson, J., Chance, B., and Zheng, G. Metabolic imaging of tumors using intrinsic and extrinsic fluorescent markers. Biosensors & Bioelectronics, *20:* 643-650, 2004.

80. Ye, Y. P., Bloch, S., Kao, J., and Achilefu, S. Multivalent carbocyanine molecular probes: Synthesis and applications. Bioconjugate Chemistry, *16:* 51-61, 2005.

81. Cheng, Z., Levi, J., Xiong, Z. M., Gheysens, O., Keren, S., Chen, X. Y., and Gambhir, S. S. Near-infrared fluorescent deoxyglucose analogue for tumor optical imaging in cell culture and living mice. Bioconjugate Chemistry, *17:* 662-669, 2006.

CHAPTER III

OPTICAL MOLECULAR IMAGING USING A PERIPHERAL BENZODIAZEPINE RECEPTOR (PBR)-TARGETED NEAR INFRARED PROBE FOR SCREENING A PRE-CLINICAL MODEL OF BREAST CANCER

Shelby Katherine Wyatt[1,2], H. Charles Manning[2,3], Mingfeng Bai[4], Stephanie N. Bailey[4], Pascal Gallant[5], Guobin Ma[5], Laura McIntosh[5], and Darryl J. Bornhop[4]

[1]Department of Biomedical Engineering, Vanderbilt University, Nashville, TN

[2]Vanderbilt University Institute of Imaging Sciences (VUIIS), Vanderbilt University, Nashville, TN

[3]Department of Neurological Surgery, Vanderbilt University, Nashville, TN

[4]Department of Chemistry, Vanderbilt University, Nashville, TN

[5]ART Advanced Research Technologies Inc., Saint-Laurent, Quebec, Canada

Abstract

Based on the observations that the peripheral benzodiazepine receptor (PBR) is overexpressed in breast cancer tissues combined with the fact that this expression profile appears to correlate with disease stage, aggressive phenotype and clinical prognosis, our laboratory and others have focused on the development of PBR-targeted molecular imaging agents for enhanced disease detection. Here we quantify the *in vitro* and *in vivo* uptake of a near infrared (NIR) PBR-targeted probe (NIR-conPK11195) in a human metastatic breast adenocarcinoma (MDA-MB-231) model of breast cancer. Fluorescence micrographs illustrate the effective labeling of MDA-MB-231 cells by NIR-conPK11195. Cellular uptake and competition assays provide further evidence of significant dose dependent ($p < 0.001$) and PBR-specific ($p < 0.001$) cellular uptake of NIR-conPK11195. By exploiting the NIR tissue transparency window and conPK11195 specificity it was possible to preferentially label MDA-MB-231 tumors *in vivo* with an 11-fold contrast enhancement over normal tissue ($p < 0.001$). Furthermore, the fluorescence signal due to NIR-conPK11195 accumulation was up to 7-fold greater than the free NIR dye and demonstrated statistical significance ($p < 0.001$). Overall, our results indicate that NIR-conPK11195 has the potential to be an effective PBR-targeted MI agent for breast cancer screening, while yielding valuable insights regarding the biological development and progression of the disease.

Introduction

The emerging field of molecular imaging (MI) aims to noninvasively, quantitatively and repetitively monitor biological processes *in vivo* to detect disease, probe its basis, and study relevant biochemical pathways at the molecular level (1). Since molecular targets (including cell surface and intracellular receptors, proteins, enzymes, DNA and RNA) undergo alterations prior to morphological or physical transformations, MI should aid in early detection and improved diagnosis of disease (1, 2). The use of MI may therefore result in improved clinical outcomes and enhanced long-term patient survival. In addition, the capability to monitor lesion physiology *in vivo* allows further characterization of disease, which may facilitate therapeutic efficacy monitoring, speed drug discovery, and potentially lead to patient-specific treatment regimens. Recently, the ability to specifically label tumor cells has allowed enhanced tumor margin definition and surgical resection guidance (3).

Optical MI, particularly in the near infrared (NIR) wavelength region, is an inexpensive technique that provides relatively high sensitivity without the use of ionizing radiation (2). Fluorescence imaging is rapid, allowing for dynamic, real-time monitoring of agent biodistribution and clearance profiles and is commonly performed concurrently on multiple animals in a relatively high-throughput manner. In addition, the use of multiple filters or a liquid crystal tunable filter allows spectral discrimination and the ability to sequentially monitor multiple optical reporters at different wavelengths (4). Although typical *in vivo* optical imaging performed at the anatomical scale tends to suffer from relatively low spatial resolution, photon penetration can be long when working in the NIR tissue transparency window ($\lambda \sim 650\text{-}900$ nm) (5). Here, photon absorption by hemoglobin and water is low, scattering is reduced and tissue autofluorescence is minimal, allowing photons to interrogate as much as centimeters of tissue (5, 6).

Exploitation of the tissue transparency window has led to the development of commercial optical imaging systems, such as the SoftScan platform for optical mammography, and clinical trials (7-16). The use of optical mammography, as an alternative or adjuvant screening methodology to conventional x-ray mammography, is noninvasive, does not necessarily require breast compression for imaging, and employs non-ionizing radiation. The lack of exposure to ionizing radiation is particularly important since some studies suggest that repeated exposure to x-rays may increase the incidence of breast cancers.

Current research in the field of NIR optical mammography has focused on the study of both intrinsic and extrinsic contrast mechanisms. Intrinsic tumor contrast measures of total, deoxy- and oxy-hemoglobin concentration provide functional information regarding vascularity and angiogenesis of the tumor as well as oxygen saturation and hypoxia (7-11). Tissue scattering and lipid content offer insight into structural complexity, cellularity and fibrosis (9, 10). Although these intrinsic characteristics have been correlated with malignancy and show clinical promise (7-11), the introduction of an exogenous contrast agent may provide enhanced specificity and sensitivity (12-16). In fact, results from Ntziachristos and colleagues indicate that physiologically relevant NIR agent concentrations can be detected through 10-12 cm of breast tissue (6). Furthermore, preliminary studies suggest that the administration of indocyanine green (ICG) may differentiate between diseased and normal human breast tissue *in vivo* (16). This contrast enhancement presumably results from the preferential extravasation of ICG through blood vessels with increased permeability, such as those found in tumor tissues (17).

Additional physiologically relevant information may be obtained by targeting exogenous contrast agents to biological processes such as MMP expression (18), or cellular or intracellular proteins such as the peripheral benzodiazepine receptor (PBR) (19, 20). PBR is a transmitochondrial membrane protein that is involved in a number of cellular process including steroidogenesis, cholesterol transport, cellular proliferation and apoptosis (21). Although PBR is naturally expressed at various levels in many normal tissues, PBR has been shown to be highly upregulated in a variety of neurodegenerative diseases and cancers including breast cancer (21-28). The overexpression of PBR even appears to correlate with aggressive phenotype (24) and the ability of some human metastatic breast cancer cells to grow in immunodeficient mice (25). Clinically, the overexpression of PBR appears to be a strong predictor of poor prognosis (26). Taken together, these observations indicate that conjugation of a signaling moiety to a high affinity PBR ligand should provide a MI agent that can be used to aid in enhancing tumor contrast *in vivo*, allowing earlier detection, diagnosis and further elucidation of disease.

A number of exogenous high affinity PBR ligands have been developed, including PK11195 (29), FGIN-1-27 (30), 2-phenylindolglyoxylamide derivatives (31), DAA1106 (32, 33), Ro 5-4864 (34), and SSR180575 (35, 36). Radiolabeled ^{3}H- and ^{11}C-PK11195 have even been used clinically for human imaging of glioma, neurodegenerative disease, and stroke [reviewed in (23)]. Since PK11195 is not conjugable in its native form, our laboratory developed a conjugable derivative (conPK11195), which has since been coupled to a number of imaging moieties (19, 20, 37, 38).

The utility of PBR-targeted optical MI agents for *in vitro* imaging and screening has been demonstrated in the literature (19, 20, 31, 37, 39). The fluorescent NBD-FGIN-1-27 (39) and 2-Phenylindolglyoxylamide-based (31) agents both appear to specifically label PBR in C6 rat glioma cells, but are limited for *in vivo* imaging due to the high autofluorescence of tissue, photon absorbance and scatter in the wavelength range of their excitation and emission profiles (~ 470 nm and ~ 540 nm, respectively). One major advantage of the lanthanide chelate-based PBR-targeted MI agent (Ln-conPK11195) is the ability to provide multiple spectroscopic signatures depending upon the chelated lanthanide ion (ex. Eu^{3+} for optical imaging or Gd^{3+} for magnetic resonance imaging) (20, 37). The fluorescent Eu^{3+}-conPK11195 compound also possesses inherent spectral resolution (~ 300 nm Stokes shift) and the capability to employ time-resolved imaging due to its long fluorescence lifetime (~ 500 μs) relative to endogenous chromophores (~ 4 ns) (40). However, ultraviolet (UV) excitation is necessary to sensitize the lanthanide luminescence, which limits the use of Eu^{3+}-conPK11195 *in vivo*. Finally, Lissamine-conPK11195 appears to be PBR specific and has been used for both live cell imaging and high-throughput *in vitro* screening assays (19). However, this compound also suffers from less than optimal absorbance and emission properties for noninvasive *in vivo* MI.

Recently our laboratory has described the effective use of a NIR PBR-targeted probe, NIR-conPK11195, for *in vivo* imaging of colonic tumors in $Smad3^{-/-}$ mice (38). Here we report the concurrent investigations regarding the use of NIR-conPK11195 for imaging of breast cancer that further expand upon the published study. Specifically, we demonstrate quantitative *in vitro* characterization of cellular uptake and PBR specificity as well as significant *in vivo* contrast enhancement by NIR-conPK11195 in the MDA-MB-231 mouse model of breast cancer.

Materials and Methods

Materials

The IRDye^{TM} 800CW NHS Ester dye and IRDye^{TM} 800-acid (designated here as "free NIR dye") were obtained from LI-COR Biosciences (Lincoln, NE). Dimethylsulfoxide (DMSO) was purchased from Fisher Scientific (Pittsburgh, PA). MDA-MB-231 cells were acquired from the American Type Culture Collection (ATCC; Manassas, VA). Calcium- and magnesium-free phosphate buffered saline (CMF-PBS), fetal bovine serum (FBS), and Leibovitz's L-15 media supplemented with 2 mM L-glutamine were obtained from Invitrogen Corporation (Carlsbad, CA). PK11195 was purchased from Sigma Aldrich (St. Louis, MI). Female BALB/c immunodeficient mice (8-9 weeks of age and weighing 15-20 g) were obtained from Charles River Canada Inc. (Lasalle, St-Constant, Quebec).

Synthesis and Characterization of NIR-conPK11195

IRDye^{TM} 800CW NHS ester (2 mg, 1.7 μmol) and the conjugable form of PK11195 (conPK11195; 2.5 mg, 6.6 μmol) were mixed in DMSO (5 mL) in a round bottom flask and stirred under argon flow for one hour. The reaction was monitored using HPLC analysis on a Varian Polaris C-18 column (250 × 4.6 mm) at a flow rate of 0.8 mL/min. Flow A was 20 mM tetrabutylammonium bromide in water and flow B was 20 mM tetrabutylammonium bromide in 90 % acetonitrile and 10 % water. The elution method for analytical HPLC started with a linear gradient from 100 % to 50 % A over ten minutes, held at 50 % A for five minutes, arrived at 10 % A in another ten minutes, held at 10 % A for ten minutes, and finally returned to 100 % A over two minutes. The elution profile was monitored by absorbance at 254 (unreacted conPK11195) and 780 nm. Product was purified by preparative HPLC using a Varian Polaris C-18 column (250 × 21.2 mm) at 17 mL/min. The collected solution was concentrated by vacuum rotary evaporation, frozen to -78ºC and dried under a freeze-dry system. The collected green solid was dissolved in DMSO and the undissolved tetrabutylammonium bromide was removed by centrifugation. The amount of NIR-conPK11195 was determined by absorption in DMSO solution at 797 nm (0.6 mg, 24 %). Note: The $\lambda_{ex,max}$ = 797 nm in DMSO and $\lambda_{ex,max}$ = 777 nm in CMF-PBS.

MS $(ESI)^+$ $[M+H]^+$ calcd 1366.4, found 1366.3. ^1H NMR 500MHz (MeOD) δ 8.55 (s, 1H), 8.10 (d, J=8.0 Hz, 1H), 7.97-7.89 (m, 2H), 7.85-7.77 (m, 7H), 7.67-7.46 (m, 7H), 7.33 (d, J=8.5 Hz, 1H), 7.24 (d, J=8.5 Hz, 1H), 7.15 (d, J=8.5 Hz, 2H), 6.25 (d, J=14.0 Hz, 1H), 6.14 (d, J=14.0 Hz, 1H), 4.15-4.10 (m, 2H), 4.08-4.04 (m, 2H), 3.44 (t, J=7.0 Hz, 2H), 3.17 (q, J=2.5 Hz, 5H), 3.12 (t, J=2.0 Hz, 2H), 3.01 (q, J=2.5 Hz, 5H), 2.89-2.85 (m, 2H), 2.77-2.69 (m, 4H), 2.15 (t, J=2.0 Hz, 2H), 2.03-2.00(m, 2H), 1.94-1.90 (m, 6H), 1.79-1.75 (m, 2H), 1.67-1.63 (m, 5H), 1.49-1.46 (m, 2H), 1.37 (d, J=4.5 Hz, 7H).

For spectroscopic characterization, the absorbance spectra of free NIR dye and NIR-conPK11195 were measured using a Shimadzu UV-VIS 1700 spectrophotometer (Columbia, MD) and the emission spectra were measured using a PTI Technologies spectrofluorometer (Oxnard, CA).

Cell Culture

The PBR overexpressing, human metastatic breast adenocarcinoma cell line (MDA-MB-231) was propagated in Leibovitz's L-15 medium supplemented with 2 mM L-glutamine, 10 % fetal bovine serum (FBS), and 1 % penicillin-streptomycin or 50 mg gentamicin in seal plug culture flasks (Corning; Corning, NY) at 37 °C and 95 % humidity. The medium was replaced every three days or as necessary. After attaining confluence, the cells were sub-cultured approximately 1:2 to 1:10.

In Vitro Fluorescence Microscopy

MDA-MB-231 cells (~100,000) were plated in parafilm-wrapped, collagen-coated glass bottom dishes (MatTek Corporation; Ashland, MA) 48 hours prior to experimentation. The cells were first washed once with warmed FBS-free medium and then incubated with 10 μM NIR-conPK11195 or free NIR dye for 30 minutes at 37 °C. Subsequently, the cells were washed three times with CMF-PBS, fixed in 4 % paraformaldehyde for one hour at room temperature and washed twice again with CMF-PBS. A Nikon Eclipse TE2000-U fluorescence microscope equipped with a mercury lamp, indocyanine green (ICG) filter set and a Hamamatsu ORCA II BT 512 camera controlled by Metamorph v6.1 (Molecular Devices Corporation; Downingtown, PA) was used for imaging.

In Vitro Uptake and Competition Studies

MDA-MB-231 cells were plated at 10,000 cells per well in 96 MicroWell™ Nunclon™Δ Optical Bottom Plates (Nalge Nunc International; Rochester, NY) and incubated under standard culture conditions for approximately 48 hours. Immediately prior to experimentation, the cells were washed once with 37 °C FBS-free medium to remove any dead cells and serum. The cells were then divided into four populations and evaluated in triplicate: (1) cells incubated with increasing concentrations of NIR-conPK11195 (1 nM, 4 nM, 7 nM, 10 nM, 40 nM, 70 nM, 100 nM, 400 nM, 700 nM, 1 μM) in FBS-free medium (100 μL volume), (2) cells simultaneously incubated with the same concentrations of NIR-conPK11195 and 100 μM PK11195, (3) cells incubated with the same concentrations of free NIR dye, and (4) undosed cells as blanks. Following a 30-minute incubation, the cells were gently washed twice with FBS-free medium and imaged on the Odyssey Infrared Imaging System (LI-COR Biosciences; Lincoln, NE) at 169 μm resolution, 3 mm focus offset, and 4.0, 8.0 and 10.0 intensity (gain) in the 800 nm channel. The average raw fluorescence intensity of each population ± standard deviation was then plotted in terms of NIR-conPK11195 or free NIR dye concentration; n = 3. The percent change in raw fluorescence intensity due to PK11195 competition was calculated as $\frac{FI_{blocked} - FI_{unblocked}}{FI_{unblocked}} * 100$ where FI ≡ raw fluorescence intensity.

Murine Model: Cell Implantation and Tumor Growth

The *in vivo* imaging studies were performed at LAB Pre-Clinical Research International Inc. (Montreal, Canada) under approved LAB protocols.

MDA-MB-231 cells were propagated until near confluency as described above. Cells were harvested by incubation with trypsin, pelleted by centrifugation, resuspended in sterile CMF-PBS, counted and assessed for viability (%) using trypan blue staining.

The cells were again pelleted by centrifugation, resuspended in sterile CMF-PBS at a concentration of 5 x 10^6 cells/100 μL and kept on ice. Prior to cell implantation, the cell-containing tube was gently inverted several times to assure proper cell distribution. Female BALB/c immunodeficient mice were finally injected with 5 x 10^6 MDA-MB-231 cells (100 μL volume) subcutaneously at the level of the right scapula.

In Vivo Imaging Studies

After approximately three weeks of tumor growth, the MDA-MB-231 tumor bearing mice were injected with four nmoles of either free NIR dye or NIR-conPK11195 in sterile saline via the tail vein (100 μL volume). The biodistribution and accumulation of the free NIR dye and PBR-targeted probe were monitored in real time using the eXplore Optix pre-clinical optical molecular imager (GE/ART Advanced Research Technologies Inc., Saint-Laurent, Quebec) equipped with an excitation laser tuned to 780 nm and an 830 nm long pass emission filter (Barr Associates; Westford, MA). Images were obtained preinjection and approximately 10 minutes, 1 hour, 4 hours, 6 hours, 12 hours, 24 hours, and 48 hours post-injection. Approximately 48 hours post-injection, the mice were sacrificed and tissues were harvested (kidneys, liver, brain, and tumors), imaged and fixed in 10 % formalin. The fixed tumors were then paraffin embedded, sliced and stained with hematoxylin and eosin (H & E) for histological characterization.

During the imaging sessions, the mice were kept on a heated animal support plate under general anesthesia by inhalation of 2.5 % isoflurane. All animals were supplied with Tears Naturale P.M. (Alcon, Mississauga, ON).

Throughout the study the step size, or spatial resolution, was maintained at 1.5 mm. However, the laser power (40 – 800 μW) and integration time (250 ms – 1 sec) were optimized at each individual time point using the peak value of the temporal point spread function (TPSF) to maximize the signal and avoid saturation. Thus, the fluorescence intensity was subsequently normalized to laser power and integration time to allow for direct comparison between mice and over time. For visualization purposes, images were smoothed using a linear interpolation algorithm in the OptiView Analysis Workstation software (ART Advanced Research Technologies, Inc).

The data were processed in MATLAB (Mathworks Inc, Boston, MA) using custom code (Guobin Ma, ART), which allows specific regions of interest (ROIs) to be manually defined and quantified in terms of normalized integrated TPSF intensity. For these studies, ROIs of equivalent size (9 mm x 6 mm) were drawn around the tumor itself and the opposite hind limb, defined as "normal" tissue. The average normalized integrated TPSF intensities (± standard deviation) for each group were then plotted as a function of time post-injection to generate time activity curves and monitor pharmacokinetics. To further determine tumor specificity, two contrast ratios were calculated: (1) the average ratio of the fluorescence intensity of the tumor regions relative to the normal tissue regions and (2) the ratio of the average fluorescence intensity of the tumors of the mice injected with NIR-conPK11195 relative to that of the tumors of the mice injected with free NIR dye.

Statistical Analysis

Statistical significance was determined using a one-way analysis of variance (ANOVA) test and the Holm-Sidak method for pairwise multiple comparisons with an overall significance level of 0.05 (SigmaStat v3.10); most results obtained $p < 0.001$.

Results and Discussion

The PBR-targeted NIR MI agent, NIR-conPK11195, was easily synthesized by coupling the IRDye^{TM} 800CW NHS Ester dye to the primary amine on the conPK11195 ligand previously developed in our laboratory [Figure 3.1A, B; (37)]. In CMF-PBS, NIR-conPK11195 exhibits an absorbance maximum centered at 777 nm with peak emission at 799 nm (λ_{ex} = 777 nm; Figure 3.1C). This spectroscopy is very similar to that of the IRDye^{TM} 800-acid (designated here as "free NIR dye"; λ_{abs} = 774 nm and λ_{em} = 796nm). The absorbance and fluorescence spectra for NIR-conPK11195 are red shifted

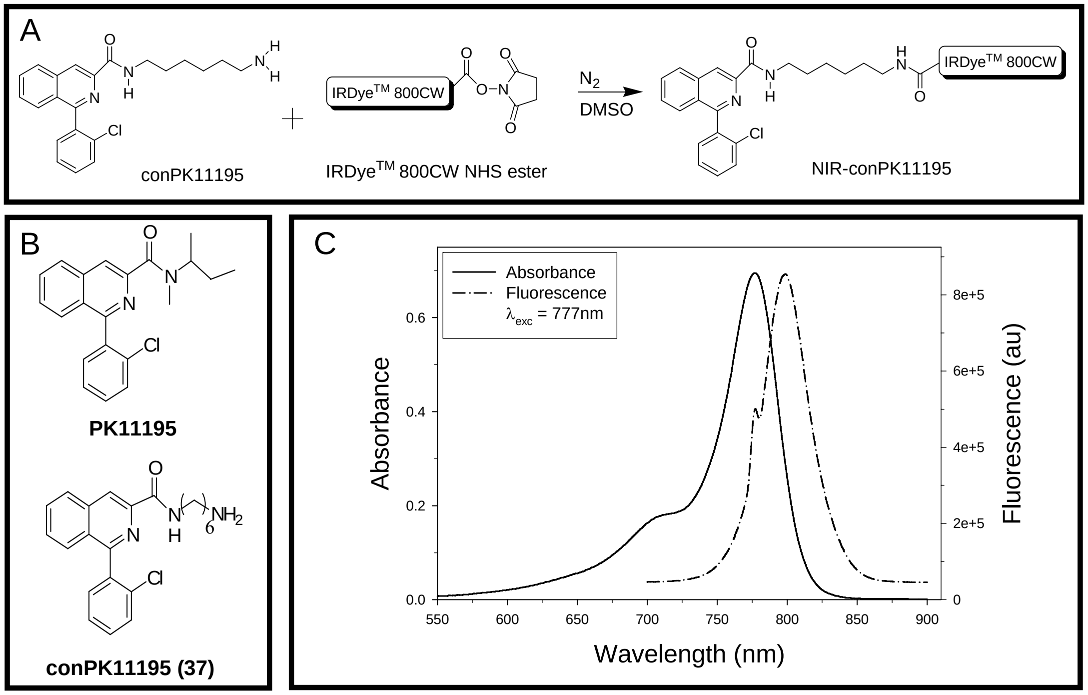

Figure 3.1. (A) Synthetic pathway, (B) relevant chemical structures and (C) spectroscopic properties of NIR-conPK11195 in CMF-PBS (λ_{ex} = 777nm).

by only 3 nm relative to the free NIR dye and the Stokes shift is 22 nm for both compounds, suggesting that the spectroscopic properties of IRDye^{TM} 800CW were not substantially altered by the conjugation of conPK11195. Furthermore, the NIR-conPK11195 spectroscopy falls directly within the NIR tissue transparency window and thus overcomes some of the major *in vivo* limitations of other fluorescent PBR-targeted agents (19, 20, 31, 37, 39).

To visualize cellular uptake of NIR-conPK11195 in comparison to free NIR dye, *in vitro* fluorescence microscopy was performed using PBR-overexpressing, human metastatic breast adenocarcinoma (MDA-MB-231) cells. The fluorescence micrograph in Figure 3.2A illustrates appreciable NIR fluorescence and cellular uptake of NIR-conPK11195. Using the same experimental conditions, instrument settings, and grayscale dynamic range, the cells incubated with free NIR dye exhibit

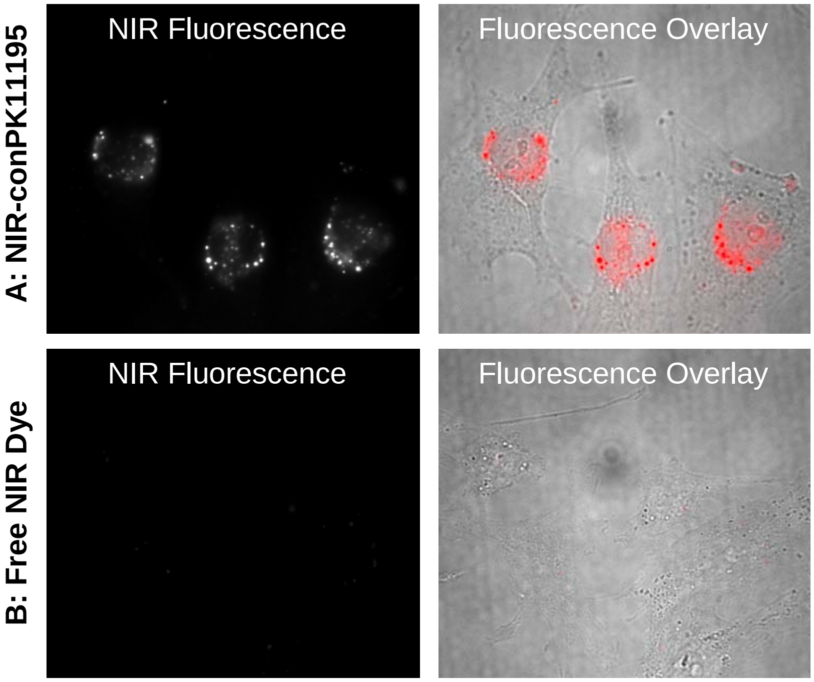

Figure 3.2. *In vitro* fluorescence microscopy illustrates appreciable NIR fluorescence and cellular uptake of NIR-conPK11195 (A), but not free NIR dye (B). MDA-MB-231 cells were incubated with 10 μM NIR-conPK11195 (A) or free NIR dye (B) for 30 minutes at 37°C in FBS-free medium. Pseudocolored fluorescence images overlaid onto the corresponding white light images also provide evidence of nuclear and perinuclear localization of NIR-conPK11195.

discernibly less fluorescence signal (Figure 3.2B). In addition, the fluorescence overlay in Figure 3.2A provides evidence that the NIR signal is emanating from the nuclear and perinuclear region of the NIR-conPK11195 dosed cells, as one would expect from the nuclear and mitochondrial location of PBR in MDA-MB-231 cells (24).

To further evaluate the cellular uptake and PBR-specificity of NIR-conPK11195, competitive binding assays were performed in a multiwell plate format. Figure 3.3 illustrates the significant (28-fold overall) increase in fluorescence intensity as a function of increasing NIR-conPK11195 concentration from 1 nM to 70 nM ($p < 0.001$; •). It is unlikely that the observed dose-dependent uptake is actually due to nonspecific binding

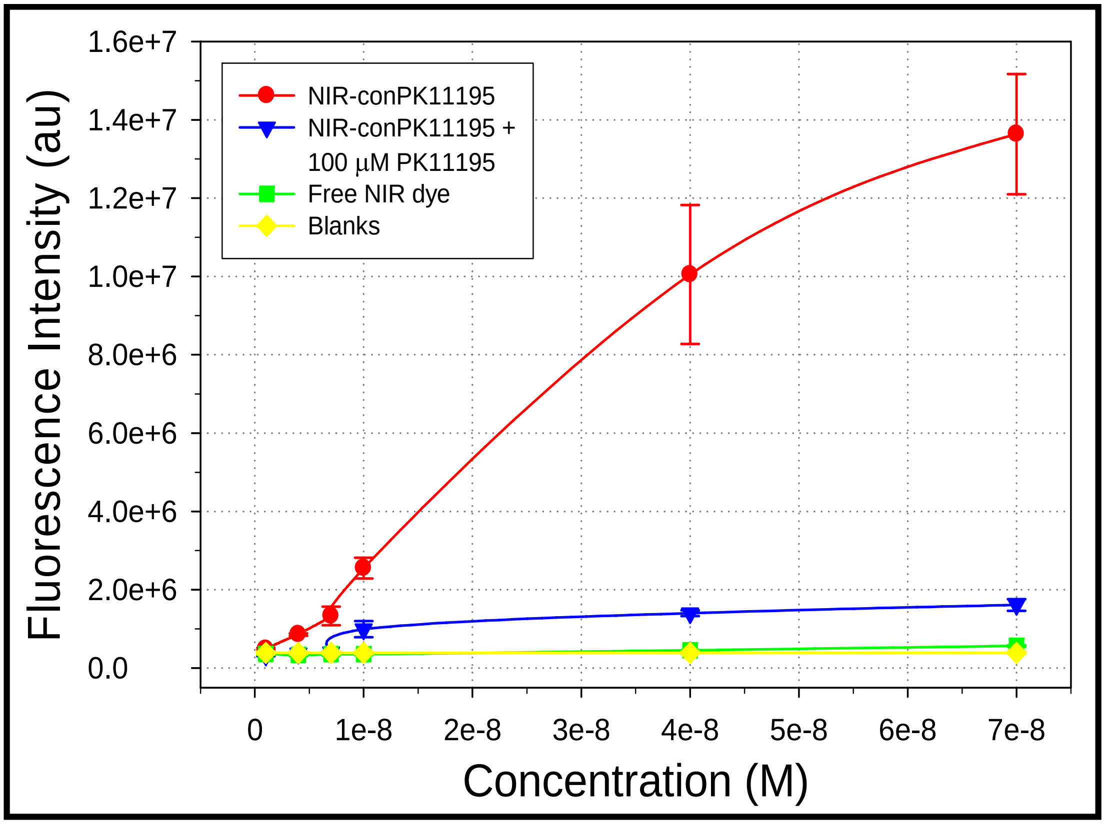

Figure 3.3. Cellular uptake and competition assays indicate significant dose dependent ($p < 0.001$) and PBR-specific ($p < 0.001$) cellular uptake of NIR-conPK11195. The average fluorescence intensity per well ± standard deviation as a function of NIR-conPK11195 concentration (unchallenged (•) or in the presence of 100 µM PK11195 (▼)) or free NIR dye concentration (■); undosed cells (◆) serve as a negative control for autofluorescence. n = 3 wells.

since the cells dosed with the non-targeted, free NIR dye (■) show significantly less fluorescence signal than those incubated with NIR-conPK11195 at each concentration ($p < 0.001$). In fact, the cells dosed with free NIR dye remain statistically indistinguishable from the undosed blanks (◆). Combined, these results suggest that the cellular uptake of NIR-conPK11195 is conPK11195-specific. In addition, the significant (33-88 %) attenuation of the fluorescence intensity due to the presence of the PK11195 ligand ($p < 0.001$; ▼) provides solid evidence for PBR-specificity.

Although the competition assay included concentrations ranging from 1 nM to 1 μM, the dynamic range of the Odyssey restricted the quantification of this assay to two orders of magnitude in incubation concentration for each of the three intensities scanned. The data presented in Figure 3.3 was acquired at an intensity setting of 10; all wells incubated with NIR-conPK11195 concentrations greater than 70 nM were saturated under these conditions and could therefore not be accurately quantified. At the lower intensity settings, higher dosages were quantifiable while the lower concentrations remained in the noise. The fluorescence intensity of the cells dosed with 100 nM to 1 μM NIR-conPK11195 increased dramatically as a function of concentration and was presumed to result from nonspecifically binding to the lipid membrane of the cells or perhaps another protein altogether (data not shown). However, more studies are necessary to determine the exact cause of this increased cellular uptake or association under these conditions.

In vivo imaging experiments were initiated after approximately three weeks of tumor growth. The normalized fluorescence images taken pre- and post-injection of NIR-conPK11195 and free NIR dye are shown in Figures 3.4A and 3.4B for qualitative visualization of the *in vivo* biodistribution, clearance and accumulation of the PBR-

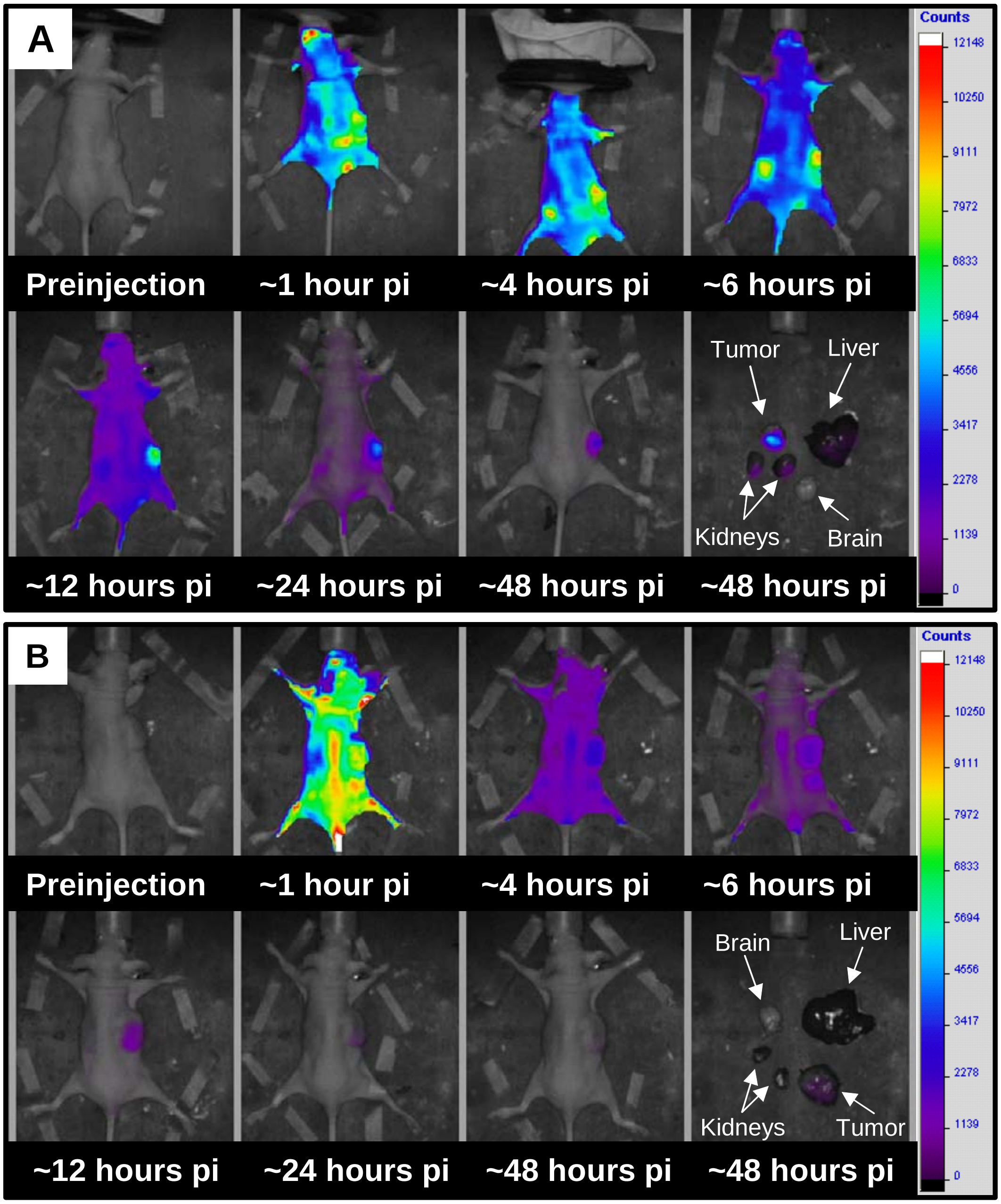

Figure 3.4. Direct comparison of the biodistribution and accumulation of the PBR-targeted NIR-conPK11195 (A) and free NIR dye (B) in tumor-bearing mice demonstrates significantly different clearance profiles and enhanced preferential labeling of MDA-MB-231 tumors *in vivo* by NIR-conPK11195. Fluorescence images were normalized to laser power and integration time, overlaid onto the corresponding white light images, and displayed in terms of normalized photon counts over 48 hours post-injection (pi). Images are representative of n = 3 mice per group.

targeted and non-targeted agents, respectively. Prior to injection, the mice are essentially devoid of fluorescence, revealing the negligible autofluorescence of tissue in the exploited wavelength region. Approximately 1 hour post-injection, both compounds exhibit fairly uniform distribution throughout the mice. Over time the free NIR dye clears primarily through the kidneys and demonstrates a more rapid clearance profile than NIR-conPK11195, which is cleared through both the renal and hepatobiliary systems. Ultimately, NIR-conPK11195 preferentially accumulates in the tumor regions to a significantly greater extent than the free NIR dye ($p < 0.001$ from 4 – 48 hours post-injection; quantitation discussed below). This enhanced fluorescence signal in the MDA-MB-231 tumors of the mice injected with NIR-conPK11195 is consistent with our *in vitro* observations of conPK11195- and PBR-specific cellular uptake of NIR-conPK11195.

Figure 3.5 further illustrates the ability to discriminate tumor from normal tissue at 48 hours post-injection due to the substantial signal enhancement of breast tumors from the PBR-targeted MI agent (A,C) over the free NIR dye (B,D). The tumor regions of the mice injected with free NIR dye (B,D) show some detectable fluorescence signal, presumably due to the enhanced permeability and retention (EPR) effect (17). However, the *in vivo* (A) and harvested (C) tumors of the mice injected with NIR-conPK11195 are on average 5-fold more intense ($p < 0.001$) than the mice injected with free NIR dye, and maintain significant tumor to normal contrast from 4 to 48 hours post-injection (quantitation discussed below).

To statistically evaluate the *in vivo* utility and effectiveness of our PBR-targeted NIR-conPK11195 agent, the fluorescence intensity of the tumor and normal (muscle)

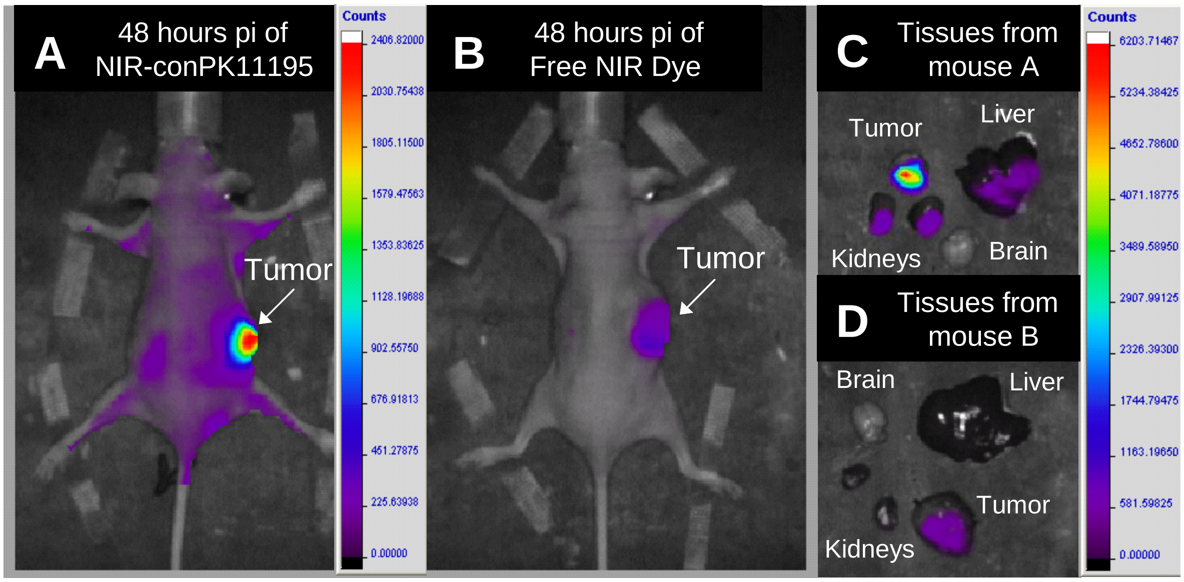

Figure 3.5. NIR-conPK11195 preferentially labels MDA-MB-231 tumors *in vivo*, substantially enhances the tumor-associated signal over free NIR dye and provides functional information without compromising the tumor to normal ratio (see Figure 3.6). (A, B) Fluorescence overlays of MDA-MB-231 tumor-bearing mice ~48 hours pi of NIR-conPK11195 and free NIR dye, respectively. (C, D) Fluorescence overlays of the tissues harvested from mouse A and B, respectively. Representative of n = 3 mice per group.

tissue regions were quantified in terms of normalized integrated TPSF intensity. Time activity curves generated from these measurements allow quantitative evaluation of the clearance rate and accumulation of NIR-conPK111195 and free NIR dye *in vivo*. Two noticeably distinct clearance profiles for NIR-conPK11195 (● tumor, ▼ normal) and free NIR dye (■ tumor, ◆ normal) are seen in Figure 3.6. More specifically, the time necessary to clear half of the maximum fluorescence intensity occurring at 10 minutes post-injection is ~10 hours for the NIR-conPK11195, but only ~3 hours for the free NIR dye (estimated from Figure 3.6). We attribute the differences in $t_{1/2}$ primarily to the targeting capabilities of NIR-conPK11195 and the polarity differences between the two agents. HPLC analysis indicates that free NIR dye is more hydrophilic than NIR-conPK11195 (data not shown), which should result in more rapid excretion from the blood stream. The increased lipophilicity of NIR-conPK11195 may also lead to more cellular membrane interactions than the free NIR dye.

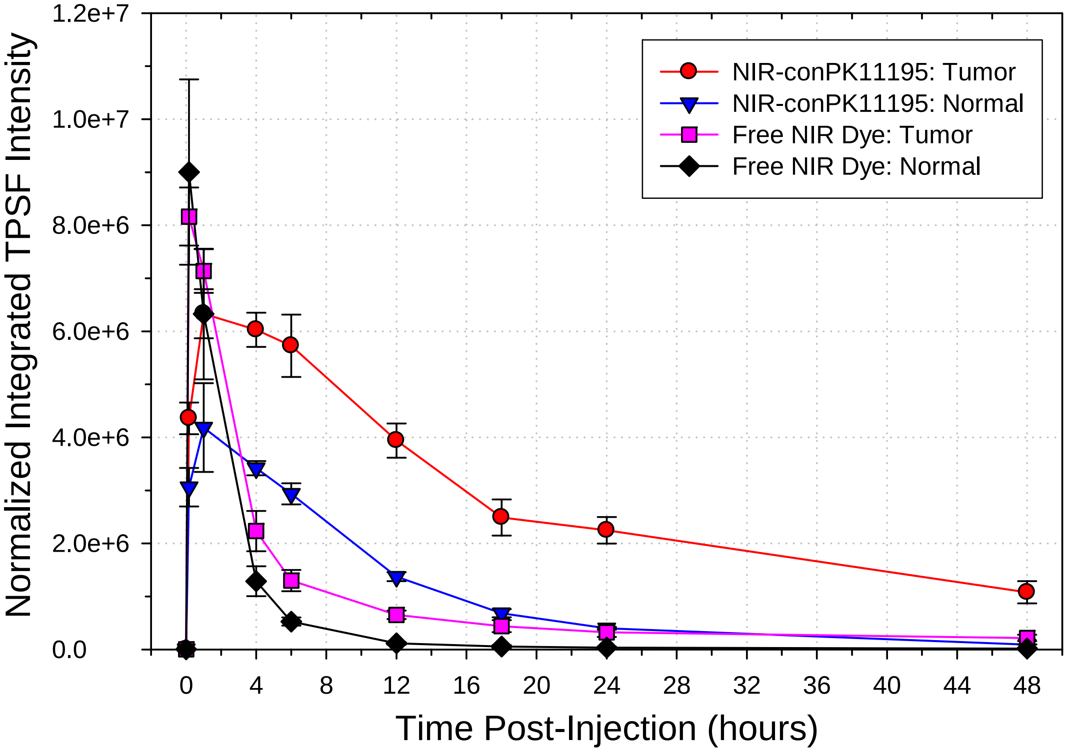

Figure 3.6. Time activity curves illustrate the distinct clearance profile of NIR-conPK11195 relative to free NIR dye, further demonstrate tumor specificity of NIR-conPK11195 *in vivo*, and reveal the significant signal enhancement resulting from the PBR-targeted NIR MI probe.

Figure 3.6 also illustrates the significant accumulation of NIR-conPK11195 in the tumor (●) relative to the normal muscle tissue (▼), as well as compared to the tumor (■) and normal (◆) tissue of the mice injected with free NIR dye. This tumor-specific accumulation of NIR-conPK11195 can be quantitatively expressed in terms of two contrast ratios: (1) Tumor:Normal Ratio – the fluorescence intensity of the tumor regions relative to the normal regions of the tumor-bearing mice and (2) PBR-targeted:Free Ratio - the average intensity of the tumors in mice injected with the PBR-targeted agent (NIR-conPK11195) relative to the average intensity of the tumors in mice injected with the free NIR dye (Table 1, Figure 3.7). The intensity in the tumor region due to accumulation of NIR-conPK11195 becomes significantly greater than the fluorescence intensity of the normal tissue four hours post-injection ($p < 0.001$), demonstrating preferential labeling of MDA-MB-231 tumors *in vivo*. The contrast enhancement steadily increases to 11-fold at 48 hours post-injection of NIR-conPK11195 and remains statistically significant ($p < 0.001$). Interestingly, the Tumor:Normal ratio for free NIR dye also increases to 11-fold as a function of time post-injection. This contrast, however, is most likely due to the EPR effect rather than tumor-targeting (17) and provides complementary information regarding the leakiness of the tumor vasculature. Furthermore, conjugation of the PK11195 analogue to the NIR dye provides a significant 3-7 fold contrast enhancement over the free NIR dye as demonstrated by the PBR-targeted/free contrast ratio (Table 1 and Figure 3.7; $p < 0.001$). This substantial signal enhancement not only provides tumor specificity over compound pooling and functional information regarding the suspected lesion, but also may allow for detection of smaller and/or deeper tumors.

Table 3.1. ROI Contrast Ratios

~ Time PI (hr)	NIR-conPK11195: Tumor/Normal[a]	Tumor: PBR-Targeted/Free[b]
0	1.0	0.8
0.2	1.4	0.5*
1	1.6	0.9
4	1.8*	2.7*
6	2.0*	4.4*
12	2.9*	6.0*
18	3.6*	5.7*
24	5.6*	7.0*
48	11.3*	4.9*

[a] The average ratio of the fluorescence intensity of the tumor region relative to the normal tissue region of mice injected with NIR-conPK11195

[b] The average fluorescence intensity of the tumor regions of the mice injected with NIR-conPK11195 relative to the average fluorescence intensity of the tumor regions of the mice injected with free NIR dye

* Statistically significant according to a one-way analysis of variance (ANOVA) test and the Holm-Sidak method of pairwise multiple comparisons with an overall significance level of 0.05

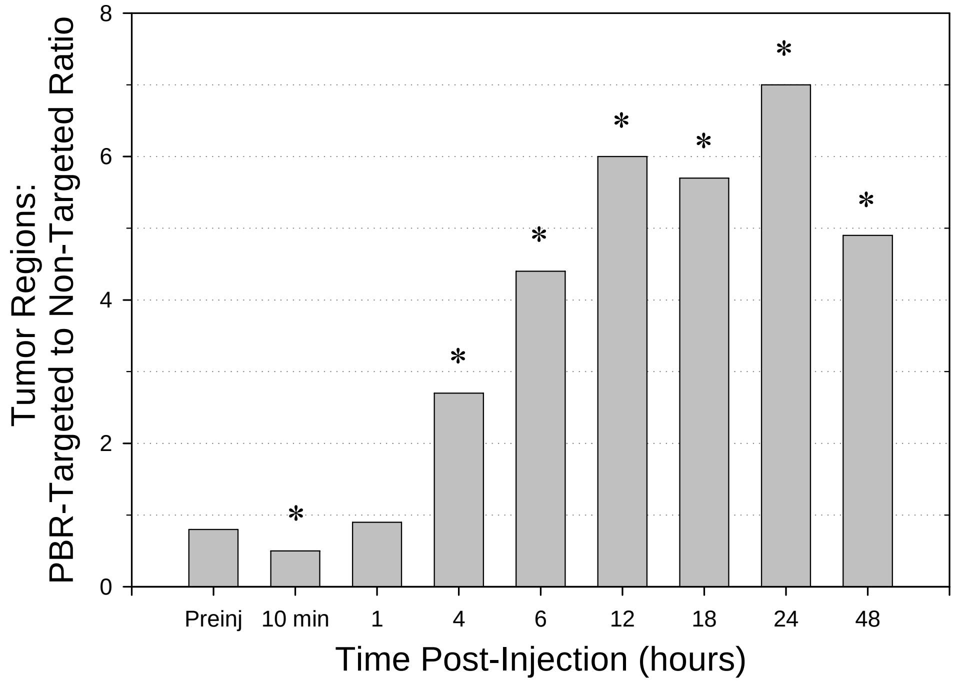

Figure 3.7. Graphical representation of the PBR-targeted to free NIR dye ratio demonstrating significant fluorescence signal enhancement from the NIR-conPK11195 relative to the free NIR dye. *$p < 0.001$

Overall, this study describes the utility of NIR-conPK11195 for *in vitro* and *in vivo* breast cancer screening and monitoring. The cellular uptake of NIR-conPK11195 can be visualized by fluorescence microscopy, quantified in live-cell competition assays, and monitored in an *in vivo* model of breast cancer. These studies demonstrate significant dose dependent ($p < 0.001$) and PBR-specific ($p < 0.001$) cellular uptake of NIR-conPK11195 *in vitro*. *In vivo*, NIR-conPK11195 provides an 11-fold contrast enhancement over normal tissue ($p < 0.001$) and a significant 7-fold improvement in fluorescence signal with respect to free NIR dye ($p < 0.001$). In theory, this signal enhancement could translate into increased sensitivity and therefore allow the detection of smaller and/or deeper tumors. NIR-conPK11195 will certainly prove useful in small animal models of disease to provide physiologically relevant information about tumor tissues as well as to facilitate therapeutic efficacy monitoring and drug discovery. In addition, the PBR-targeted NIR-conPK11195 may contribute to the development and clinical use of optical mammography.

Acknowledgements

The authors would like to acknowledge ART Advanced Research Technologies Inc. and the United States Army Department of Defense for financial support of this research as well as LI-COR Biosciences, Inc. for providing a portion of the dye used in this study.

References

1. Herschman, H. R. Molecular imaging: Looking at problems, seeing solutions. Science, *302:* 605-608, 2003.

2. Hengerer, A., Wunder, A., Wagenaar, D. J., Vija, A. H., Shah, M., and Grimm, J. From genomics to clinical molecular imaging. Proceedings of the Ieee, *93:* 819-828, 2005.

3. Stummer, W., Pichlmeier, U., Meinel, T., Wiestler, O. D., Zanella, F., Hans-Jurgen, R., and Grp, A.-G. S. Fluorescence-guided surgery with 5-aminolevulinic acid for resection of malignant glioma: a randomised controlled multicentre phase III trial. Lancet Oncology, *7:* 392-401, 2006.

4. Mansfield, J. R., Gossage, K. W., Hoyt, C. C., and Levenson, R. M. Autofluorescence removal, multiplexing, and automated analysis methods for in-vivo fluorescence imaging. Journal of Biomedical Optics, *10:* 041207, 2005.

5. Weissleder, R. A clearer vision for in vivo imaging. Nature Biotechnology, *19:* 316-317, 2001.

6. Ntziachristos, V., Ripoll, J., and Weissleder, R. Would near-infrared fluorescence signals propagate through large human organs for clinical studies? Optics Letters, *27:* 333-335, 2002.

7. Tromberg, B. J., Cerussi, A., Shah, N., Compton, M., Durkin, A., Hsiang, D., Butler, J., and Mehta, R. Imaging in breast cancer - Diffuse optics in breast cancer: detecting tumors in pre-menopausal women and monitoring neoadjuvant chemotherapy. Breast Cancer Research, *7:* 279-285, 2005.

8. Ntziachristos, V. and Chance, B. Probing physiology and molecular function using optical imaging: applications to breast cancer. Breast Cancer Research, *3:* 41-46, 2001.

9. Cerussi, A., Shah, N., Hsiang, D., Durkin, A., Butler, J., and Tromberg, B. J. In vivo absorption, scattering, and physiologic properties of 58 malignant breast tumors determined by broadband diffuse optical spectroscopy. Journal of Biomedical Optics, *11:* 044005, 2006.

10. Intes, X., Djeziri, S., Ichalalene, Z., Mincu, N., Wang, Y., St-Jean, P., Lesage, F., Hall, D., Boas, D., Polyzos, M., Fleiszer, D., and Mesurolle, B. Time-domain optical mammography SoftScan: Initial results. Academic Radiology, *12:* 1355-1355, 2005.

11. Zhu, Q., Cronin, E. B., Currier, A. A., Vine, H. S., Huang, M. M., Chen, N. G., and Xu, C. Benign versus malignant breast masses: Optical differentiation with US-guided optical imaging reconstruction. Radiology, *237:* 57-66, 2005.

12. Bremer, C., Ntziachristos, V., and Weissleder, R. Optical-based molecular imaging: contrast agents and potential medical applications. European Radiology, *13:* 231-243, 2003.

13. Ebert, B., Sukowski, U., Grosenick, D., Wabnitz, H., Moesta, T. K., Licha, K., Becker, A., Semmler, W., Schlag, P. M., and Rinneberg, H. Near-infrared fluorescent dyes for enhanced contrast in optical mammography: phantom experiments. Journal of Biomedical Optics, *6:* 134-140, 2001.

14. Godavarty, A., Thompson, A. B., Roy, R., Gurfinkel, M., Eppstein, M. J., Zhang, C., and Sevick-Muraca, E. M. Diagnostic imaging of breast cancer using fluorescence-enhanced optical tomography: phantom studies. Journal of Biomedical Optics, *9:* 488-496, 2004.

15. Ke, S., Wen, X. X., Gurfinkel, M., Charnsangavej, C., Wallace, S., Sevick-Muraca, E. M., and Li, C. Near-infrared optical imaging of epidermal growth factor receptor in breast cancer xenografts. Cancer Research, *63:* 7870-7875, 2003.

16. Ntziachristos, V., Yodh, A. G., Schnall, M., and Chance, B. Concurrent MRI and diffuse optical tomography of breast after indocyanine green enhancement. Proceedings of the National Academy of Sciences of the United States of America, *97:* 2767-2772, 2000.

17. Iyer, A. K., Khaled, G., Fang, J., and Maeda, H. Exploiting the enhanced permeability and retention effect for tumor targeting. Drug Discovery Today, *11:* 812-818, 2006.

18. McIntyre, J. O., Fingleton, B., Wells, K. S., Piston, D. W., Lynch, C. C., Gautam, S., and Matrisian, L. M. Development of a novel fluorogenic proteolytic beacon for in vivo detection and imaging of tumour-associated matrix metalloproteinase-7 activity. Biochemical Journal, *377:* 617-628, 2004.

19. Manning, H. C., Smith, S. M., Sexton, M., Haviland, S., Bai, M., Cederquist, K., Stella, N., and Bornhop, D. J. A peripheral benzodiazepine receptor targeted agent for in vitro imaging and screening. Bioconjugate Chemistry, *17:* 735-740, 2006.

20. Manning, H. C., Goebel, T., Thompson, R. C., Price, R. R., Lee, H., and Bornhop, D. J. Targeted molecular imaging agents for cellular-scale bimodal imaging. Bioconjugate Chemistry, *15:* 1488-1495, 2004.

21. Papadopoulos, V., Baraldi, M., Guilarte, T. R., Knudsen, T. B., Lacapere, J. J., Lindemann, P., Norenberg, M. D., Nutt, D., Weizman, A., Zhang, M. R., and Gavish, M. Translocator protein (18 kDa): new nomenclature for the peripheral-type benzodiazepine receptor based on its structure and molecular function. Trends in Pharmacological Sciences, *27:* 402-409, 2006.

22. Han, Z. Q., Slack, R. S., Li, W. P., and Papadopoulos, V. Expression of peripheral benzodiazepine receptor (PBR) in human tumors: Relationship to breast, colorectal, and prostate tumor progression. Journal of Receptors and Signal Transduction, *23:* 225-238, 2003.

23. Venneti, S., Lopresti, B. J., and Wiley, C. A. The peripheral benzodiazepine receptor (Translocator protein 18 kDa) in microglia: From pathology to imaging. Progress in Neurobiology, 2006.

24. Hardwick, M., Fertikh, D., Culty, M., Li, H., Vidic, B., and Papadopoulos, V. Peripheral-type benzodiazepine receptor (PBR) in human breast cancer: Correlation of breast cancer cell aggressive phenotype with PBR expression, nuclear localization, and PBR-mediated cell proliferation and nuclear transport of cholesterol. Cancer Research, *59:* 831-842, 1999.

25. Hardwick, M., Rone, J., Han, Z. Q., Haddad, B., and Papadopoulos, V. Peripheral-type benzodiazepine receptor levels correlate with the ability of human breast cancer MDA-MB-231 cell line to grow in SCID mice. International Journal of Cancer, *94:* 322-327, 2001.

26. Maaser, K., Grabowski, P., Sutter, A. P., Hopfner, M., Foss, H. D., Stein, H., Berger, G., Gavish, M., Zeitz, M., and Scherubl, H. Overexpression of the

peripheral benzodiazepine receptor is a relevant prognostic factor in stage III colorectal cancer. Clinical Cancer Research, *8:* 3205-3209, 2002.

27. Starosta-Rubinstein, S., Ciliax, B. J., Penney, J. B., Mckeever, P., and Young, A. B. Imaging of a Glioma Using Peripheral Benzodiazepine Receptor Ligands. Proceedings of the National Academy of Sciences of the United States of America, *84:* 891-895, 1987.

28. Black, K. L., Ikezaki, K., and Toga, A. W. Imaging of Brain-Tumors Using Peripheral Benzodiazepine Receptor Ligands. Journal of Neurosurgery, *71:* 113-118, 1989.

29. Benavides, J., Quarteronet, D., Imbault, F., Malgouris, C., Uzan, A., Renault, C., Dubroeucq, M. C., Gueremy, C., and Lefur, G. Labeling of Peripheral-Type Benzodiazepine Binding-Sites in the Rat-Brain by Using [3H]PK 11195, an Isoquinoline Carboxamide Derivative - Kinetic-Studies and Autoradiographic Localization. Journal of Neurochemistry, *41:* 1744-1750, 1983.

30. Romeo, E., Auta, J., Kozikowski, A. P., Ma, D., Papadopoulos, V., Puia, G., Costa, E., and Guidotti, A. 2-Aryl-3-Indoleacetamides (FGIN-1): a New Class of Potent and Specific Ligands for the Mitochondrial Dbi Receptor (MDR). Journal of Pharmacology and Experimental Therapeutics, *262:* 971-978, 1992.

31. Taliani, S., Simorini, F., Sergianni, V., La Motta, C., Da Settimo, F., Cosimelli, B., Abignente, E., Greco, G., Novellino, E., Rossi, L., Gremigni, V., Spinetti, F., Chelli, B., and Martini, C. New fluorescent 2-phenylindolglyoxylamide derivatives as probes targeting the peripheral-type benzodiazepine receptor: Design, synthesis, and biological evaluation. Journal of Medicinal Chemistry, *50:* 404-407, 2007.

32. Okuyama, S., Chaki, S., Yoshikawa, R., Ogawa, S., Suzuki, Y., Okubo, T., Nakazato, A., Nagamine, M., and Tomisawa, K. Neuropharmacological profile of peripheral benzodiazepine receptor agonists, DAA1097 and DAA1106. Life Sciences, *64:* 1455-1464, 1999.

33. Chaki, S., Funakoshi, T., Yoshikawa, R., Okuyama, S., Okubo, T., Nakazato, A., Nagamine, M., and Tomisawa, K. Binding characteristics of [H-3]DAA1106, a novel and selective ligand for peripheral benzodiazepine receptors. European Journal of Pharmacology, *371:* 197-204, 1999.

34. Newman, A. H., Lueddens, H. W. M., Skolnick, P., and Rice, K. C. Novel Irreversible Ligands Specific for Peripheral Type Benzodiazepine Receptors - (+/-) , (+) , and (-)-1-(2-Chlorophenyl)-N-(1-Methylpropyl)-N-(2-Isothiocyanatoethyl)-3-Isoquinolinecarboxamide and 1-(2-Isothiocyanatoethyl)-7-Chloro-1,3-Dihydro-5-(4-Chlorophenyl)-H-2-1,4-Benzodiazepin-2-One. Journal of Medicinal Chemistry, *30:* 1901-1905, 1987.

35. Ferzaz, B., Brault, E., Bourliaud, G., Robert, J. P., Poughon, G., Claustre, Y., Marguet, F., Liere, P., Schumacher, M., Nowicki, J. P., Fournier, J., Marabout, B., Sevrin, M., George, P., Soubrie, P., Benavides, J., and Scatton, B. SSR180575 (7-chloro-N,N,5-trimethyl-4-oxo-3-phenyl-3,5-dihydro-4H-pyridazino[4,5-b]indole-1-acetamide), a peripheral benzodiazepine receptor ligand, promotes neuronal survival and repair. Journal of Pharmacology and Experimental Therapeutics, *301:* 1067-1078, 2002.

36. Vin, V., Leducq, N., Bono, F., and Herbert, J. M. Binding characteristics of SSR180575, a potent and selective peripheral benzodiazepine ligand. Biochemical and Biophysical Research Communications, *310:* 785-790, 2003.

37. Manning, H. C., Goebel, T., Marx, J. N., and Bornhop, D. J. Facile, efficient conjugation of a trifunctional lanthanide chelate to a peripheral benzodiazepine receptor ligand. Organic Letters, *4:* 1075-1078, 2002.

38. Deane, N. G., Manning, H. C., Foutch, A. C., Washington, M. K., Aronow, B. A., Bornhop, D. J., and Coffey, R. J. Targeted Imaging of Colonic Tumors in Smad3-/-Mice Discriminates Cancer and Inflammation. Molecular Cancer Research, 2007.

39. Kozikowski, A. P., Kotoula, M., Ma, D. W., Boujrad, N., Tuckmantel, W., and Papadopoulos, V. Synthesis and biology of a 7-nitro-2,1,3-benzoxadiazol-4-yl derivative of 2-phenylindole-3-acetamide: A fluorescent probe for the peripheral-type benzodiazepine receptor. Journal of Medicinal Chemistry, *40:* 2435-2439, 1997.

40. Vereb, G., Jares-Erijman, E., Selvin, P. R., and Jovin, T. M. Temporally and spectrally resolved imaging microscopy of lanthanide chelates. Biophysical Journal, *74:* 2210-2222, 1998.

CHAPTER IV

PERIPHERAL BENZODIAZEPINE RECEPTOR (PBR)-TARGETED MOLECULAR IMAGING AGENTS FOR LABELING PRIMARY BRAIN TUMORS AND SECONDARY BREAST CANCER METASTASES TO THE BRAIN

Shelby Katherine Wyatt[1,2], H. Charles Manning[2,3], Moneeb M. Ehtesham[3], Khubaib Y. Mapara[3], Reid C. Thompson[3], and Darryl J. Bornhop[4]

[1]Department of Biomedical Engineering, Vanderbilt University, Nashville, TN

[2]Vanderbilt University Institute of Imaging Sciences (VUIIS), Vanderbilt University, Nashville, TN

[3]Department of Neurological Surgery, Vanderbilt University, Nashville, TN

[4]Department of Chemistry, Vanderbilt University, Nashville, TN

Abstract

Maximum surgical resection is predominantly believed to improve the clinical prognosis of primary brain tumors and secondary brain metastases. However, the extent of surgical resection is often compromised due to difficulties in accurately determining tumor location and ill-defined tumor boundaries as well as the desire to preserve eloquent normal brain tissue. In an effort to overcome some of the limitations of the commonly used image-guided surgery techniques, two PBR-targeted MI agents were assessed for their applicability to aid in primary brain tumor demarcation (Eu^{3+}-conPK11195) and the study of secondary brain metastases *in vivo* (NIR-conPK11195).

The use of Eu^{3+}-conPK11195 as a topical agent for labeling brain tumors was evaluated in an intracranial rat model of glioma. Preliminary imaging results demonstrate substantial localized fluorescence in the tumor-bearing hemisphere, while the contralateral normal brain is relatively devoid of fluorescence. These observations suggest that Eu^{3+}-conPK11195 preferentially bound to the tumor tissue over normal brain tissue and may therefore be useful for intraoperative labeling of gliomas. Next, the use of NIR-conPK11195 to study breast cancer metastases to the brain was evaluated in an intracranial breast cancer (MDA-MB-231) model of secondary brain metastases. *In vivo* imaging studies and quantitative time activity curves demonstrate distinct clearance profiles for NIR-conPK11195 and free NIR dye, resulting in preferential labeling of the MDA-MB-231-bearing hemisphere by NIR-conPK11195. Quantification of the tumor-to-normal and PBR-targeted-to-free contrast ratios further indicate that NIR-conPK11195 provides significantly enhanced fluorescence signal over the normal tissue ($p < 0.005$) and the non-targeted fluorophore ($p < 0.001$). Overall, these preliminary observations

indicate that PBR-targeted fluorescent agents may be useful in the management of primary brain tumors and secondary brain metastases.

Introduction

Both primary brain tumors and secondary brain metastases are often treated by maximum surgical resection followed by chemotherapy and/or radiation (1-4). Surgical resection provides cytoreduction of tumor mass as well as immediate symptomatic benefits including the reduction of intracranial hypertension, seizures and neurological deficits from the mass effect of the tumor (4, 5). Importantly, the extent of surgical resection is predominantly believed to correlate with improved clinical prognosis, increased time to recurrence and overall patient survival [reviewed in (1-4)]. However, the degree of surgical resection is often compromised due to difficulties in accurately determining tumor location and ill-defined tumor boundaries as well as the desire to preserve eloquent normal brain tissue.

A number of techniques have been employed to aid in intraoperative tumor localization in an attempt to perform more aggressive resections without inducing neurological deficits. Surgical navigation systems based on preoperative images are commonly used to intraoperatively guide tumor resections. However, the accuracy of these systems is limited by the sensitivity of the preoperative imaging modality [computed tomography (CT) or magnetic resonance imaging (MRI)] as well as spatial inaccuracies due to registration errors and intraoperative brain deformation (6, 7). The use of intraoperative ultrasound (iUS), intraoperative magnetic resonance imaging (iMRI) and intraoperative computed tomography (iCT) provide the advantage of real-time (or near-real time) feedback regarding tumor boundaries and extent of resection, but also possess associated disadvantages (6). Additional echogenic signals resulting from the contused brain, irrigation fluid and peritumoral edema decrease the accuracy of iUS, particularly as surgery progresses (8, 9). iMRI systems are expensive, not particularly compatible with standard operating room equipment, and limit patient access, while iCT systems expose the patient and neurosurgeons to ionizing radiation.

In an effort to overcome some of the limitations of the commonly used image-guided surgery techniques, a number of optical methods have also been explored for intraoperative brain tumor demarcation. Optical spectroscopy (OS) is an inexpensive, portable and easily integrated intraoperative imaging modality that detects spectral differences between diseased and normal tissue (10-12). While the sensitivity (80 – 100%) and specificity (76 – 93%) of current generation OS devices are useful, the small area of tissue interrogated by the probe (600 x 670 µm) and the short photon penetration depth (< 500 µm) limit its clinical incorporation, particularly for cancer screening applications (11, 12). In addition, the probe-based system requires tissue contact and only provides single-point spatial information. However, translation of probe-based optical spectroscopy to spectral imaging, which provides spectroscopic characterization at each pixel, has recently been explored (13). Several studies have also reported the use of exogenous agents for brain tumor demarcation including fluorescein (14, 15), indocyanine green (ICG) (16, 17), Cy5.5-CLIO (18, 19), and Quantum dots (Qdots) (20) as well as 5-aminolevulinic acid (ALA)-induced fluorescence (21-23). Although each of these agents appears to preferentially label tumor tissues and possesses unique advantages, they are also limited in their clinical applicability. These disadvantages include brief temporal contrast (fluorescein-based agents and ICG), potential toxicity (Qdots), and predominant uptake by tumor-infiltrating macrophages and microglia rather than tumor cells (Cy5.5-CLIO and Qdots). In addition, the short tissue penetration by fluorescein-based agents and ALA-induced porphyrin fluorescence may be beneficial for intraoperative surgical resection, but is a clear limitation for *in vivo* cancer screening applications. The use of targeted molecular imaging agents with time-resolved capabilities (for intraoperative surgical resection guidance) or NIR spectroscopy (for *in vivo* cancer screening) should overcome some of the aforementioned limitations and provide further functional information regarding the tumor phenotype.

The peripheral benzodiazepine receptor (PBR) represents an attractive target for imaging of both primary and secondary brain tumors since PBR has been shown to be upregulated in both glioblastomas (the predominant primary brain tumor) (24, 25) and breast cancer (the second most common origin site of brain metastases) (26, 27). Clinically, the expression of PBR appears to correlate with aggressive phenotype (27) and is a strong predictor of poor prognosis (28).

A number of exogenous PBR-targeting ligands (29-36) and fluorescence-based imaging agents (31, 37-40) have been synthesized. The lanthanide chelate-based Eu^{3+}-conPK11195 (37, 38) and near infrared (NIR) NIR-conPK11195 (41, 42) were developed in our laboratory. Both compounds possess unique advantages over previously reported agents. Eu^{3+}-conPK11195 offers high spectral resolution due to a large Stokes shift (~ 300 nm), can be detected with the naked eye, and is more resistant to photobleaching than typical organic fluorophores. The long fluorescence lifetime of Eu^{3+}-conPK11195 (~500 μsec) relative to endogenous compounds such as collagen, elastin and NADH (~4 ns) enables the use of time-resolved imaging or gated detection techniques and thus the capability to work in a low background regime (43). Combined, these spectroscopic properties suggest that Eu^{3+}-conPK11195 is particularly amenable to surgical resection guidance following topical application. On the other hand, NIR-conPK11195 (λ_{ex} = 777 nm and λ_{em} = 799 nm in saline) exploits the NIR tissue transparency window (44) to provide increased photon penetration and better signal localization as well as the ability to monitor *in vivo* disease progression in real-time (41, 42).

Previous studies have demonstrated cellular uptake and PBR-specificity of Eu^{3+}-conPK11195 and NIR-conPK11195 in C6 rat glioma cells (38) and MDA-MB-231 human metastatic breast adenocarcinoma cells (42), respectively. In addition, NIR-conPK11195 has been shown to preferentially label MDA-MB-231 cells *in vivo* with an 11-fold contrast enhancement over normal tissue and a 5- to 7-fold enhancement over free NIR dye (42). Here, we report an extension of these observations and exploit the unique spectroscopic characteristics of the two agents to demonstrate the potential applicability of using Eu^{3+}-conPK11195 as a topical agent for brain tumor demarcation and NIR-conPK11195 as a molecular imaging agent to study breast cancer metastases to the brain.

Materials and Methods

Materials

The IRDye® 800CW NHS Ester dye and IRDye® 800-acid (free NIR dye) were obtained from LI-COR Biosciences (Lincoln, Nebraska). Dimethylsulfoxide (DMSO) was purchased from Fisher Scientific (Pittsburgh, PA). MDA-MB-231 cells, C6 cells, and horse serum were acquired from the American Type Culture Collection (ATCC; Manassas, VA). Calcium- and magnesium-free phosphate buffered saline (CMF-PBS), Leibovitz's L-15 media supplemented with 2 mM L-glutamine, Dulbecco's Modified Eagle Medium (DMEM)-F12 medium, fetal bovine serum (FBS), and gentamicin sulfate were obtained from Invitrogen Corporation (Carlsbad, CA). Wistar rats and female athymic nude (nu/nu) mice were obtained from Charles Rivers Laboratories, Inc. (Wilmington, MA).

PBR-Targeted Molecular Imaging Agents

Eu^{3+}-conPK11195 (37) and NIR-conPK11195 (41, 42) were synthesized, purified and characterized as previously described. For spectroscopic characterization, the absorbance spectra of Eu^{3+}-conPK11195, free NIR dye and NIR-conPK11195 were measured using a Shimadzu UV-VIS 1700 spectrophotometer (Columbia, MD) and the emission spectra were measured using a PTI Technologies spectrofluorometer (Birmingham, NJ).

Cell Culture

C6 rat glioma cells were propagated in DMEM-F12 medium, 15% horse serum, 2.5% FBS, and 50 mg gentamicin sulfate in vented culture flasks (Corning; Corning, NY) at 37 °C, 5 % CO_2 and 95 % humidity. MDA-MB-231 (human metastatic breast adenocarcinoma) cells were propagated in Leibovitz's L-15 medium supplemented with 2 mM L-glutamine, 10% FBS, and 50 mg gentamicin in seal plug culture flasks at 37 °C and 95 % humidity. The medium was replaced every three days or as necessary. After attaining confluence, the cells were sub-cultured approximately 1:2 to 1:10.

Animal Models

Animal studies were performed under guidelines approved by the Institutional Animal Care and Use Committee (IACUC) at Vanderbilt University.

A rat model of glioma was prepared by intracranially implanting C6 cells into Wistar rats to evaluate the applicability of using Eu^{3+}-conPK11195 as a topical agent for brain tumor demarcation. A mouse model of breast cancer metastasis to the brain was prepared by intracranially implanting MDA-MB-231 cells into athymic nude (nu/nu) mice to evaluate the use of NIR-conPK11195 for studying metastases to the brain *in vivo* with the future potential for intraoperative surgical resection guidance.

First, an incision was made in the midline of the cranium and a 2-mm burr hole was drilled into the bone overlying the right hemisphere 2.5 mm anterior and 2.5 mm lateral to the bregma under microscopic guidance. C6 cells (1×10^5 in 5 μL sterile saline; Wistar rat) or MDA-MB-231 cells (1×10^6 cells in 4 μL of sterile saline; nu/nu mouse) were then stereotactically injected intracranially into the basal ganglia to a depth of 3 mm (rat) or 2 mm (mouse). Following injection, the skin was closed with sterile surgical staples, which were removed after seven days following confirmation of healing.

Imaging Studies

To evaluate the applicability of using Eu^{3+}-conPK11195 as a topical imaging agent for brain tumor demarcation, a craniotomy was first performed to expose the rat’s brain. Then, approximately 100 μL of 100 μM Eu^{3+}-conPK11195 was applied topically in a dropwise manner to the exposed tumor-bearing and contralateral normal brain hemispheres. Following a ten minute incubation, the rat's brain was washed three times with CMF-PBS and imaged with a simple imaging setup. An ultraviolet (UV) light curing system (SunSpot SM, Uvitron International; West Springfield, MA) equipped with a 100W mercury lamp was as used the excitation source. The excitation light traveled through a liquid core light guide and was filtered through a UG11 Schott filter (λ_{ex} = 320nm) directed onto the rat's brain. The emitted light was collected through an objective lens, passed through a TRITC/DiI emission filter (λ_{em} = 610/75 nm; Chroma; Rockingham, VT) and detected with the QImaging Micropublisher High Resolution Digital CCD Color Camera.

To evaluate the *in vivo* use of NIR-conPK11195 for studying breast cancer metastases to the brain, tumor-bearing and non-tumor-bearing mice were injected with 10 nmoles of either free NIR dye or NIR-conPK11195 in sterile saline via the tail vein (100 μL) two weeks post-implantation. The biodistribution and accumulation of the free NIR dye and PBR-targeted probe were monitored in real-time using the IVIS Imaging System 200 (Xenogen Corporation/Caliper LifeSciences; Alameda, CA) equipped with an indocyanine green (ICG) excitation and emission filter set (710 – 760 nm and 810 – 875 nm, respectively). Images were obtained pre-injection and approximately five minutes, 4.5 hours, 8.5 hours, 12.5 hours, and 24.5 hours post-injection using the following instrument settings: 7 seconds exposure time, medium binning (8 x 8 pixels), f/stop of 8 and FOV D (19.5 cm x 19.5 cm). The mice were then imaged longitudinally once a week for three consecutive weeks. On the fifth week post-implantation, the mice were sacrificed approximately 25 hours post-injection and the harvested brains, the remaining exposed head cavities and pieces of suspected tumor growth out of the brain (if applicable) were imaged using the same IVIS instrument parameters. The brains and suspected tumor tissues were fixed in 4% paraformaldehyde followed by ethanol dehydration. The fixed tissues were then paraffin embedded, sliced and stained with hematoxylin and eosin (H&E) for histological characterization.

During the imaging sessions, the mice were kept on a heated animal support plate under general anesthesia by inhalation of 2-3% isoflurane. Anesthesia was initiated in an induction chamber.

The data were processed in Living Image® Software Version 2.50 (Xenogen Corporation). Regions of interest (ROIs) of equivalent size were drawn over the tumor-bearing hemisphere and a normal (muscle) region defined on the hindlimb of the mice. The average total photon flux (photons/second) ± standard deviation for each group were plotted as a function of time post-injection to generate time-activity curves and to monitor clearance rate and accumulation of the PBR-targeted and non-targeted probes (n = 2-3). In addition, three contrast ratios were calculated to further determine tumor specificity: (1) the average ratio of the fluorescence intensity of the tumor-bearing hemisphere relative to the normal tissue, (2) the ratio of the average fluorescence intensity of the tumor-bearing hemispheres of the mice injected with NIR-conPK11195 to that of the tumor-bearing hemispheres of the mice injected with free NIR dye and (3) the ratio of the average fluorescence intensity of the tumor-bearing hemispheres of the tumor-bearing mice relative to the average fluorescence intensity of the "tumor" regions of the non-tumor-bearing control mice.

Statistical Analysis

Statistical significance was determined using a one-way analysis of variance (ANOVA) test and the Holm-Sidak method for pairwise multiple comparisons with an overall significance level of 0.05 (SigmaStat v3.10).

Results and Discussion

An intracranial rat glioma model was employed to evaluate the applicability of using a PBR-targeted lanthanide chelate-based molecular imaging agent (Eu^{3+}-conPK11195) to preferentially label brain tumor cells, with a potential application to intraoperative brain tumor demarcation. Preliminary imaging results following the topical application of Eu^{3+}-conPK11195 on a glioma-bearing rat's brain are shown in Figure 4.1. Substantial localized fluorescence is apparent in the tumor-bearing hemisphere as diagnosed by the attending neurosurgeon (Figures 4.1A,B). Conversely, the non-tumor-bearing hemisphere exhibits a relative lack of fluorescence signal (Figures 4.1C,D). To allow for better spatial orientation, the fluorescence images collected for the suspected tumor region is overlaid onto the white light image of the skull and brain (Figure 4.1E). Combined, these results suggest that the PBR-targeted lanthanide chelate-based MI agent preferentially bound to the tumor tissue over the contralateral normal brain tissue. Although more animal studies with additional histological characterization are necessary to confirm C6- and PBR-specific labeling by Eu^{3+}-conPK11195, these preliminary imaging results suggest that Eu^{3+}-conPK11195 may be useful for demarcation of gliomas, particularly for intraoperative surgical resection guidance.

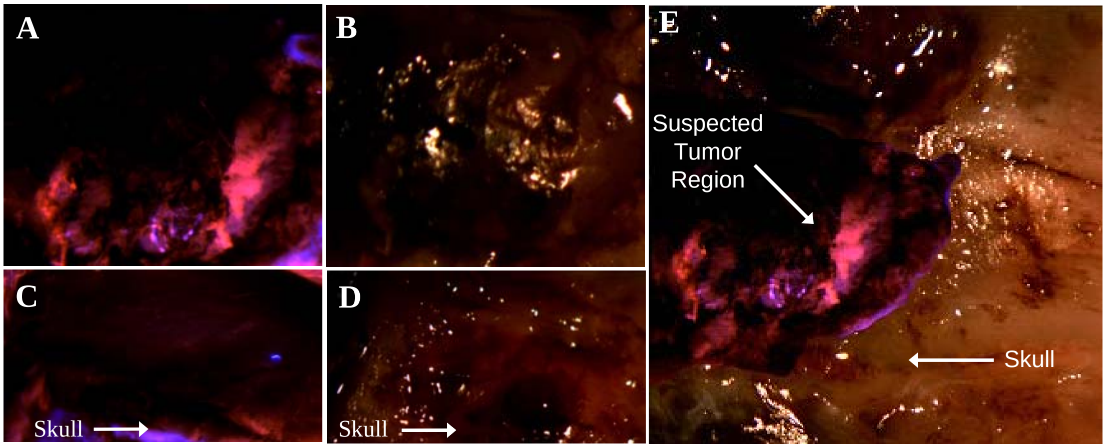

Figure 4.1. Fluorescence molecular imaging of a rat glioma model following topical Eu^{3+}-conPK11195 application for brain tumor demarcation. (A) Fluorescence and (B) white light images of the C6 glioma-bearing region of a rat's brain following topical application of Eu^{3+}-conPK11195. (C) Fluorescence and (D) white light images of the contralateral normal hemisphere following dosing with Eu^{3+}-conPK11195. (E) Overlay of the fluorescence images of the tumor region (A) and opposite normal hemisphere (C) onto the white light image of the skull and brain for spatial orientation.

The potential to use Eu^{3+}-conPK11195 to label tumor tissue is advantageous over previously reported intraoperative optical agents for several reasons. First, the PBR-specific Eu^{3+}-conPK11195 is a targeted imaging agent that provides physiological information regarding PBR expression levels, which have been shown to be indicative of clinical prognosis (28). In addition, the antenna-sensitized Eu^{3+} fluorescence is inherently spectrally resolved (Stokes shift ~ 300nm), and can be detected either with the naked eye or using simple instrumentation. Under the circumstances where enhanced detectability is necessary, the sensitivity could be further improved by exploiting the long fluorescence lifetime (on the order of ~ 500 μs) relative to endogenous compounds (~ 4 ns) and implementing gated imaging techniques to work in a low background regime. Finally, by substituting gadolinium (Gd^{3+}) for the Eu^{3+} ion, the Ln-conPK11195 complex could provide MRI contrast with T_1 relaxivity comparable to the commonly used MR agent Magnevist (38). Simultaneous delivery of a “cocktail” of the PBR-targeted fluorescent Eu^{3+}-conPK11195 and MR active Gd^{3+}-conPK11195 could potentially allow for bimodal imaging, which has been successfully demonstrated in *in vitro* C6 glioma cells (38).

Although Eu^{3+}-conPK11195 shows promise as a topical imaging agent for brain tumor demarcation (Figure 4.1) with the possibility of intraoperative surgical resection guidance, the capabilities of this probe for *in vivo* or deep tissue imaging are limited by the photon penetration depth in the wavelength range of its excitation and emission profiles (centered around 320 nm and 610 nm, respectively). Thus, we evaluated the applicability of using a NIR-labeled conPK11195 agent to label intracranial tumors *in vivo* to study breast cancer metastases to the brain. For this study, we stereotactially implanted MDA-MB-231 human metastatic breast adenocarcinoma cells into the brains of athymic nu/nu mice. Tumor-bearing and non-tumor-bearing mice were injected with 10 nmoles of NIR-conPK11195 or free NIR dye via the tail vein. The biodistribution, clearance rate and accumulation of the PBR-targeted and non-targeted probes were monitored in real-time using the IVIS Imaging System 200 equipped with an ICG filter set.

Fluorescence images taken approximately 25 hours post-injection of NIR-conPK11195 or free NIR dye are shown in Figures 4.2A-D, displayed on a color bar scale ranging from 0 to $1x10^8$ photons/sec/cm^2/sr. To further highlight the tumor specificity of NIR-conPK11195, the images from A-D are displayed on a smaller dynamic range ($7x10^7$ to $8.6x10^7$ photons/sec/cm^2/sr) in Figure 4.2E-H. The harvested brains from each of these mice (Figures 4.2I-L) as well as the exposed head cavities of mouse A (representative of tumor-bearing mice injected with NIR-conPK11195; Figure 4.2M) and mouse C (representative of non-tumor-bearing mice injected with NIR-conPK11195; Figure 4.2O) are also shown, displayed on a color bar scale ranging from 1.2×10^8 to 2.0×10^8 photons/sec/cm^2/sr. The head cavities of mice B (representative of tumor-bearing mice injected with free NIR dye) and D (representative of non-tumor-bearing mice injected with free NIR dye) are devoid of fluorescence and are not shown. Increased fluorescence intensity is apparent in the right tumor-bearing hemisphere of the mouse's brain twenty-five hours post-injection of NIR-conPK11195 (Figures 4.2A,E,I), suggesting preferential uptake of the PBR-targeted imaging agent by tumor tissue over the contralateral normal brain. Conversely, the non-tumor-bearing mouse injected with NIR-conPK11195 demonstrates fairly uniform residual fluorescence (Figure 4.2C) as well as a lack of fluorescence signal in the harvested brain (Figure 4.2G) ~ 25 hours post-injection. The uniformly distributed fluorescence intensity in the normal tissues of both the tumor-bearing (Figure 4.2A) and non-tumor-bearing (Figure 4.2C) mice injected with NIR-conPK11195 is similar in magnitude and presumably results from the ubiquitous expression of PBR, albeit significantly lower than that of MDA-MB-231 cells (26). In addition, the free NIR has cleared to approximately baseline levels from both the tumor-bearing (Figure 4.2B,F,J) and non-tumor-bearing (Figure 4.2D,H,L) mice injected with the non-targeted fluorophore.

The images in Figure 4.2 indicate preferential uptake of NIR-conPK11195 by the MDA-MB-231 tumor-bearing brain tissue over the contralateral (Figure 4.2A,E) and non-tumor-bearing normal brain (Figure 4.2C,G). In addition, the absence of fluorescence ~25 hours post-injection of free NIR dye in the tumor-bearing mice (Figure 4.2B,F)

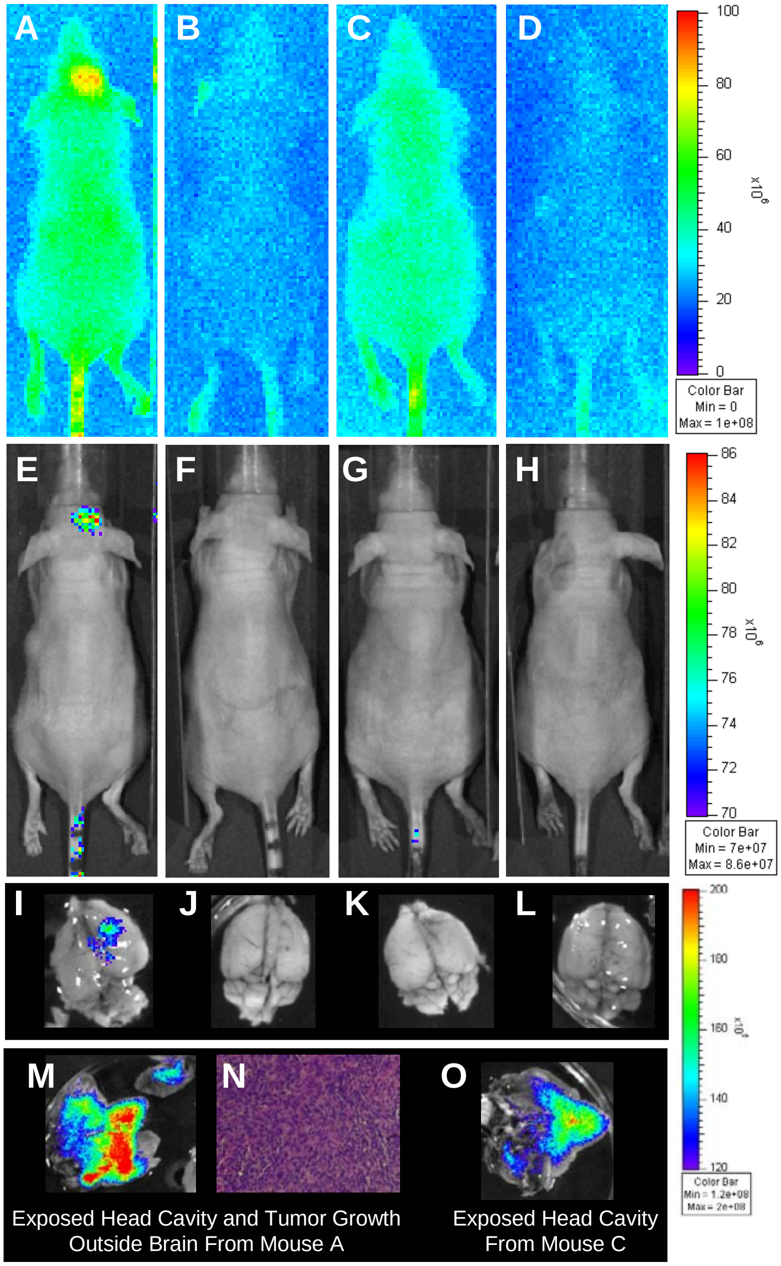

Figure 4.2. Fluorescence images and fluorescence overlays approximately 25 hours post-injection of NIR-conPK11195 or free NIR dye in tumor-bearing and non-tumor-bearing mice. (A) Tumor-bearing mouse injected with NIR-conPK11195, (B) Tumor-bearing mouse injected with free NIR dye, (C) Non-tumor-bearing mouse injected with NIR-conPK11195, (D) Non-tumor-bearing mouse injected with free NIR dye, (E-H) Images from A-D displayed on a smaller dynamic range to highlight the tumor-specificity of NIR-conPK11195, (I-L) Harvested brains from mice A-D, respectively, (M) Skull piece with tumor growth outside of brain and exposed head cavity from mouse A, (N) Histological characterization of the tumor growth outside of brain in M, (O) Exposed head cavity from mouse C.

indicates that the uptake of NIR-conPK11195 is conPK11195-specific rather than simply due to the enhanced permeability and retention effect (EPR) present in tumors (45). This observation is in agreement with previous studies that have demonstrated PBR-specificity of NIR-conPK11195 in *in vitro* MDA-MB-231 cells as well as an up to 7-fold contrast enhancement of *in vivo* MDA-MB-231 xenografts labeled with NIR-conPK11195 (42). However, the fluorescence signal in the *in vivo* mouse head (Figure 4.2A) appears to emanate from other tissues (Figure 4.2M) in addition to the tumor-bearing brain hemisphere (Figure 4.2I). At least some of this additional fluorescently-labeled tissue includes MDA-MB-231 tumor growth outside of the brain (seen attached to a piece of the mouse's skull in Figure 4.2M with histological characterization shown in Figure 4.2N). Low levels of uptake by the skin and normal tissues appear to be similar in magnitude to the normal uptake in non-tumor-bearing mice (Figure 4.2C,O). However, inflammation may also contribute to some of this uptake. Microglia, the major immune cells of the brain, and macrophages have been shown to upregulate PBR expression upon activation and as a function of certain central nervous system (CNS) disorders [reviewed in (46)]. Thus, ongoing and future studies are aimed at expanding the histological characterization to determine the exact cellular population that is taking up NIR-conPK11195.

To quantitatively evaluate the *in vivo* utility and effectiveness of our PBR-targeted NIR-conPK11195 agent to study breast cancer metastases to the brain, the fluorescence intensity of the right brain hemisphere and normal tissue (muscle) regions were quantified in terms of total photon flux (photons/second) using equivalently sized ROIs. Figure 4.3 displays the time activity curves generated from these measurements, allowing quantitative evaluation of the clearance rates and accumulation of NIR-conPK111195 and free NIR dye *in vivo*. In tumor-bearing mice, the time necessary to clear half of the maximum fluorescence intensity in the tumor regions was approximately ten hours for NIR-conPK11195 (Figure 4.3 ●, solid line) and approximately three hours for free NIR dye (Figure 4.3 ■, solid line); these clearance rates are in agreement with the previously reported clearance rates of NIR-conPK11195 and free NIR dye in MDA-MB-231 xenografts (42). However, the time necessary to clear half of the maximum fluorescence intensity in the equivalent "tumor" regions of the non-tumor-bearing mice

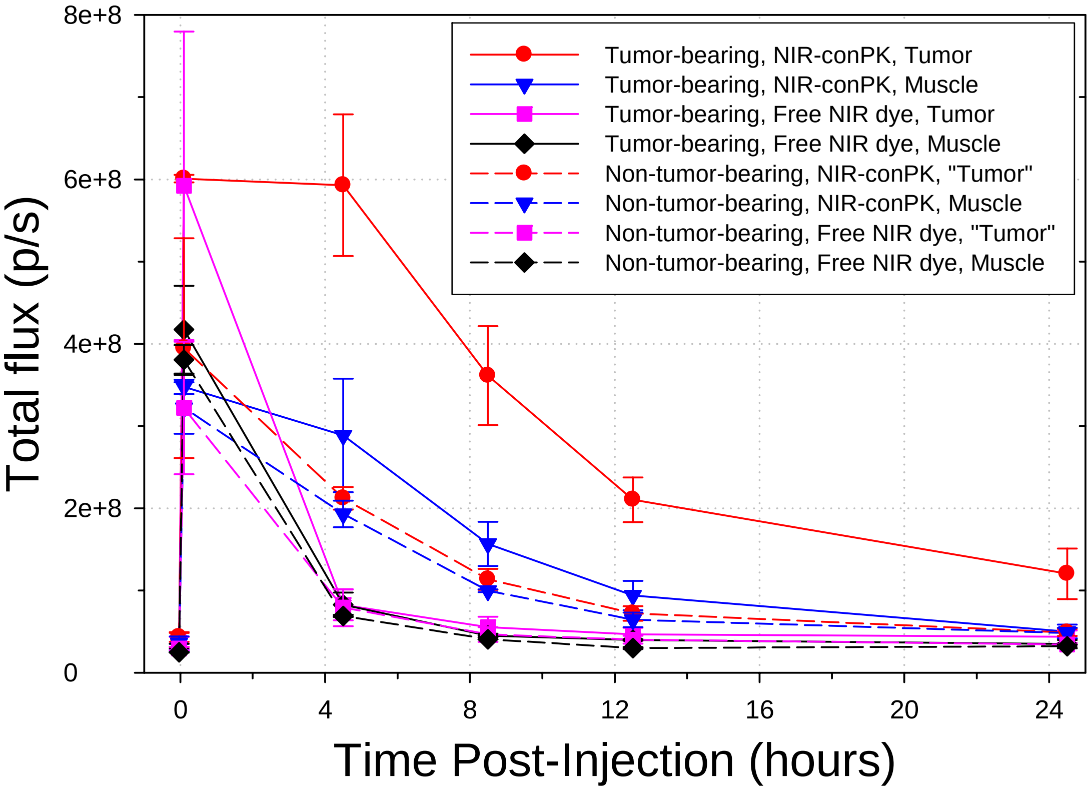

Figure 4.3. Time activity curves for intracranial MDA-MB-231 tumor-bearing (solid lines) and non-tumor-bearing (dashed lines) mice. (●) Tumor or equivalent "tumor" region of mice injected with NIR-conPK11195, (▼) Normal (muscle) region of mice injected with NIR-conPK11195, (■) Tumor or equivalent "tumor" region of mice injected with free NIR dye, (◆) Normal (muscle) region of mice injected with free NIR dye. The time activity curves illustrate distinct clearance profiles for NIR-conPK11195 and free NIR dye, demonstrate tumor specificity of NIR-conPK11195, and reveal the significant signal enhancement resulting from the PBR-targeted NIR MI agent.

was only ~5 hours for NIR-conPK11195; the $t_{1/2}$ of the free NIR dye was ~3 hours in both the tumor-bearing and non-tumor-bearing mice. Figure 4.3 also illustrates the significant accumulation of NIR-conPK11195 in the tumor-bearing hemispheres of the tumor-bearing mice (●, solid line) relative to their normal muscle tissue (▼, solid line) as well as the significant contrast enhancement compared to free NIR dye (solid lines, ■ and ♦). The statistical significance of the contrast enhancement can be evaluated by calculating three valuable contrast ratios: (1) Tumor/Normal: the average ratio of the fluorescence intensity of the tumor-bearing hemisphere relative to the normal (muscle) tissue, (2) PBR-Targeted/Free: the ratio of the average fluorescence intensity of the tumor-bearing hemispheres of the mice injected with NIR-conPK11195 relative to the average fluorescence intensity of the tumor-bearing hemispheres of the mice injected with free NIR dye and (3) Tumor/"Tumor": the ratio of the average fluorescence intensity of the tumor-bearing hemispheres of the tumor-bearing mice relative to the average fluorescence intensity of the equivalent "tumor" regions of the non-tumor-bearing control mice (Table 4.1).

The fluorescence intensity of the tumor regions of the intracranial tumor-bearing mice injected with NIR-conPK11195 becomes significantly greater than the normal muscle tissue approximately 4.5 hours post-injection ($p < 0.001$; Table 4.1 – Tumor:Normal Ratio). This significant tumor-specific contrast persists and increases to 2.4-fold at 24.5 hours post-injection ($p < 0.005$; Table 4.1). Conversely, the tumor/normal ratio of the tumor-bearing mice injected with free NIR dye is not statistically significant at any time point post-injection. Combined, these results indicate that the accumulation of NIR-conPK11195 is conPK11195-specific and not simply due to agent pooling and the EPR effect (45).

Table 4.1. Contrast ratios further demonstrate tumor-specificity of NIR-conPK11195.

Approx Time PI (hours)	Intracranial MDA-MB-231 Tumor-Bearing Mice			Non-Tumor-Bearing Mice			Tumor- vs Non-Tumor-Bearing Mice	
	NIR-conPK: Tumor/Normal[a]	Free NIR Dye: Tumor/Normal[a]	Tumor: PBR-Targeted/Free[b]	NIR-conPK: Tumor/Normal[a]	Free NIR Dye: Tumor/Normal[a]	Tumor: PBR-Targeted/Free[b]	NIR-conPK: Tumor/"Tumor" [c]	Free NIR dye: Tumor/"Tumor" [c]
0.1	1.7	1.4	1.0	1.2	0.9	1.2	1.5	1.8
4.5	2.1 *	1.0	7.2 *	1.1	1.1	2.7 *	2.8 *	1.0
8.5	2.3 *	1.2	6.5 *	1.1	1.1	2.4 *	3.2 *	1.2
12.5	2.3 *	1.2	4.5 *	1.1	1.3	1.8 *	2.9 *	1.2
24.5	2.4 *	1.3	2.7 *	1.0	1.1	1.4	2.5 *	1.3

[a] The average ratio of the fluorescence intensity of the tumor region relative to the normal region of individual mice

[b] The ratio of the average fluorescence intensity of the tumor regions of mice injected with NIR-conPK11195 relative to the average fluorescence intensity of mice injected with free NIR dye

[c] The ratio of the average fluorescence intensity of the tumor regions of tumor-bearing mice injected with NIR-conPK11195 relative to the average fluorescence intensity of the "tumor" regions of non-tumor-bearing control mice injected with NIR-conPK11195

* Statistically significant according to a one-way analysis of variance (ANOVA) test and the Holm-Sidak method for pairwise comparisons with an overall significance level of 0.05

The tumor-specific contrast enhancement due to the accumulation of NIR-conPK11195 is further demonstrated by comparing the tumor regions of the tumor-bearing mice injected with NIR-conPK11195 with those of the free NIR dye-injected tumor-bearing mice (Table 4.1 - PBR-targeted:Free Ratio). Immediately post-injection, the tumor regions of the tumor-bearing mice injected with NIR-conPK11195 and free NIR dye are equivalent (PBR-targeted/free = 1.0). Over time, however, NIR-conPK11195 is taken up, presumably binds to PBR and is retained to a significantly greater extent than the free NIR dye ($p < 0.001$; Table 4.1 – PBR-targeted:Free Ratio).

The non-tumor-bearing mice injected with either NIR-conPK11195 or free NIR dye demonstrate no appreciable accumulation of the PBR-targeted or non-targeted agents in the equivalent “tumor” regions; the tumor/normal ratios at all time points post-injection are approximately 1.1 (Table 4.1). The significant 1.8- to 2.7-fold increase in the fluorescence intensity of the “tumor” regions of the mice injected with NIR-conPK11195 relative to those injected with free NIR dye presumably results from the ubiquitous low levels of NIR-conPK11195 uptake (see also Figure 4.2C,D). As one might expect, the PBR-targeted/free ratios of the normal regions of the non-tumor-bearing mice also range from 1.5 – 2.8, suggesting that this slight enhancement is not due tumor-specific.

As a final measure of NIR-conPK11195 specificity, the tumor regions of tumor-bearing mice were compared to the equivalent “tumor” regions of the non-tumor-bearing controls. The tumor/“tumor” ratio of the mice injected with NIR-conPK11195 was significant from 4.5 to 24.5 hours post-injection and demonstrated an approximately 3-fold signal enhancement in the tumor-bearing mice relative to the non-tumor-bearing controls. Conversely, the free NIR dye tumor/“tumor” ratio remained statistically insignificant for the duration of the study. These results suggest similar clearance rates and lack of accumulation of free NIR dye in both tumor-bearing and non-tumor-bearing mice as well as tumor-specific uptake of NIR-conPK11195.

Although the NIR spectroscopy of NIR-conPK11195 enables increased tissue penetration over visible fluorescent agents (44), the detection limits of this technique and the contrast threshold necessary to discriminate tumor tissues should be addressed. All of the results discussed above were obtained five weeks post-implantation. At four weeks post-implantation, the fluorescence intensity of the tumor region was significantly greater (1.8-fold) than the normal tissue at 24 hours post-injection ($p < 0.01$), while the tumor/normal ratio for free NIR dye-injected tumor-bearing mice remained statistically insignificant at all time points post-injection (1.0- to 1.3-fold). However, at two and three weeks post-implantation, no contrast enhancement was appreciable in the tumor regions relative to the normal tissues. The lack of observable signal is likely dictated by the tumor size and location depth. Although larger tumors could be produced by implanting more cells, smaller tumors are more biologically relevant and of greater interest to our laboratories. As optical instrumentation improves, the *in vivo* imaging capabilities of this agent through the cranium should also improve. Nevertheless, NIR-conPK11195 may prove effective as an intraoperative imaging agent due to its significant sensitivity advantages over visible and/or non-targeted optical agents, previously demonstrated PBR-specificity, and ability to provide functional information regarding PBR expression profiles.

Overall, this study demonstrates (1) the potential use of Eu^{3+}-conPK11195 as a topical imaging agent for brain tumor demarcation and (2) the applicability of using a PBR-targeted NIR MI agent (NIR-conPK11195) in an intracranial MDA-MB-231 breast cancer model to study breast cancer metastases to the brain.

Acknowledgements

The authors would like to thank Dr. Dave Piston and Steve Head for the use of their fluorescence microscope, Dr. Masakazu Shiota for graciously assisting with the tail vein injections, and LI-COR Biosciences, Inc. for providing a portion of the dye used in this study. This research was supported by the National Science Foundation (NSF BES-0323281) and National Institutes of Health (NIH P20 GM072048-02).

References

1. Lefranc, F., Sadeghi, N., Camby, I., Metens, T., Dewitte, O., and Kiss, R. Present and potential future issues in glioblastoma treatment. Expert Review of Anticancer Therapy, *6:* 719-732, 2006.

2. Weil, R. J., Palmieri, D. C., Bronder, J. L., Stark, A. M., and Steeg, P. S. Breast cancer metastasis to the central nervous system. American Journal of Pathology, *167:* 913-920, 2005.

3. Nathoo, N., Toms, S. A., and Barnett, G. H. Metastases to the brain: current management perspectives. Expert Rev. Neurotherapeutics, *4:* 633-640, 2004.

4. Soffietti, R., Ruda, R., and Mutani, R. Management of brain metastases. Journal of Neurology, *249:* 1357-1369, 2002.

5. Toms, S. A., Ferson, D. Z., and Sawaya, R. Basic surgical techniques in the resection of malignant gliomas. Journal of Neuro-Oncology, *42:* 215-226, 1999.

6. Peters, T. M. Image-guidance for surgical procedures. Physics in Medicine and Biology, *51:* R505-R540, 2006.

7. Sinha, T. K., Miga, M. I., Cash, D. M., and Weil, R. J. Intraoperative cortical surface characterization using laser range scanning: Preliminary results. Neurosurgery, *59:* 368-376, 2006.

8. Leroux, P. D., Berger, M. S., Ojemann, G. A., Wang, K., and Mack, L. A. Correlation of Intraoperative Ultrasound Tumor Volumes and Margins with Preoperative Computerized-Tomography Scans - an Intraoperative Method to Enhance Tumor Resection. Journal of Neurosurgery, *71:* 691-698, 1989.

9. Sosna, J., Barth, M. M., Kruskal, J. B., and Kane, R. A. Intraoperative sonography for neurosurgery. Journal of Ultrasound in Medicine, *24:* 1671-1682, 2005.

10. Lin, W. C., Toms, S. A., Motamedi, M., Jansen, E. D., and Mahadevan-Jansen, A. Brain tumor demarcation using optical spectroscopy; an in vitro study. Journal of Biomedical Optics, *5:* 214-220, 2000.

11. Lin, W. C., Toms, S. A., Johnson, M., Jansen, E. D., and Mahadevan-Jansen, A. In vivo brain tumor demarcation using optical spectroscopy. Photochemistry and Photobiology, *73:* 396-402, 2001.

12. Toms, S. A., Lin, W. C., Weil, R. J., Johnson, M. D., Jansen, E. D., and Mahadevan-Jansen, A. Intraoperative optical spectroscopy identifies infiltrating glioma margins with high sensitivity. Neurosurgery, *57(4 Suppl):* 382-391, 2005.

13. Gebhart, S. C., Majumder, S. K., and Mahadevan-Jansen, A. Comparison of spectral variation from spectroscopy to spectral imaging. Applied Optics, *46:* 1343-1360, 2007.

14. Moore, G. E. Fluorescein as an agent in the differentiation of normal and malignant tissues. Science, *106:* 130-131, 1947.

15. Ichioka, T., Miyatake, S. I., Asai, N., Kajimoto, Y., Nakagawa, T., Hayashi, H., and Kuroiwa, T. Enhanced detection of malignant glioma xenograft by fluorescein-human serum albumin conjugate. Journal of Neuro-Oncology, *67:* 47-52, 2004.

16. Haglund, M. M., Hochman, D. W., Spence, A. M., and Berger, M. S. Enhanced optical imaging of rat gliomas and tumor margins. Neurosurgery, *35:* 930-941, 1994.

17. Haglund, M. M., Berger, M. S., and Hochman, D. W. Enhanced optical imaging of human gliomas and tumor margins. Neurosurgery, *38:* 308-317, 1996.

18. Kircher, M. F., Mahmood, U., King, R. S., Weissleder, R., and Josephson, L. A multimodal nanoparticle for preoperative magnetic resonance imaging and intraoperative optical brain tumor delineation. Cancer Research, *63:* 8122-8125, 2003.

19. Trehin, R., Figueiredo, J. L., Pittet, M. J., Weissleder, R., Josephson, L., and Mahmood, U. Fluorescent nanoparticle uptake for brain tumor visualization. Neoplasia, *8:* 302-311, 2006.

20. Popescu, M. A. and Toms, S. A. In vivo optical imaging using quantum dots for the management of brain tumors. Expert Review of Molecular Diagnostics, *6:* 879-890, 2006.

21. Stummer, W., Stocker, S., Wagner, S., Stepp, H., Fritsch, C., Goetz, C., Goetz, A. E., Kiefmann, R., and Reulen, H. J. Intraoperative detection of malignant gliomas by 5-aminolevulinic acid-induced porphyrin fluorescence. Neurosurgery, *42:* 518-525, 1998.

22. Stummer, W., Novotny, A., Stepp, H., Goetz, C., Bise, K., and Reulen, H. J. Fluorescence-guided resection of glioblastoma multiforme by using 5-aminolevulinic acid-induced porphyrins: a prospective study in 52 consecutive patients. Journal of Neurosurgery, *93:* 1003-1013, 2000.

23. Stummer, W., Pichlmeier, U., Meinel, T., Wiestler, O. D., Zanella, F., Hans-Jurgen, R., and Grp, A.-G. S. Fluorescence-guided surgery with 5-aminolevulinic acid for resection of malignant glioma: a randomised controlled multicentre phase III trial. Lancet Oncology, *7:* 392-401, 2006.

24. Starosta-Rubinstein, S., Ciliax, B. J., Penney, J. B., Mckeever, P., and Young, A. B. Imaging of a Glioma Using Peripheral Benzodiazepine Receptor Ligands. Proceedings of the National Academy of Sciences of the United States of America, *84:* 891-895, 1987.

25. Black, K. L., Ikezaki, K., and Toga, A. W. Imaging of Brain-Tumors Using Peripheral Benzodiazepine Receptor Ligands. Journal of Neurosurgery, *71:* 113-118, 1989.

26. Han, Z. Q., Slack, R. S., Li, W. P., and Papadopoulos, V. Expression of peripheral benzodiazepine receptor (PBR) in human tumors: Relationship to breast, colorectal, and prostate tumor progression. Journal of Receptors and Signal Transduction, *23:* 225-238, 2003.

27. Hardwick, M., Fertikh, D., Culty, M., Li, H., Vidic, B., and Papadopoulos, V. Peripheral-type benzodiazepine receptor (PBR) in human breast cancer: Correlation of breast cancer cell aggressive phenotype with PBR expression, nuclear localization, and PBR-mediated cell proliferation and nuclear transport of cholesterol. Cancer Research, *59:* 831-842, 1999.

28. Maaser, K., Grabowski, P., Sutter, A. P., Hopfner, M., Foss, H. D., Stein, H., Berger, G., Gavish, M., Zeitz, M., and Scherubl, H. Overexpression of the peripheral benzodiazepine receptor is a relevant prognostic factor in stage III colorectal cancer. Clinical Cancer Research, *8:* 3205-3209, 2002.

29. Benavides, J., Quarteronet, D., Imbault, F., Malgouris, C., Uzan, A., Renault, C., Dubroeucq, M. C., Gueremy, C., and Lefur, G. Labeling of Peripheral-Type Benzodiazepine Binding-Sites in the Rat-Brain by Using [3H]PK 11195, an Isoquinoline Carboxamide Derivative - Kinetic-Studies and Autoradiographic Localization. Journal of Neurochemistry, *41:* 1744-1750, 1983.

30. Romeo, E., Auta, J., Kozikowski, A. P., Ma, D., Papadopoulos, V., Puia, G., Costa, E., and Guidotti, A. 2-Aryl-3-Indoleacetamides (FGIN-1): a New Class of Potent and Specific Ligands for the Mitochondrial Dbi Receptor (MDR). Journal of Pharmacology and Experimental Therapeutics, *262:* 971-978, 1992.

31. Taliani, S., Simorini, F., Sergianni, V., La Motta, C., Da Settimo, F., Cosimelli, B., Abignente, E., Greco, G., Novellino, E., Rossi, L., Gremigni, V., Spinetti, F., Chelli, B., and Martini, C. New fluorescent 2-phenylindolglyoxylamide derivatives as probes targeting the peripheral-type benzodiazepine receptor: Design, synthesis, and biological evaluation. Journal of Medicinal Chemistry, *50:* 404-407, 2007.

32. Okuyama, S., Chaki, S., Yoshikawa, R., Ogawa, S., Suzuki, Y., Okubo, T., Nakazato, A., Nagamine, M., and Tomisawa, K. Neuropharmacological profile of

peripheral benzodiazepine receptor agonists, DAA1097 and DAA1106. Life Sciences, *64:* 1455-1464, 1999.

33. Chaki, S., Funakoshi, T., Yoshikawa, R., Okuyama, S., Okubo, T., Nakazato, A., Nagamine, M., and Tomisawa, K. Binding characteristics of [H-3]DAA1106, a novel and selective ligand for peripheral benzodiazepine receptors. European Journal of Pharmacology, *371:* 197-204, 1999.

34. Newman, A. H., Lueddens, H. W. M., Skolnick, P., and Rice, K. C. Novel Irreversible Ligands Specific for Peripheral Type Benzodiazepine Receptors - (+/-) , (+) , and (-)-1-(2-Chlorophenyl)-N-(1-Methylpropyl)-N-(2-Isothiocyanatoethyl)-3-Isoquinolinecarboxamide and 1-(2-Isothiocyanatoethyl)-7-Chloro-1,3-Dihydro-5-(4-Chlorophenyl)-H-2-1,4-Benzodiazepin-2-One. Journal of Medicinal Chemistry, *30:* 1901-1905, 1987.

35. Ferzaz, B., Brault, E., Bourliaud, G., Robert, J. P., Poughon, G., Claustre, Y., Marguet, F., Liere, P., Schumacher, M., Nowicki, J. P., Fournier, J., Marabout, B., Sevrin, M., George, P., Soubrie, P., Benavides, J., and Scatton, B. SSR180575 (7-chloro-N,N,5-trimethyl-4-oxo-3-phenyl-3,5-dihydro-4H-pyridazino[4,5-b]indole-1-acetamide), a peripheral benzodiazepine receptor ligand, promotes neuronal survival and repair. Journal of Pharmacology and Experimental Therapeutics, *301:* 1067-1078, 2002.

36. Vin, V., Leducq, N., Bono, F., and Herbert, J. M. Binding characteristics of SSR180575, a potent and selective peripheral benzodiazepine ligand. Biochemical and Biophysical Research Communications, *310:* 785-790, 2003.

37. Manning, H. C., Goebel, T., Marx, J. N., and Bornhop, D. J. Facile, efficient conjugation of a trifunctional lanthanide chelate to a peripheral benzodiazepine receptor ligand. Organic Letters, *4:* 1075-1078, 2002.

38. Manning, H. C., Goebel, T., Thompson, R. C., Price, R. R., Lee, H., and Bornhop, D. J. Targeted molecular imaging agents for cellular-scale bimodal imaging. Bioconjugate Chemistry, *15:* 1488-1495, 2004.

39. Manning, H. C., Smith, S. M., Sexton, M., Haviland, S., Bai, M., Cederquist, K., Stella, N., and Bornhop, D. J. A peripheral benzodiazepine receptor targeted agent for in vitro imaging and screening. Bioconjugate Chemistry, *17:* 735-740, 2006.

40. Kozikowski, A. P., Kotoula, M., Ma, D. W., Boujrad, N., Tuckmantel, W., and Papadopoulos, V. Synthesis and biology of a 7-nitro-2,1,3-benzoxadiazol-4-yl derivative of 2-phenylindole-3-acetamide: A fluorescent probe for the peripheral-type benzodiazepine receptor. Journal of Medicinal Chemistry, *40:* 2435-2439, 1997.

41. Deane, N. G., Manning, H. C., Foutch, A. C., Washington, M. K., Aronow, B. A., Bornhop, D. J., and Coffey, R. J. Targeted Imaging of Colonic Tumors in Smad3-/-Mice Discriminates Cancer and Inflammation (accepted for publication). Molecular Cancer Research, 2007.

42. Wyatt, S. K., Manning, H. C., Bai, M., Bailey, S. N., Gallant, P., Ma, G., McIntosh, L. M., and Bornhop, D. J. Optical Molecular Imaging Using a Peripheral Benzodiazepine Receptor (PBR)-Targeted Near Infrared Probe for Screening a Pre-Clinical Model of Breast Cancer (in preparation). In Preparation, 2007.

43. Vereb, G., Jares-Erijman, E., Selvin, P. R., and Jovin, T. M. Temporally and spectrally resolved imaging microscopy of lanthanide chelates. Biophysical Journal, *74:* 2210-2222, 1998.

44. Weissleder, R. A clearer vision for in vivo imaging. Nature Biotechnology, *19:* 316-317, 2001.

45. Iyer, A. K., Khaled, G., Fang, J., and Maeda, H. Exploiting the enhanced permeability and retention effect for tumor targeting. Drug Discovery Today, *11:* 812-818, 2006.

46. Venneti, S., Lopresti, B. J., and Wiley, C. A. The peripheral benzodiazepine receptor (Translocator protein 18 kDa) in microglia: From pathology to imaging. Progress in Neurobiology, 2006.

CHAPTER V

IN VITRO AND IN VIVO EVALUATION OF A POTENTIAL OPTICAL ANALOGUE TO 2-[^{18}F]FLUORO-2-DEOXY-D-GLUCOSE (^{18}FDG)

Shelby Katherine Wyatt[1,2], Mingfeng Bai[3], Stephanie N. Bailey[3], J. Oliver McIntyre[4], and Darryl J. Bornhop[3]

[1]Department of Biomedical Engineering, Vanderbilt University, Nashville, TN

[2]Vanderbilt University Institute of Imaging Sciences (VUIIS), Vanderbilt University, Nashville, TN

[3]Department of Chemistry, Vanderbilt University, Nashville, TN

[4]Department of Cancer Biology, Vanderbilt University, Nashville, TN

Introduction

The most commonly used radiopharmaceutical, 2-[^{18}F]fluoro-2-deoxy-D-glucose (^{18}FDG), is valuable in oncologic diagnostics and therapeutic efficacy monitoring based on its versatility and sensitive detection of increased metabolic activity by positron emission tomography (PET) (1, 2). The preferential uptake and accumulation of ^{18}FDG in cancerous tissues results from increased glycolysis by tumor cells as well as the upregulation of glucose transporter proteins (GLUTs) and the presence of a highly active hexokinase. The cellular uptake of ^{18}FDG occurs via these GLUTs. Once internalized, ^{18}FDG is phosphorylated by hexokinase to ^{18}FDG-6-phosphate in a similar manner as glucose. However, unlike the glucose metabolite, ^{18}FDG-6-phosphate cannot be further metabolized due to the lack of a hydroxyl group at the C-2 position, resulting in intracellular accumulation of ^{18}FDG-6-phosphate and PET signal that can serve to detect tumors (1, 2).

While ^{18}FDG-PET has inherently high sensitivity and demonstrated clinical applicability, the imaging technique has several limitations. These drawbacks include exposure to ionizing radiation, difficulty of compound synthesis, requirement of a local cyclotron, short halflife of ^{18}F (110 minutes) and relatively low spatial resolution. In an effort to overcome some of the major limitations of PET, our laboratory and others have developed potential optical analogues of ^{18}FDG including 2-[N-(7-nitrobenz-2-oxa-1,3-diazol-4-yl)amino]-2-deoxy-D-glucose [2-NBDG] (3-8), pyropheophorbide 2-deoxyglucosamide [Pyro-2DG] (9, 10), fluorescent dendritic arrays of glucosamine (11), and Cy5.5-D-glucosamine [Cy5.5-2DG] (12).

Yoshioka *et al* developed the first fluorescent D-glucose derivative, 2-NBDG, and demonstrated D-glucose but not L-glucose inhibition of cellular uptake (3). In addition, mass spectrometry indicated intracellular phosphorylation of 2-NBDG to 2-NBDG-6-phosphate (3-8). Combined, these results suggest that 2-NBDG is taken up and accumulated via the GLUT/hexokinase pathway. However, the spectroscopic properties (λ_{ex} = 475 nm and λ_{em} = 550 nm) render the 2-NBDG probe a poor choice for *in vivo* imaging.

Several more recent studies have attempted to develop D-glucose analogues suitable for *in vivo* imaging by capitalizing on the increased sensitivity and photon penetration depth in the near infrared (NIR) tissue transparency window (13). Pyro-2DG, which functions as both a NIR imaging and photodynamic therapy agent, demonstrated enhanced tumor uptake relative to the surrounding muscle tissue (9, 10). Preliminary confocal microscopy studies suggest that the uptake of Pyro-2DG is GLUT-specific, since D-glucose appears to competitively inhibit cellular localization of Pyro-2DG but not Pyro-acid (9). Using an alternative approach, Ye *et al* synthesized dendritic arrays of glucosamine based on an inner NIR carbocyanine core (11). Although the number of glucosamines (1, 2, 3, 4, 6, or 8) conjugated to the multicarboxylate probe does not appear to correlate with tumor uptake, each of the dendritic glucosamine arrays provided some tumor signal. The mechanisms of uptake and accumulation of the glucosamine-containing cypate derivatives, however, remain unknown. Interestingly, Cheng *et al* reported that another NIR deoxyglucose analogue (Cy5.5-2DG) does not appear to follow the GLUT/hexokinase pathway and provides significantly less contrast enhancement than the free Cy5.5 N-hydroxysuccinimide ester dye (12). The authors hypothesize that the dye characteristics are responsible for the differing behaviors of 2-NBDG and Cy5.5-2DG and suggest careful selection of NIR fluorophores for particular biological applications.

Based on the literature precedence regarding optical analogues to ^{18}FDG, our laboratory has developed an alternative NIR deoxyglucose analogue by conjugating D-glucosamine to IRDye^{TM} 800CW. The IRDye^{TM} 800CW is a cyanine-like dye that is highly water soluble and relatively stable. IRDye^{TM} 800CW capitalizes on the increased photon penetration in the NIR tissue transparency window and is slightly red-shifted relative to Cy5.5. This red-shift in excitation and emission eliminates the fluorescence contribution from the autofluorescence of typical alfalfa-based rodent chow, which is often seen in the Cy5.5 wavelength region, and is more suitable for *in vivo* imaging (14). Here, we report the *in vitro* and *in vivo* characterization of NIR-glucosamine in an SW480*neo* mouse model of human colon cancer that corroborates and expands upon the recent results reported for Cy5.5-2DG (12).

Materials and Methods

Materials

The IRDye^{TM} 800CW NHS Ester dye and IRDye^{TM} 800-acid (designated here as “free NIR dye”) were obtained from LI-COR Biosciences (Lincoln, NE). Sodium methoxide, glucosamine hydrochloride, D-(+)-glucose monohydrate, and cytochalasin B were purchased from Fluka/Sigma Aldrich (St. Louis, MO). Dimethylsulfoxide (DMSO) was purchased from Fisher Scientific (Pittsburgh, PA). SW480 (human colorectal adenocarcinoma) cells were acquired from the American Type Culture Collection (ATCC;

Manassas, VA). Calcium- and magnesium-free phosphate buffered saline (CMF-PBS), Dulbecco's Modified Eagle Medium (DMEM), fetal bovine serum (FBS), and gentamicin sulfate were obtained from Invitrogen Corporation (Carlsbad, CA). Female athymic nude (nu/nu) mice (6 weeks of age) were obtained from Harlan Sprague Dawley (Indianapolis, IN).

Synthesis of NIR-glucosamine

A mixture of sodium methoxide (9.3 mg, 0.17 mmol) and D-glucosamine hydrochloride (37 mg, 0.17 mmol) in DMSO (2 mL) was stirred at room temperature for two hours. 150 μL of this mixture (12.9 μmol) was added to a stirring solution of IRDye^{TM} 800CW NHS Ester dye (5mg, 4.3 μmol) in DMSO (9.85 mL). The mixture was stirred in the dark under argon positive pressure flow overnight.

HPLC analysis was performed to monitor the reaction on a Varian Polaris C-18 column (250 × 4.6 mm) at a flow rate of 0.8 mL/min. Flow A was 0.1% TEA in water and flow B was 0.1% TEA in acetonitrile. The elution method for analytical HPLC started with a linear gradient from 100% to 80% A over 30 minutes, then from 80% to 50% A for 5 minutes, arrived at 20% A in another 3 minutes, held at 20% A for 10 minutes, and finally returned to 100% A over 1 minute. The elution profile was monitored by UV absorbance at 254 and 780 nm. Product was purified by preparative HPLC using a Varian Polaris C-18 column (250×21.2 mm) at 17 mL/min. The collected solution was concentrated by vacuum rotary evaporation, frozen to -78ºC and dried under freeze-dry system. The amount of NIR-glucosamine was determined by absorption in DMSO solution at 780 nm (3.5 mg, 66%).

MS $(ESI)^+$ $[M+H]^+$ calcd 1162.3, found 1162.2. ^{1}H NMR 400MHz (MeOD) δ 8.02-7.93 (m, 2H), 7.88-7.80 (m, 6H), 7.36 (d, J=8.4 Hz, 1H), 7.28 (d, J=8.4 Hz, 1H), 7.19 (d, J=8.8 Hz, 2H), 6.29 (d, J=14.4 Hz, 1H), 6.19 (d, J=14.0 Hz, 1H), 5.08 (d, J=3.2 Hz, 1H), 4.20-4.14 (m, 2H), 4.10 (t, J=6.8 Hz, 2H), 3.89-3.58 (m, 5H), 3.06-3.01 (m, 2H), 2.92-2.86 (m, 2H), 2.82-2.75 (m, 2H), 2.28-2.22 (m, 2H), 2.08-2.05 (m, 2H), 2.00-1.91 (m, 5H), 1.80-1.79 (m, 2H), 1.71-1.68 (m, 3H), 1.40 (s, 12H).

For spectroscopic characterization, the absorbance spectra of free NIR dye and NIR-glucosamine were measured using a Shimadzu UV-VIS 1700 spectrophotometer (Columbia, MD) and the emission spectra were measured using a PTI Technologies spectrofluorometer (Oxnard, CA).

Cell Culture

Stable SW480 clones expressing the neomycin selection cassette (SW480*neo*) were isolated and characterized as previously reported (15). SW480*neo* (human colorectal adenocarcinoma) cells were propagated in Dulbecco's Modified Eagle Medium (DMEM; high glucose) supplemented with 2mM L-glutamine, 10% FBS, and 50 mg gentamicin sulfate in vented culture flasks (Corning; Corning, NY) at 37 °C and 5% CO_2. The medium was replaced every three days or as necessary. After attaining confluence, the cells were sub-cultured approximately 1:2 to 1:10.

Animal Models

Animal studies were performed under guidelines approved by the Institutional Animal Care and Use Committee (IACUC) at Vanderbilt University.

SW480*neo* cells were propagated until near confluency as described above. Cells were harvested by incubation with trypsin, pelleted by centrifugation, resuspended in sterile CMF-PBS, counted and assessed for viability (%) using trypan blue staining. The cells were again pelleted by centrifugation, resuspended in sterile CMF-PBS at a concentration of 1.5×10^6 or 2×10^6 cells/100 μL and kept on ice. Prior to cell implantation, the cell-containing tube was gently inverted several times to assure proper cell distribution. Athymic nude (nu/nu) mice were finally injected with approximately 1.5×10^6 or 2×10^6 SW480*neo* cells (100 μL volume) subcutaneously on one or both hind limbs.

In Vivo Optical Imaging Studies

During the imaging sessions, the mice were kept on a heated animal support plate under general anesthesia by inhalation of 2-3% isoflurane. Anesthesia was initiated in an induction chamber.

Tumor-bearing mice that had been fasted overnight to decrease blood glucose levels were retroorbitally injected with 20 nmoles of either free NIR dye or NIR-glucosamine (100 μL in sterile saline). The biodistribution and accumulation of free NIR dye and NIR-glucosamine were monitored in real-time using the IVIS Imaging System 200 (Xenogen Corporation/ Caliper LifeSciences; Alameda, CA) equipped with an indocyanine green (ICG) excitation and emission filter set (710 – 760 nm and 810 – 875 nm, respectively). Images were obtained pre-injection and at numerous time points post-injection (typically several minutes post-injection, 1 hour, 3 hours, 4 hours, 6 hours, 8 hours, 12 hours, 24 hours and 48 hours). The following instrument settings were used: 1

or 3 second exposure time, small or medium binning (4 x 4 pixels or 8 x 8 pixels, respectively), f/stop of 8 and FOV B or C (6.4 cm x 6.4 cm and 12.8 cm x 12.8 cm, respectively). At the conclusion of the study, the mice were sacrificed and the harvested organs (heart, lungs, kidneys, liver) and tumors were also imaged using the same IVIS instrument parameters and/or on the Odyssey Infrared Imaging System. The tumors and organs were subsequently fixed in 10% formalin followed by ethanol dehydration. The fixed tumor tissues were then paraffin embedded and serially sliced. Alternating slices were stained with hematoxylin and eosin (H&E) for histological characterization or DAPI-mounted for NIR fluorescence microscopy.

The data were processed in Living Image® Software Version 2.50 (Xenogen Corporation). Regions of interest (ROIs) were drawn over the xenograft tumors and a normal region. Since most of the mice had two hindlimb tumors, several "normal" ROIs were drawn and evaluated including regions over one forelimb, along the midline (spine) between the two flank tumors, slightly to the right or left of the spine between the two flank tumors, between the forelimbs and below the tumors on the lower portion of a hindlimb. All of the data presented here refer to the lower hindlimb ROI analysis for reasons discussed below. Also, since these mice were imaged longitudinally, the contribution of residual NIR-glucosamine or free NIR dye needed to be accounted for. This was accomplished by subtracting the original (true) pre-injection fluorescence intensity obtained on the very first day of imaging from the initial "pre-injection" fluorescence intensity acquired a week or more later to reestablish baseline pre-injection values. For example: $FI_{6h\ pi,\ day\ B} = FI_{6h\ pi,\ day\ B} - \left(FI_{preinjection, day\ B} - FI_{preinjection, day\ A}\right)$ where FI ≡ fluorescence intensity in terms of average radiance = [p/s/cm^2/sr] and

$\left(FI_{preinjection,day\ B} - FI_{preinjection,day\ A}\right)$ represents the contribution from the residual fluorescence signal.

To generate time activity curves and monitor biodistribution, accumulation and clearance rates, the average radiance (photons/sec/cm^2/sr) ± standard deviation for each group were plotted as a function of time post-injection to generate time-activity curves (n = 2 – 8 tumors from 1 – 4 mice per group). To further determine tumor specificity, the tumor to normal contrast ratio was also calculated as the average ratio of the fluorescence intensity of the tumor region relative to the normal tissue.

In Vivo microPET Imaging

SW480*neo* tumor-bearing mice that had been fasted overnight to decrease blood glucose levels were injected with approximately 118-300 μCi of ^{18}FDG two days pre- or post-injection of NIR-glucosamine and imaged dynamically over an hour to an hour and a half using the Concorde Microsystems microPET Focus 220 (Concorde Microsystems; Knoxville, TN). Maximum a posteriori (MAP) reconstructions were performed after the scans were collected. Data processing was performed using ASIPro VM^{TM} (Concorde Microsystems; Knoxville, TN).

Blood Stability

HPLC was used to evaluate the stability of NIR-glucosamine in blood. Since blood samples taken from mice ~3.5 hours post-injection of NIR-glucosamine did not contain enough compound to analyze via HPLC or mass spectrometry, these studies were performed *ex vivo*. To maintain the *in vivo* concentration (20 nmoles injected into ~1.6

mL of blood), five nmoles of NIR-glucosamine was added to 400 µL of blood obtained from Balb/c mice; the blood was originally collected and stored in heparinized-tubes. The NIR-glucosamine-containing blood was then incubated at 37°C for either zero, four or eight hours to allow sufficient time for agent degradation by blood components. The NIR-glucosamine-containing blood was then centrifuged at 1,800 g for 20 minutes to separate the red blood cells from the plasma. The supernatant (plasma) was collected, vortexed, and centrifuged again for 20 minutes at 1,800 g to settle any sediment. The supernatant was carefully transferred to another tube and an equal volume of acetonitrile was added for precipitation. The tube was vortexed for 60 seconds and centrifuged for five minutes at 1,800 g. Supernatant was transferred to a separate tube and centrifuged again at 1,800 g for five minutes to remove any residual precipitate.

Stock NIR-glucosamine and free NIR dye as well as the purified plasma samples were analyzed via HPLC at 782 nm. Flow A was 20mM tetrabutylammonium bromide in water and B was 20mM tetrabutylammonium bromide in 90% acetonitrile and 10% water. The elution method started with a linear gradient from 100% to 50% A over 10 minutes, held at 50% for 5 minutes, arrived at 10% A in another 10 minutes, held at 10% A for 5 minutes and finally returned to 100% A over 1 minute. The data were processed by integrating the area under the peaks at 782 nm using Empower software (Waters Corporation; Milford, MA). The relative percent free NIR dye (eluting at 23 minutes) and NIR-glucosamine (eluting at 18 minutes) were calculated as:

$$\%\ \text{Free NIR Dye} = \frac{\text{Area at 23 minutes}}{\text{Area at 18 min} + \text{Area at 23 min}} \text{ x } 100$$

$$\%\ \text{NIR - glucosamine} = \frac{\text{Area at 18 minutes}}{\text{Area at 18 min} + \text{Area at 23 min}} \text{ x } 100$$

Preliminary Extravasation Experiment

Non-tumor-bearing mice were injected with either free NIR dye (20 nmoles), NIR-glucosamine (20 nmoles) or saline (2 mice per compound). At approximately three and a half hours post-injection, one group of mice was exsanguinated while the other group was not. The brain, liver, kidneys, lungs and heart were harvested and imaged on the Odyssey Infrared Imaging System on both the 700 and 800 nm channels ($\lambda_{ex,\ 700}$ = 680 nm and $\lambda_{ex,\ 800}$ = 780 nm; dichroic mirror reflects light below 750 nm for detection in the 700 channel and transmits light above 810 nm for detection in the 800 nm channel).

In Vitro Uptake and Competition Studies

SW480*neo* cells were plated at ~15,000 cells per well in 96 MicroWell™ Nunclon™Δ Optical Bottom Plates (Nalge Nunc International; Rochester, NY) and incubated under standard culture conditions for approximately 48 hours. Immediately prior to experimentation, the cells were washed once with warmed glucose- and FBS-free medium to remove any dead cells, glucose and serum. Twelve populations of SW480*neo* cells [1 through 12] were evaluated in triplicate using glucose- and FBS-free medium: cells incubated with 1 μM or 10 μM NIR-glucosamine [1,2] or free NIR dye [3,4] for 30 minutes in the absence of inhibitor; cells pretreated with 50 mM D-glucose for 30 minutes followed by incubation with 1 μM or 10 μM NIR-glucosamine [5,6] or free NIR dye [7,8] for 30 minutes; cells pretreated with 10 μM cytochalasin B for 30 minutes followed by a 30-minute incubation with 1 μM or 10 μM NIR-glucosamine [9,10] or free NIR dye [11,12]. Following a 30-minute incubation, the cells were gently washed three times with glucose- and FBS-free medium and imaged on the Odyssey Infrared Imaging

System (LI-COR Biosciences; Lincoln, NE) at 169 μm resolution, 3 mm focus offset, and 7.0 intensity in the 800 nm channel. The average raw fluorescence intensity of each population ± standard deviation was then plotted; n = 3.

Cell Imaging

SW480*neo* cells (~75,000 per dish) were plated in collagen-coated glass bottom dishes (MatTek Corporation; Ashland, MA) 48 hours prior to experimentation. The cells were first washed once with warmed glucose- and FBS-free medium and then incubated with 10 – 20 μM NIR-glucosamine or free NIR dye for 30 minutes at 37°C. Subsequently, the cells were washed three times with medium and imaged. A Nikon Eclipse TE2000-U fluorescence microscope equipped with a mercury lamp, indocyanine green (ICG) filter set and a Hamamatsu ORCA II BT 512 camera controlled by Metamorph software v6.1 (Molecular Devices Corporation; Downingtown, PA) was used for imaging.

Statistical Analysis

Statistical significance was determined using a one-way or two-way analysis of variance (ANOVA) test and the Holm-Sidak method for pairwise multiple comparisons with an overall significance level of 0.05 (SigmaStat v3.10).

Results and Discussion

Based on literature precedence regarding optical analogues to ^{18}FDG, our laboratory synthesized an alternative NIR D-glucose analogue by coupling the IRDye^{TM}

800CW NHS ester dye to D-glucosamine (NIR-glucosamine; Figure 5.1A). The IRDye^{TM} 800CW is reported by the manufacturer to be a cyanine-like dye (Figure 5.1B) that is highly water soluble and relatively stable. IRDye^{TM} 800CW capitalizes on the increased photon penetration in the NIR tissue transparency window and is slightly red-shifted relative to Cy5.5. This red-shift in excitation and emission eliminates the fluorescence contribution from the autofluorescence of typical alfalfa-based rodent chow, which is often seen in the Cy5.5 wavelength region, and its longer wavelength excitation and emission is more suitable for *in vivo* imaging (14). In water, NIR-glucosamine exhibits an absorbance maximum centered at 774 nm with peak emission at 799 nm (λ_{ex} = 774 nm; Figure 5.1D). This spectroscopy is very similar to the IRDye800-acid (designated here as “free NIR dye”; λ_{ex} = 774 nm, λ_{ex} = 796 nm). Like ^{18}FDG (Figure 5.1C), NIR-glucosamine is conjugated at the C-2 position to allow for potential

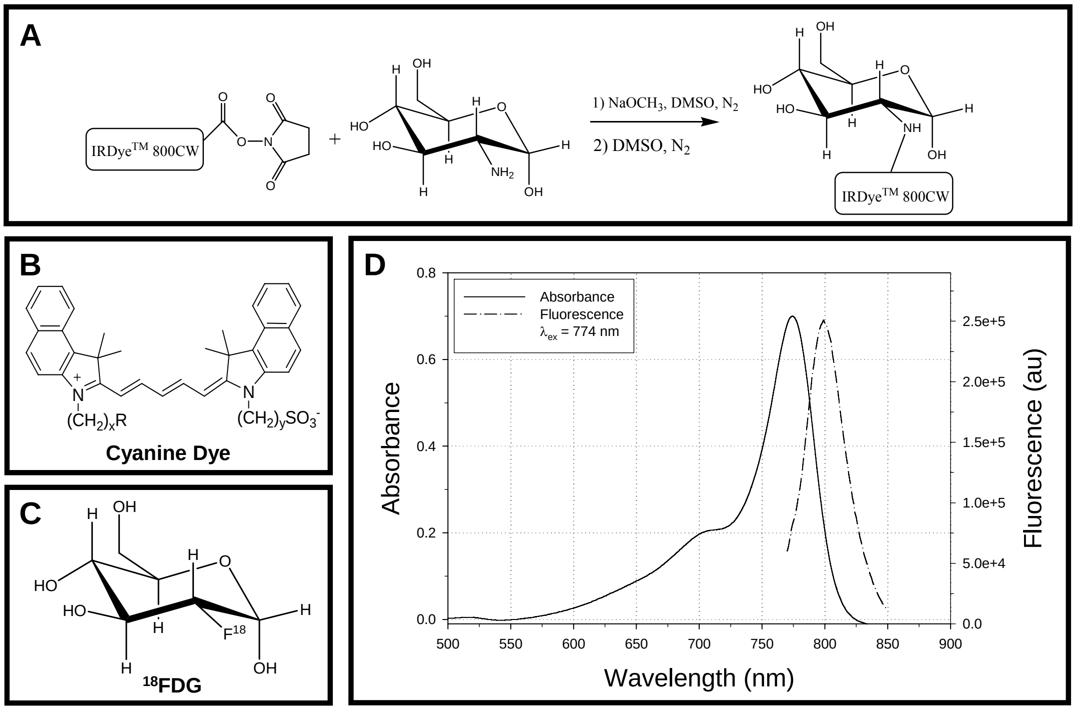

Figure 5.1: (A) Synthetic pathway, (B) relevant chemical structures, and (C) aqueous spectroscopic properties of NIR-glucosamine (λ_{ex} = 774 nm).

recognition and phosphorylation by hexokinase at C-6.

In a preliminary study of the *in vivo* tumor targeting capabilities of NIR-glucosamine, an SW480*neo* tumor-bearing mouse was injected with 20 nmoles of NIR-glucosamine and imaged over time using the IVIS Imaging System 200. Fluorescence images taken pre-injection as well as approximately three minutes and six hours post-injection of NIR-glucosamine are shown in Figure 5.2; the fluorescence images are also overlaid onto the corresponding photographic images for orientation. Prior to injection, the mice are essentially devoid of NIR fluorescence, revealing the negligible autofluorescence of tissue in the exploited wavelength region. Approximately 3 minutes post-injection, the NIR-glucosamine appears to be fairly uniformly distributed throughout the mouse with some increased signal near the retroorbital injection site (right eye).

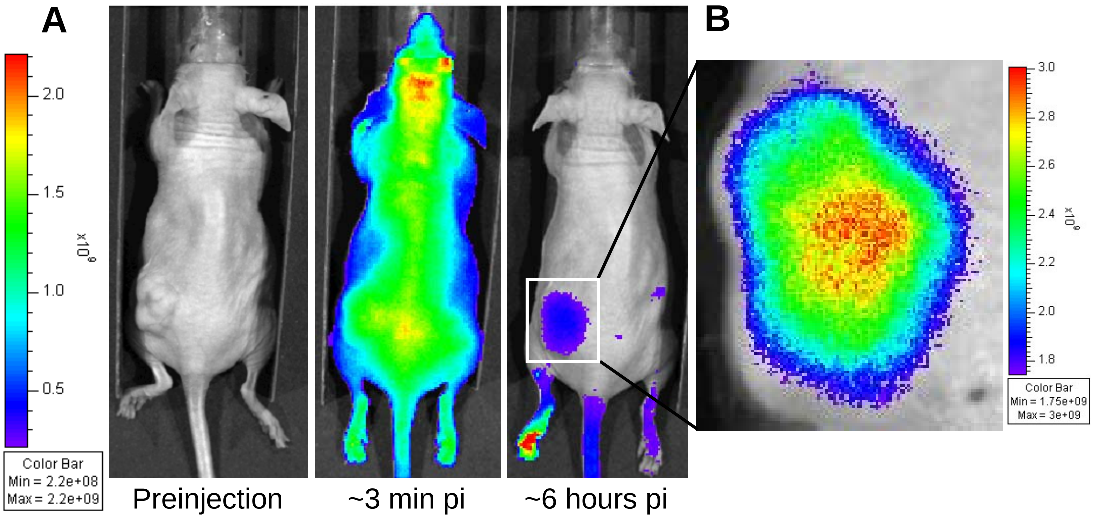

Figure 5.2. Biodistribution and accumulation of NIR-glucosamine in real-time. (A) Fluorescence images of an SW480 tumor-bearing mouse overlaid onto the corresponding photographic images, displayed on a color bar scale ranging from $2.2x10^8$ to $2.2x10^9$ photons/sec/cm^2/sr (acquired using FOV C and medium binning). Substantial accumulation of NIR-glucosamine is seen in the tumor region relative to the normal tissues approximately six hours post-injection. (B) Zoomed image of the tumor region with better resolution on a color bar scale ranging from $1.75x10^9$ to $3x10^9$ photons/sec/cm^2/sr (acquired using FOV B and small binning).

However, almost six hours post-injection, substantial accumulation of NIR-glucosamine is apparent in the tumor tissue. The bright fluorescence signal on the left rear paw is believed to result from urine contamination and is not present in other imaging studies. Figure 5.2B displays a zoomed image of the tumor region, imaged using a smaller IVIS field of view (FOV B = 6.4 x 6.4 cm), with better resolution (binning = 4 x 4), and presented on a different average radiance scale. Quantification of the fluorescent signal in the tumor region relative to the normal tissue on the opposite hindlimb demonstrates a 2.3-fold tumor-specific enhancement, suggesting that NIR-glucosamine specifically labels tumor tissue *in vivo*.

Two days after optical imaging, the mouse shown in Figure 5.2 was injected with 118 μCi of ^{18}FDG and dynamically imaged in the Concorde MicroSystems microPET scanner. A summation of the microPET images taken over an hour and ten minutes post-injection of ^{18}FDG is shown in Figure 5.3A. As expected, enhanced PET signal resulting from increased uptake and accumulation of ^{18}FDG is seen in the highly metabolic tissues including the brain, heart, and tumor. The bladder is also significantly bright due to the renal excretion of ^{18}FDG. For comparison, the optical image demonstrating NIR-glucosamine accumulation six hours post-injection is shown in Figure 5.3B. We originally attributed the lack of fluorescence signal emanating from the heart and brain following injection with NIR-glucosamine to decreased sensitivity in deeper tissues and the potential that NIR-glucosamine may not cross the blood brain barrier. Further studies have demonstrated otherwise as discussed below.

Figure 5.3C displays a coronal slice through the tumor of the ^{18}FDG-PET image for comparison to the tumor-specific accumulation of NIR-glucosamine (Figure 5.3D). It

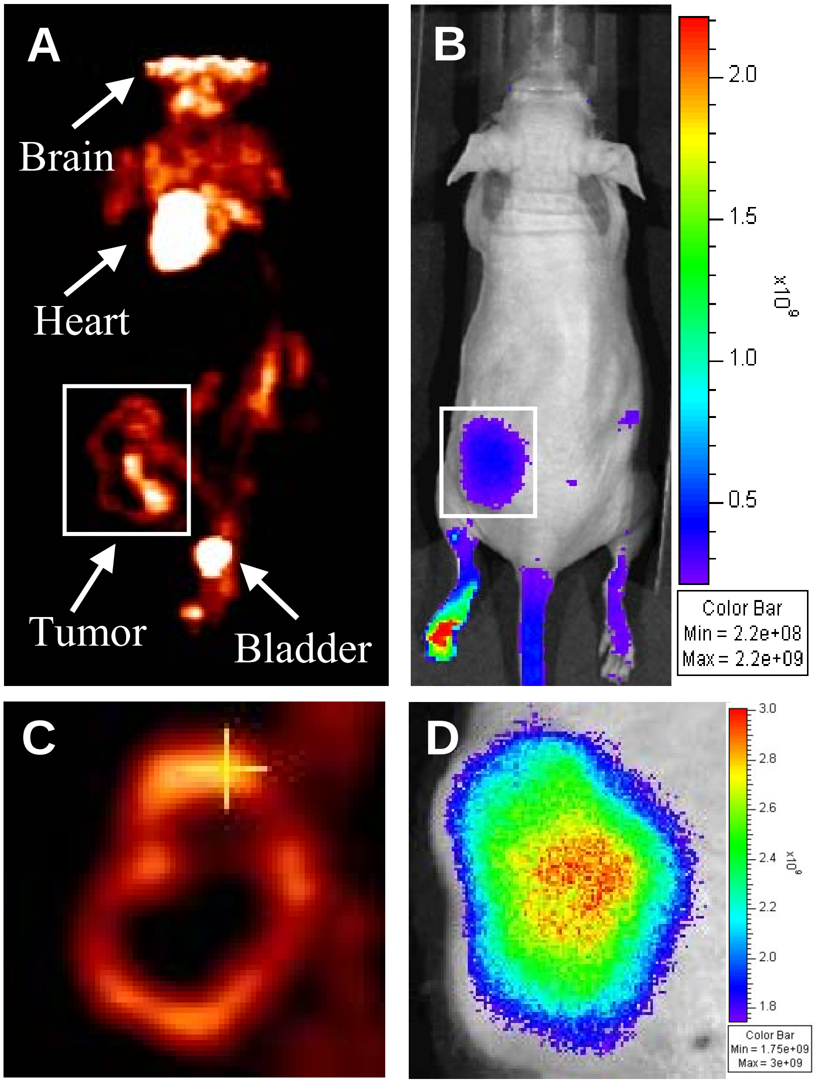

^{18}FDG-PET Image of the Tumor Region: Coronal Slice

Optical Image of NIR-glucosamine Accumulation

Figure 5.3. Comparison of ^{18}FDG signal to NIR-glucosamine accumulation in the tumor region of the same SW480 tumor-bearing mouse. (A) The microPET image illustrates ^{18}FDG accumulation in the highly metabolic tissues (brain, heart, and tumor) as well as the bladder due to renal excretion of ^{18}FDG. (B) The optical image captured six hours post-injection shows substantial accumulation of NIR-glucosamine in the same tumor two days prior to ^{18}FDG-microPET imaging. (C) A coronal slice through the tumor of the ^{18}FDG-PET image for comparison to the tumor-specific accumulation of NIR-glucosamine (D).

is noteworthy that both images have a similar size and shape, indicating potential correlation between the two imaging probes and methodologies. However, the central region of the tumor is devoid of ^{18}FDG-PET signal while the optical image shows substantial fluorescence intensity mid-tumor. This observation is presumably due to the fact that the IVIS Imaging System produces two-dimensional projection images of fluorescence intensity and is essentially a volumetric ensemble of all the photons emanating from the interrogated regions, whereas the microPET image is a slice through the tumor itself. This discrepancy is analogous to the difference between fluorescence and confocal microscopy. It is likely that the dark region on the ^{18}FDG-microPET image represented necrotic tissue that was not evident in the 2D optical projection image. (In later studies, it became apparent that unlike ^{18}FDG, NIR-glucosamine does label necrotic and transitioning tissues, which may also account for the difference.) Qualitatively, but not quantitatively, the tumor-specific uptake of NIR-glucosamine appears to mimic that of ^{18}FDG uptake and accumulation. We therefore set out to determine the uptake mechanism responsible for tumor-specific labeling by NIR-glucosamine and to compare the *in vivo* biodistribution, clearance and accumulation of NIR-glucosamine with free NIR dye.

To evaluate the *in vivo* biodistribution, clearance and accumulation of NIR-glucosamine compared to free NIR dye, a pilot imaging study was performed in four SW480*neo* tumor-bearing mice. Approximately four and a half weeks post-implantation, the tumors were externally visible but fairly small (2 – 8 mm in their longest dimension). Following an overnight fast, the tumor-bearing mice were retroorbitally injected with 20 nmoles of free NIR dye and imaged over 24 hours using the Xenogen IVIS Imaging

System 200. Two days later, the same mice were injected with NIR-glucosamine and again monitored over 24 hours post-injection. The fluorescence intensity of the tumor and normal regions were subsequently quantified in terms of average radiance (photons/sec/cm^2/steradian) to generate time activity curves and determine tumor specificity. It is important to note that since these mice each had two flank tumors, the opposite hindlimb could not be used as the "normal" tissue control. Thus, several ROIs were evaluated to determine the most appropriate "normal" tissue region, including regions (1) over one forelimb, (2) along the midline (spine) between the two flank tumors, (3) slightly to the right or left of the spine between the two flank tumors, (4) between the forelimbs and (5) below the tumors on the lower portion of a hindlimb. The "normal" region defined over one forelimb consistently provided the highest tumor to normal contrast. However, this region did not appear to accurately represent normal tissue biodistribution as evident even in the immediately post-injection images (ex. Figure 5.2A). The "normal" regions defined along the spine and slightly offset from the spine demonstrated increased fluorescence intensity relative to the rest of the normal tissue, even immediately post-injection. These ROIs were also too close to the bladder and presumably included some signal from the renally cleared agents. Finally, the "normal" ROI between the shoulders consistently demonstrated a different clearance profile than either the tumor or the other normal ROIs and was consequently eliminated. Thus, all of the results presented herein result from quantitative analysis of the tumor ROI relative to the lower portion of the hindlimb.

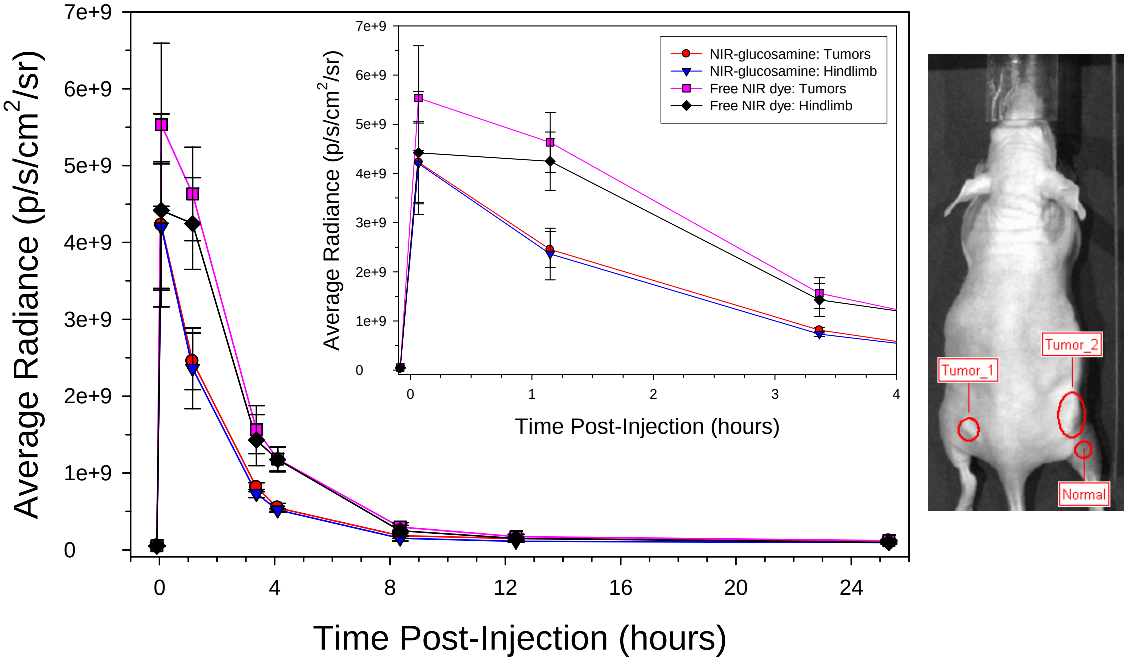

Figure 5.4. Time activity curves for NIR-glucosamine and free NIR dye in the tumor region and "normal" lower hindlimb tissue of mice bearing relatively small SW480 xenograft tumors. The same average radiance data up to four hours post-injection is displayed in the inset plot. The NIR-glucosamine appears to clear slightly faster than the free NIR dye in both the tumor and normal regions.

The *in vivo* time activity curves of NIR-glucosamine and free NIR dye in mice bearing relatively small SW480*neo* tumors are shown in Figure 5.4; the same average radiance data up to four hours post-injection is displayed as an inset. The NIR-glucosamine and free NIR dye appear to clear from the tumor and normal tissues with slightly different clearance profiles. More specifically, the time necessary to clear half of the maximum fluorescence intensity occurring immediately post-injection is approximately 2.5 hours for the free NIR dye, but only ~ 1.5 hours for the NIR-glucosamine. The faster rate of clearance presumably results from the increased polarity and therefore water solubility of NIR-glucosamine relative to the free NIR dye, which is more lipophilic. Overall, both agents appear to provide very little to no contrast

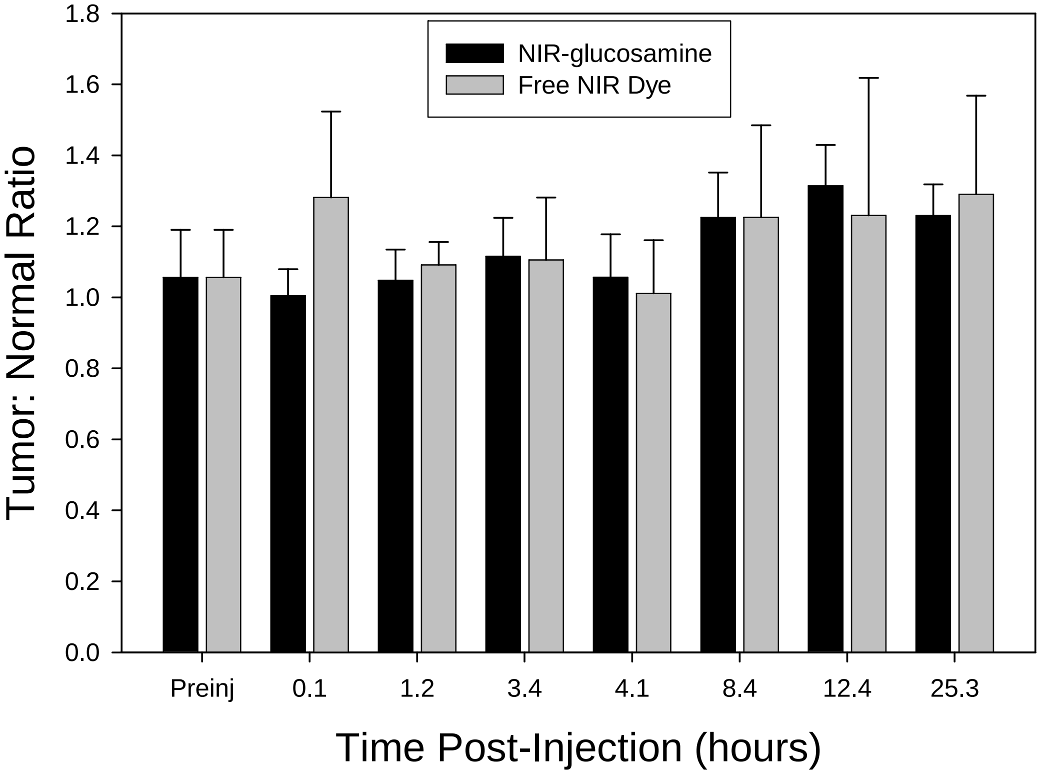

Figure 5.5. The tumor to normal contrast ratios of mice bearing relatively small SW480 xenograft tumors at each time point post-injection. Overall, both agents appear to provide very little to no tumor-specific contrast enhancement, suggesting a potential size or vascularity requirement for substantial tumor uptake.

enhancement in the relatively small tumors (Figure 5.5), suggesting a potential size or vascularity requirement for substantial tumor uptake.

Several weeks later, when the tumors approximately doubled in size, both the free NIR dye and NIR-glucosamine provided enhanced tumor-specific contrast relative to the adjacent normal hindlimb tissue. The time activity curves and tumor to normal contrast ratios for two mice imaged simultaneously following retroorbital injection of 20 nmoles of free NIR dye or NIR-glucosamine are shown in Figures 5.6 and 5.7, respectively. As previously demonstrated in Figure 5.4, the NIR-glucosamine appears to clear more rapidly than the free NIR dye, particularly from the normal hindlimb tissue (Figure 5.6

inset). As a result, the apparent tumor to normal contrast from NIR-glucosamine increases from 1.0 immediately post-injection to a maximum of 2.7 six hours post-injection (Figure 5.7). This 2.7-fold contrast enhancement persists for the duration of the study (~24 hours). Conversely, the tumor to normal ratio from the free NIR dye is only 1.8 at six hours post-injection, but steadily increases to 3.3-fold at 21 hours post-injection. Since the fluorescence intensity in the free NIR dye-containing tumors is consistently higher than the fluorescence intensity in the NIR-glucosamine-containing tumors, this contrast discrepancy is presumably due to the faster normal tissue washout of NIR-glucosamine rather than preferential NIR-glucosamine accumulation over free NIR dye. This increased normal tissue clearance due to the contribution of the D-glucosamine may prove beneficial over free NIR dye due to the earlier contrast enhancement and could

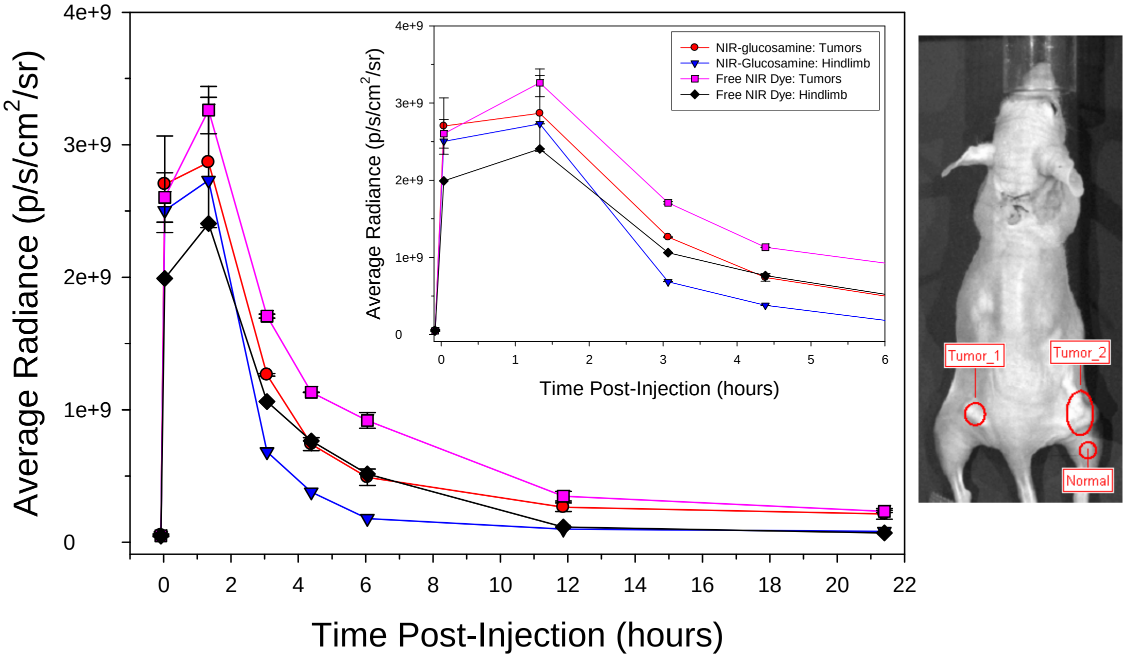

Figure 5.6. Time activity curves for NIR-glucosamine and free NIR dye in the tumor region and "normal" lower hindlimb tissue of mice bearing relatively larger SW480 xenograft tumors. The same average radiance data up to six hours post-injection is displayed in the inset plot. The NIR-glucosamine appears to clear slightly faster than the free NIR dye in the normal hindlimb region.

potentially provide a reduction in cytotoxicity. However, more animal studies are necessary to evaluate the potential advantages of NIR-glucosamine over the use of free NIR dye for tumor labeling.

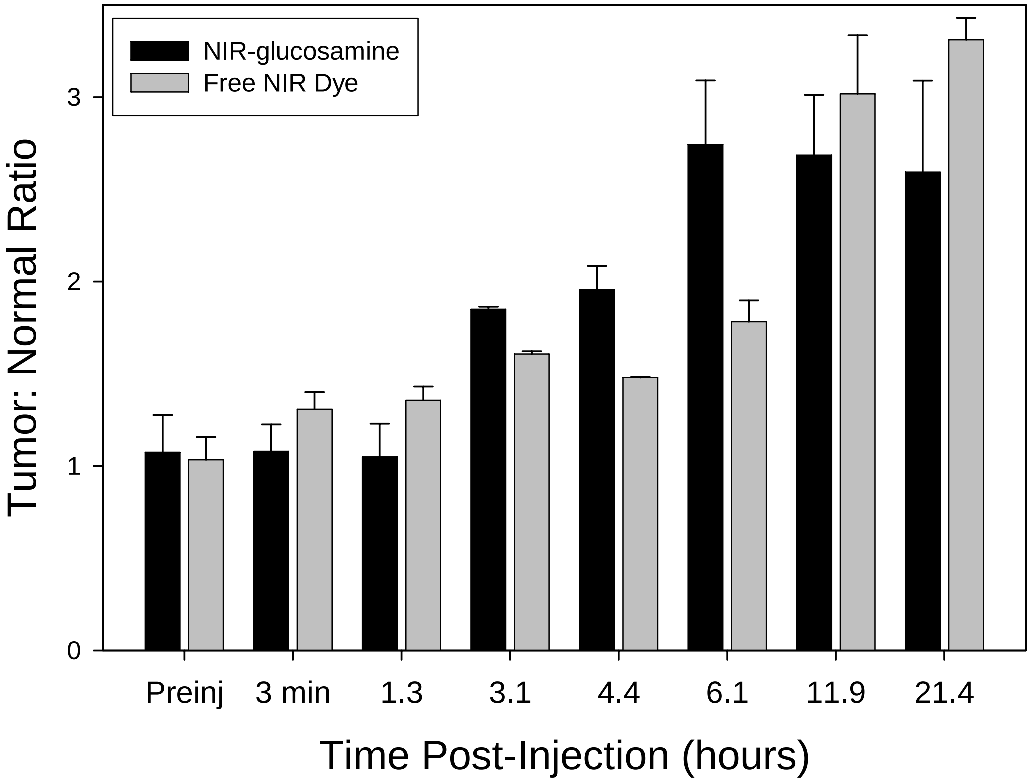

Figure 5.7. The tumor to normal contrast ratios of mice bearing relatively larger SW480 xenograft tumors at each time point post-injection. The NIR-glucosamine reaches a maximum tumor to normal contrast ratio (2.7) at six hours post-injection, while the free NIR dye contrast steadily rises to 3.3 over 24 hours post-injection. This discrepancy is presumably due to the faster rate of NIR-glucosamine clearance in the normal hindlimb tissue, which appears to result in earlier tumor-specific contrast and potentially less toxicity.

The *ex vivo* NIR fluorescence and histological characterization of tumor tissue harvested approximately 24 hours post-injection of NIR-glucosamine or free NIR dye is shown in Figure 5.8. Serial sections of tumor tissue were either DAPI-mounted for NIR fluorescence microscopy (A-C, E-G) or stained with hematoxylin and eosin (H&E) for histological characterization (D,H). Both NIR-glucosamine and free NIR dye appear to predominantly label necrotic or transitioning tissue rather than viable tumor cells, suggesting non-specific pooling of these agents *in vivo* due to the enhanced permeability and retention (EPR) effect in malignant tumors (16).

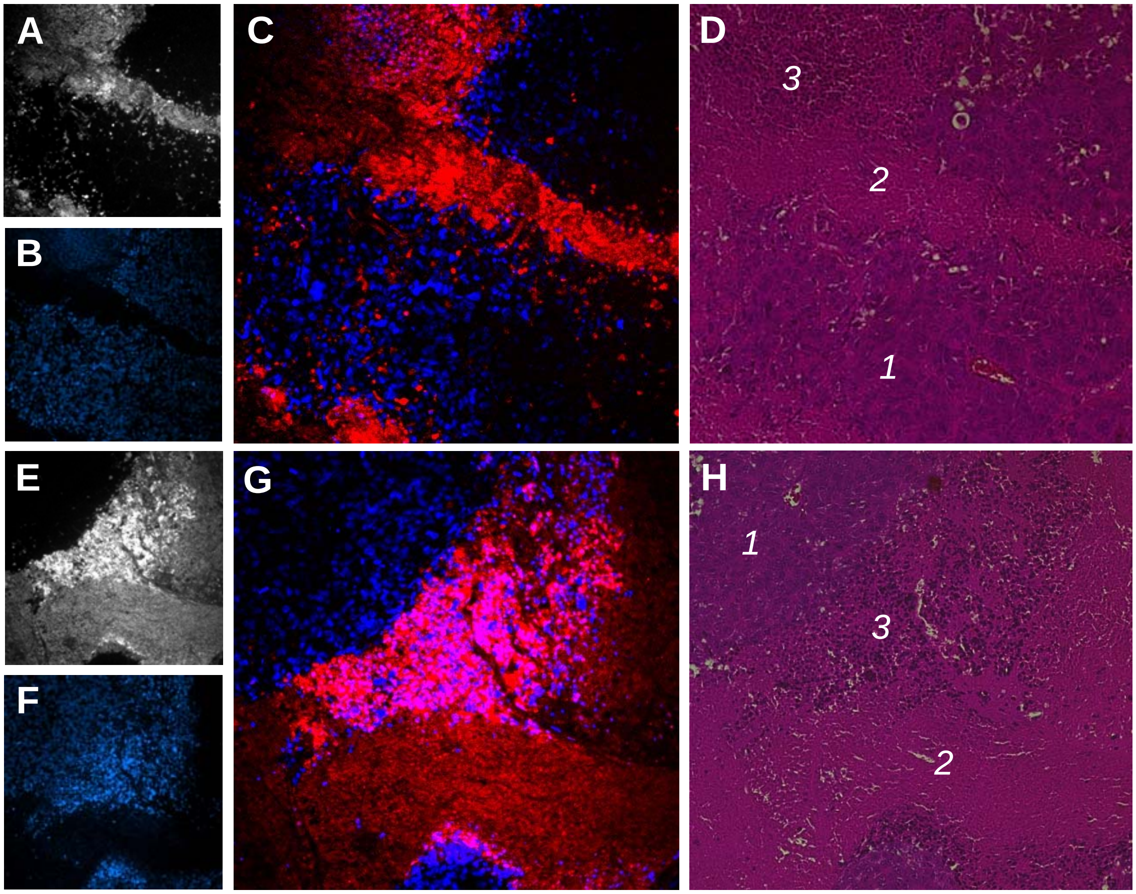

Figure 5.8. ***Ex vivo*** **NIR fluorescence and histological characterization of tumor tissue harvested from SW480 tumor-bearing mice ~24 hours post-injection of NIR-glucosamine (A-D) or free NIR dye (E-H).** (A, B) NIR fluorescence and DAPI images from the same slice of a NIR-glucosamine-containing tumor section. (C) Overlay of the fluorescence and DAPI images seen in A and B. (D) H&E stain from an adjacent tissue section that shows (1) viable tumor, (2) necrotic, and (3) transitioning tumor tissue. (E, F) NIR fluorescence and DAPI images from the same slice of a free NIR dye-containing tumor section. (G) Overlay of the fluorescence and DAPI images seen in E and F. (H) H&E stain from an adjacent tissue section that shows (1) viable tumor, (2) necrotic, and (3) transitioning tumor tissue.

Since both NIR-glucosamine and free NIR dye provide similar contrast enhancement in SW480*neo* tumor-bearing mice, the blood stability and extravasation of these molecules came into question. HPLC analysis was used to determine whether or not NIR-glucosamine is degraded to free NIR dye in the presence of blood components on a relevant time scale. Following a 0, 4, or 8 hour incubation in whole blood, the elution profile of NIR-glucosamine was compared to that of the NIR-glucosamine and free NIR dye stocks at 782 nm (Table 5.1). NIR-glucosamine and free NIR dye eluted at ~18.1 minutes and ~22.5 minutes, respectively. The shorter elution time for NIR-glucosamine indicates an increased polarity relative to the free NIR dye, as previously discussed. The reduction in area following incubation in whole blood results from some baseline issues due to the very low signal of these samples. The blood stability analysis will be scaled up to allow for sample concentration and improved signal to noise. The small fraction of the NIR-glucosamine stock (~8 %) that eluted at 22.6 minutes is likely free NIR dye. The NIR-glucosamine sample used for these studies was approximately six month old and has probably degraded slightly. However, this small contribution to the entire elution profile remains less than 13 % after exposure to whole blood components for 4 or 8 hours. This suggests that the NIR-glucosamine remains intact and is stable in blood for at least 8 hours.

Table 5.1. Blood Stability Analysis.

Compound	Experimental Condition	Peak Elution Time (min) NIR-gluc	Area	Peak Elution Time (min) Free NIR dye	Area	% NIR-glucosamine[a]	% Free NIR Dye[b]
Free NIR Dye	Stock Solution	18.3	1.3	22.5	95	1 %	99 %
NIR-glucosamine	Stock Solution	18.1	88	22.6	7.7	92 %	8 %
NIR-glucosamine	Diluted in blood and immediately purified	18.0	66	22.5	6.9	91 %	9 %
NIR-glucosamine	In whole blood for 4 hours	18.2	53	23.1	7.1	88 %	12 %
NIR-glucosamine	In whole blood for 8 hours	18.1	61	23.0	4.7	93 %	7 %

$$^{a}\ \%\ \text{Free NIR Dye} = \frac{\text{Area at 23 minutes}}{\text{Area at 18 min} + \text{Area at 23 min}} \times 100; \qquad ^{b}\ \%\ \text{NIR - glucosamine} = \frac{\text{Area at 18 minutes}}{\text{Area at 18 min} + \text{Area at 23 min}} \times 100$$

Next, a preliminary experiment was performed to determine whether or not these compounds extravasate into various tissues or are unable to escape the vasculature in the absence of the enhanced permeability and retention (EPR) effect in tumors (16). Non-tumor-bearing mice were injected with either free NIR dye, NIR-glucosamine or saline (2 mice per compound). At approximately three and a half hours post-injection, one group of mice was exsanguinated while the other group was not. Various organs were subsequently harvested (brain, liver, kidneys, lungs, heart) and imaged on the Odyssey Infrared Imaging System on both the 700 and 800 nm channels. The 700 nm channel allows for visualization of the organs due to autofluorescence in this wavelength range,

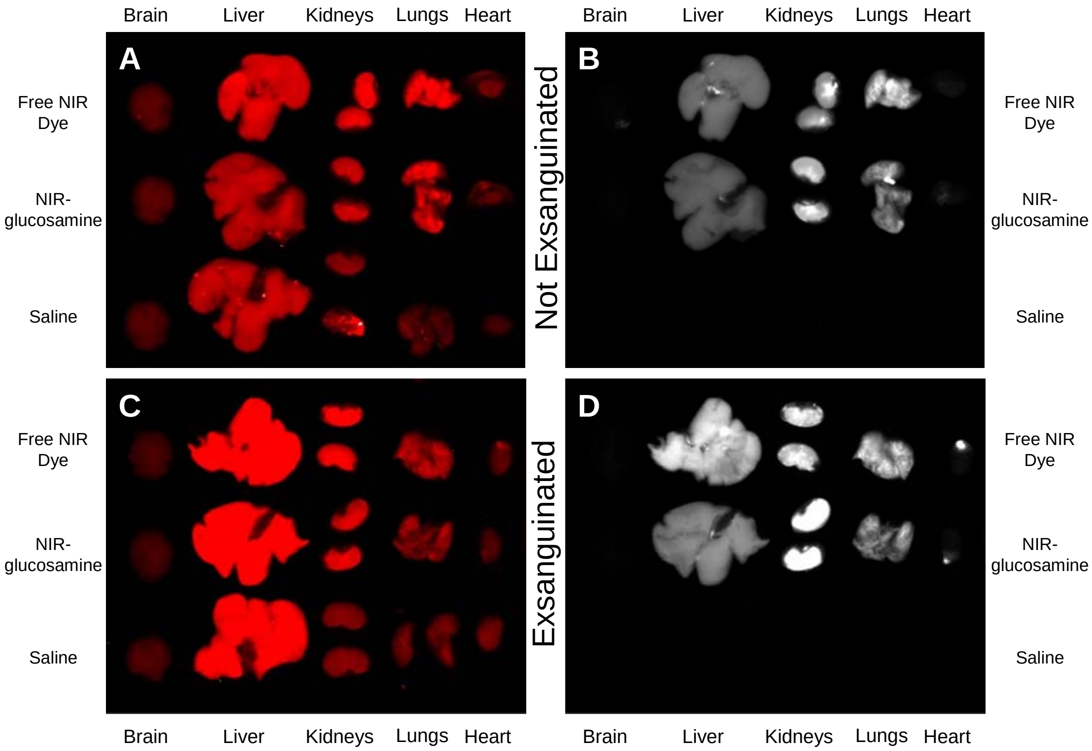

Figure 5.9. Fluorescence images of tissues harvested from mice ~3.5 hours post-injection of free NIR dye, NIR-glucosamine or saline using the 700 nm (A, C) and 800 nm (B, D) channels of the Odyssey Infrared Imaging System, displayed on the same dynamic range. (A, B) Mice that have not been exsanguinated. (C, D) Exsanguinated mice.

while the 800 nm channel only collects NIR signal through an 810 nm longpass emission filter. Two important observations can be made from the results in Figure 5.9. First, the NIR-glucosamine agent does not appear to be taken up and accumulated in the highly metabolically active brain or heart; the bright, localized NIR fluorescence that does appear to emanate from the heart is actually from a fatty deposit attached to the heart itself. It is possible that NIR-glucosamine does not cross the intact blood brain barrier, but one would expect to see fluorescence signal in the heart if NIR-glucosamine functioned as an optical analogue to ^{18}FDG. Secondly, the fluorescence signal in the exsanguinated organs is at least as bright, if not brighter than the organs from the non-exsanguinated mice. The slight increase in signal in the exsanguinated organs may result from the decreased blood volume and therefore reduced hemoglobin absorption of photons, albeit small, or more likely from reduced scattering. The similar NIR intensities suggest that withdrawal of the blood volume did not reduce the fluorescence signal of these organs and that perhaps these agents did extravasate from the vasculature. However, more in depth studies are necessary to fully characterize the distribution of these agents in tissues.

In an attempt to elucidate the cellular uptake mechanism of NIR-glucosamine, *in vitro* competition assays were performed in a multiwell plate format. SW480*neo* cells were incubated with 1 μM or 10 μM NIR-glucosamine or free NIR dye for 30 minutes in the absence of competitor (unblocked) or following pretreatment with 50 mM D-glucose or 10 μM cytochalasin B, two known inhibitors of GLUT-mediated uptake (17). The average raw fluorescence intensity of each population ± the standard deviation is shown in Figure 5.10.

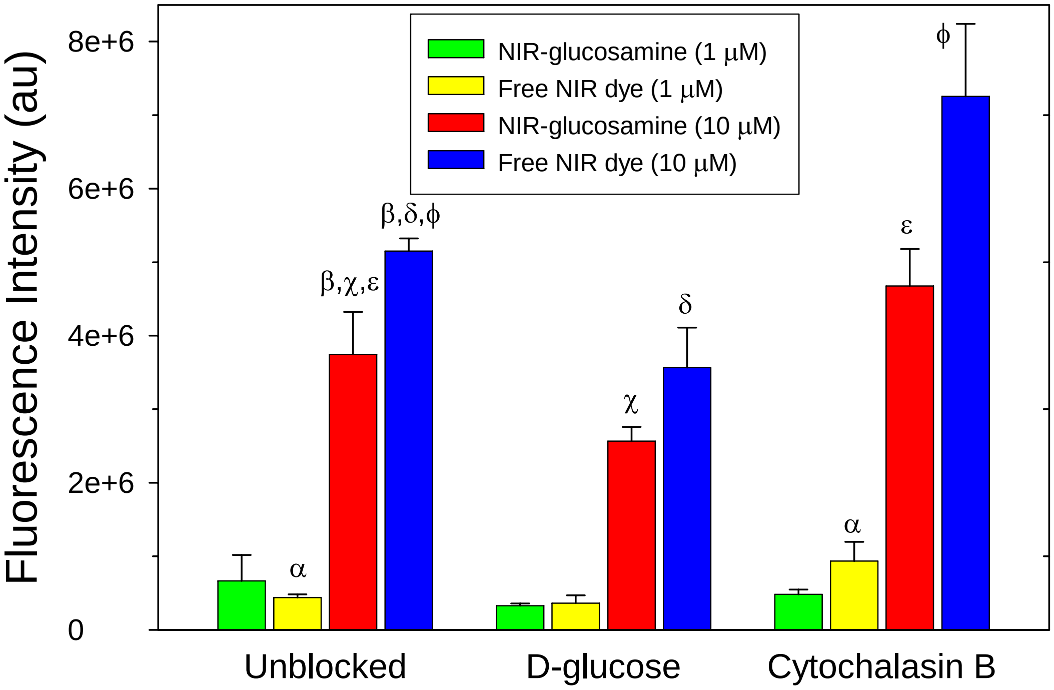

Figure 5.10. ***In vitro* cellular uptake and competition assays performed in a multi-well plate format.** SW480 cells were incubated with 1 µM or 10 µM NIR-glucosamine or free NIR dye in the absence of competitor (unblocked) or following pretreatment with 50 mM D-glucose or 10 µM cytochalasin B. The average raw fluorescence intensity of each population ± the standard deviation is shown here (n = 3 wells). Pairwise statistical significance ($p < 0.05$) is indicated by α, β, χ, δ, ε, ϕ.

At 1 µM NIR-glucosamine (Figure 5.10, green) and free NIR dye (Figure 5.10, yellow) concentrations, the unblocked NIR-glucosamine signal is statistically insignificant from the unblocked free NIR dye population; both agents appear to label SW480*neo* cells equally. In addition, pretreatment with 50 mM D-glucose does not appear to have an affect on either NIR-glucosamine or free NIR dye uptake when dosed at 1 µM concentration. However, cytochalasin B appears to slightly increase the uptake of free NIR dye at 1 µM incubation concentration ($p < 0.05$). The competition assay was also performed using 10 µM NIR-glucosamine (Figure 5.10, red) and free NIR dye (Figure 5.10, blue). Interestingly, the unblocked cells incubated with 10 µM free NIR dye (blue) are significantly more fluorescent than the unblocked cells incubated with 10 μM NIR-glucosamine (red; $p < 0.05$). In addition, pretreatment with 50 mM D-glucose significantly attenuates the fluorescence intensity of both the NIR-glucosamine (red) and free NIR dye (blue) populations relative to the unblocked cells incubated with 10 μM NIR-glucosamine or free NIR dye alone ($p < 0.05$). Finally, pretreatment with 10 μM cytochalasin B does not inhibit cellular uptake, but actually significantly increases the fluorescence intensity of cells incubated with 10 μM NIR-glucosamine or free NIR dye ($p < 0.05$). Taken together, these results suggest that the uptake of NIR-glucosamine is likely not mediated by the GLUT proteins and may simply result from non-specific binding to the cell membrane. If so, the increased fluorescence intensity of the cells incubated with free NIR dye (10 μM) compared to the cells incubated with NIR-glucosamine (10 μM) could be explained by the relative lipophilicity of these molecules. HPLC analysis indicates that the free NIR dye is less polar and thus more lipophilic than the NIR-glucosamine agent (discussed below). This increase in lipophilicity could potentially increase the cell membrane interactions and result in increased cellular-associated fluorescence signal. However, additional studies are necessary to confirm the potential non-specific binding to the lipid membrane or to determine the precise uptake mechanism.

Finally, fluorescence microscopy studies were performed to assess the cellular localization of NIR-glucosamine and free NIR dye. Figure 5.11 displays one slice of a pseudo-confocal NIR z-stack of SW480*neo* cells incubated with NIR-glucosamine (A, B) or free NIR dye (C,D) for 30 minutes. Both agents appear to be primarily localized to the outer cellular membrane. This localization is better demonstrated by the full z-stack, which shows localized fluorescence at the top of the cell that spreads radially outwards as one traverses through the cell. These fluorescence images further suggest non-specific binding to the lipid membrane.

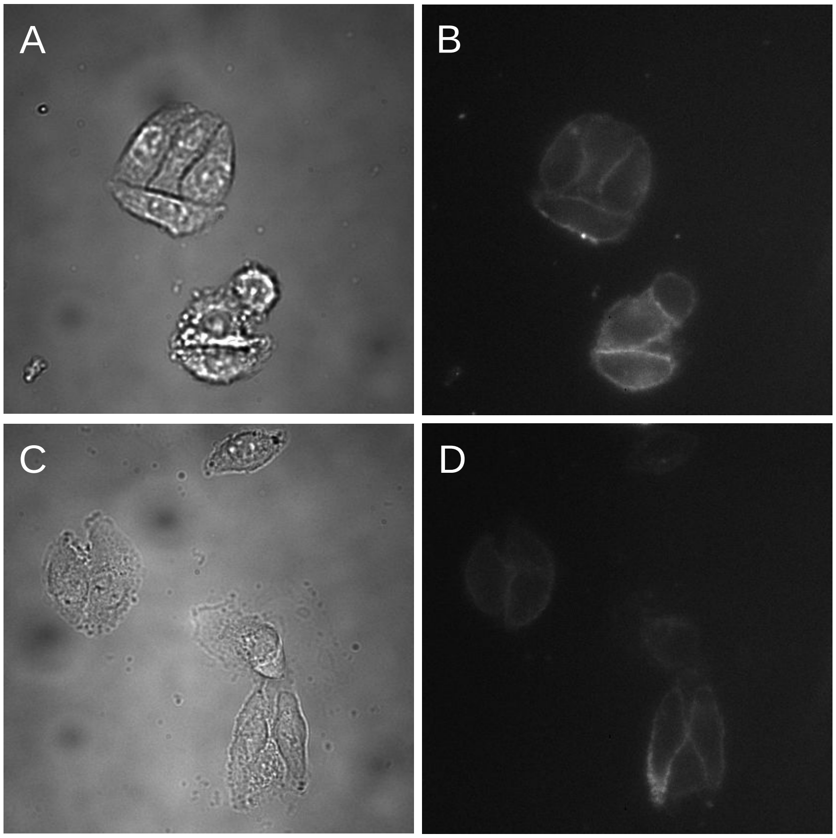

Figure 5.11. Fluorescence microscopy of SW480 cells incubated with NIR-glucosamine (white light image in A and NIR fluorescence in B) or free NIR dye (white light image in C and NIR fluorescence in D) in glucose- and FBS-free medium. The fluorescence signal appears to be primarily associated with the cell membrane. The localization is better demonstrated by the full, pseudo-confocal z-stack.

In summary, this report describes the *in vitro* and *in vivo* characterization of an alternative NIR D-glucose analogue developed in our laboratory. Preliminary imaging studies in an SW480*neo* mouse model of human colon cancer suggest that NIR-glucosamine specifically labels tumor tissue *in vivo* with a 2.3 to 2.7-fold contrast enhancement over normal tissue. This tumor-specific fluorescence signal also appears to mimic that of ^{18}FDG accumulation, at least qualitatively. However, subsequent studies demonstrate a potential size and/or vascularity requirement for appreciable tumor-specific contrast; a larger animal cohort is necessary to establish the precise conditions for significant contrast enhancement. Furthermore, several observations suggest that NIR-glucosamine, like Cy5.5-2DG (12), does not follow the GLUT/hexokinase pathway and may label tumors in a non-specific manner. First, *ex vivo* fluorescence microscopy studies suggest that the NIR-glucosamine and free NIR dye molecules preferentially label necrotic tissue, which may indicate tumor-specific labeling due to the EPR effect (16) rather than cellular uptake and accumulation. Second, *in vitro* competition assays and fluorescence microscopy studies demonstrate that the free NIR dye labels SW480*neo* cells as well or more efficiently than NIR-glucosamine and both compounds appear to localize to the cell membrane. Finally, blood stability analysis and preliminary tissue imaging studies suggest that NIR-glucosamine is not degraded to free NIR dye in blood and appears to be able to extravasate from the vasculature at least in liver, kidneys and lungs.

Overall, NIR-glucosamine and free NIR dye appear to provide enhanced tumor contrast over normal tissues in reasonably sized tumors. Although the mechanism of uptake and accumulation remains unknown, the increased rate of NIR-glucosamine clearance from the normal tissue due to increased polarity may prove beneficial for imaging of vascular permeability and could result in less toxicity. However, additional animal studies are necessary to evaluate the potential advantages of NIR-glucosamine over free NIR dye for tumor labeling.

Acknowledgements

The authors would like to thank Dr. Richard Whitesell and Dr. Al Powers for valuable input and LI-COR Biosciences, Inc. for providing a portion of the dye used in this study. This research was supported by the National Science Foundation (NSF BES-0323281) and National Institutes of Health (NIH P20 GM072048-02).

References

1. Pauwels, E. K. J., Ribeiro, M. J., Stoot, J. H. M. B., McCready, V. R., Bourguignon, M., and Maziere, B. FDG accumulation and tumor biology. Nuclear Medicine and Biology, *25:* 317-322, 1998.

2. Gambhir, S. S. Molecular imaging of cancer with positron emission tomography. Nature Reviews Cancer, *2:* 683-693, 2002.

3. Yoshioka, K., Takahashi, H., Homma, T., Saito, M., Oh, K. B., Nemoto, Y., and Matsuoka, H. A novel fluorescent derivative of glucose applicable to the assessment of glucose uptake activity of Escherichia coli. Biochimica Et Biophysica Acta-General Subjects, *1289:* 5-9, 1996.

4. Yoshioka, K., Oh, K. B., Saito, M., Nemoto, Y., and Matsuoka, H. Evaluation of 2-[N-(7-nitrobenz-2-oxa-1,3-diazol-4-yl)amino]-2-deoxy-D-glucose, a new fluorescent derivative of glucose, for viability assessment of yeast Candida albicans. Applied Microbiology and Biotechnology, *46:* 400-404, 1996.

5. Yoshioka, K., Saito, M., Oh, K. B., Nemoto, Y., Matsuoka, H., Natsume, M., and Abe, H. Intracellular fate of 2-NBDG, a fluorescent probe for glucose uptake activity, in Escherichia coli cells. Bioscience Biotechnology and Biochemistry, *60:* 1899-1901, 1996.

6. Yamada, K., Nakata, M., Horimoto, N., Saito, M., Matsuoka, H., and Inagaki, N. Measurement of glucose uptake and intracellular calcium concentration in single, living pancreatic beta-cells. Journal of Biological Chemistry, *275:* 22278-22283, 2000.

7. Oh, K. B. and Matsuoka, H. Rapid viability assessment of yeast cells using vital staining with 2-NBDG, a fluorescent derivative of glucose. International Journal of Food Microbiology, *76:* 47-53, 2002.

8. O'Neil, R. G., Wu, L., and Mullani, N. Uptake of a fluorescent deoxyglucose analog (2-NBDG) in tumor cells. Molecular Imaging and Biology, *7:* 388-392, 2005.

9. Zhang, M., Zhang, Z. H., Blessington, D., Li, H., Busch, T. M., Madrak, V., Miles, J., Chance, B., Glickson, J. D., and Zheng, G. Pyropheophorbide 2-deoxyglucosamide: A new photosensitizer targeting glucose transporters. Bioconjugate Chemistry, *14:* 709-714, 2003.

10. Zhang, Z. H., Li, H., Liu, Q., Zhou, L. L., Zhang, M., Luo, Q. M., Glickson, J., Chance, B., and Zheng, G. Metabolic imaging of tumors using intrinsic and extrinsic fluorescent markers. Biosensors & Bioelectronics, *20:* 643-650, 2004.

11. Ye, Y. P., Bloch, S., Kao, J., and Achilefu, S. Multivalent carbocyanine molecular probes: Synthesis and applications. Bioconjugate Chemistry, *16:* 51-61, 2005.

12. Cheng, Z., Levi, J., Xiong, Z. M., Gheysens, O., Keren, S., Chen, X. Y., and Gambhir, S. S. Near-infrared fluorescent deoxyglucose analogue for tumor optical imaging in cell culture and living mice. Bioconjugate Chemistry, *17:* 662-669, 2006.

13. Weissleder, R. A clearer vision for in vivo imaging. Nature Biotechnology, *19:* 316-317, 2001.

14. Ke, S., Wen, X. X., Gurfinkel, M., Charnsangavej, C., Wallace, S., Sevick-Muraca, E. M., and Li, C. Near-infrared optical imaging of epidermal growth factor receptor in breast cancer xenografts. Cancer Research, *63:* 7870-7875, 2003.

15. Witty, J. P., Mcdonnell, S., Newell, K. J., Cannon, P., Navre, M., Tressler, R. J., and Matrisian, L. M. Modulation of Matrilysin Levels in Colon-Carcinoma Cell-Lines Affects Tumorigenicity in-Vivo. Cancer Research, *54:* 4805-4812, 1994.

16. Iyer, A. K., Khaled, G., Fang, J., and Maeda, H. Exploiting the enhanced permeability and retention effect for tumor targeting. Drug Discovery Today, *11:* 812-818, 2006.

17. Estensen, R. D. and Plageman.Pg Cytochalasin B: Inhibition of Glucose and Glucosamine Transport. Proceedings of the National Academy of Sciences of the United States of America, *69:* 1430-1434, 1972.

CHAPTER VI

CONCLUSIONS AND FUTURE WORK

Conclusions

The overall objectives of this dissertation were directed at quantitative *in vitro* and *in vivo* characterization of two novel molecular imaging (MI) agents developed in our laboratory: (1) a peripheral benzodiazepine receptor (PBR)-targeted near infrared (NIR) MI agent (NIR-conPK11195) and (2) a potential optical analogue to the 2-[^{18}F]fluoro-2deoxy-D-glucose (^{18}FDG) positron emission tomography (PET) agent. NIR-conPK11195 was evaluated in a subcutaneous MDA-MB-231 breast cancer xenograft model as well as in an intracranial MDA-MB-231 breast cancer model to study breast cancer metastases to the brain; NIR-glucosamine was assessed in an SW480 mouse model of human colon cancer.

Chapter II briefly describes the significance of improved cancer detection methodologies as well as provides a concise overview of relevant topics in the literature. Specifically, the typical detection methods for breast and brain cancer, the clinical applicability of ^{18}FDG-PET, and the recent research efforts regarding optical imaging techniques are discussed. Finally, the rationale for the development of NIR-conPK11195 and NIR-glucosamine are highlighted.

The quantitative evaluation of the *in vitro* and *in vivo* uptake of NIR-conPK11195 in a human metastatic breast adenocarcinoma (MDA-MB-231) model of breast cancer is presented in Chapter III. Fluorescence micrographs illustrate the effective labeling of

MDA-MB-231 cells by NIR-conPK11195. Cellular uptake and competition assays provide further evidence of significant dose-dependent and PBR-specific cellular uptake of NIR-conPK11195. By exploiting the NIR tissue transparency window and conPK11195 specificity, it was possible to preferentially label MDA-MB-231 tumors *in vivo* with an 11-fold contrast enhancement over normal tissue. Furthermore, the fluorescence signal due to NIR-conPK11195 accumulation was up to 7-fold greater than the free NIR dye and demonstrated statistical significance. Overall, our results indicate that NIR-conPK11195 has the potential to be an effective PBR-targeted MI agent for breast cancer screening, while yielding valuable insights regarding the biological development and progression of the disease.

In Chapter IV, two PBR-targeted MI agents were assessed for their applicability to aid in primary brain tumor demarcation (Eu^{3+}-conPK11195) and the study of secondary brain metastases *in vivo* (NIR-conPK11195). Preliminary imaging studies suggest that Eu^{3+}-conPK11195 preferentially bound to the tumor tissue over the contralateral normal brain tissue and may therefore be useful for intraoperative labeling of gliomas. Real-time *in vivo* monitoring of biodistribution over 48 hours post-injection of NIR-conPK11195 or free NIR dye in intracranial MDA-MB-231 tumor-bearing mice demonstrated distinct clearance profiles for the PBR-targeted and non-targeted fluorophores, resulting in preferential labeling of the MDA-MB-231-bearing hemisphere by NIR-conPK11195. Quantification of the tumor-to-normal and PBR-targeted-to-free contrast ratios further indicate that NIR-conPK11195 provides significantly enhanced fluorescence signal over the normal tissue and the non-targeted fluorophore. Combined, these observations indicate that PBR-targeted fluorescent agents may be useful in the management of primary brain tumors and secondary brain metastases.

Chapter V details the extensive *in vitro* and *in vivo* characterization of NIR-glucosamine, particularly in comparison to the GLUT-mediated uptake and hexokinase-specific accumulation of ^{18}FDG. The scientific deductive reasoning involved in these experiments is outlined. Overall, it appears that NIR-glucosamine may not function as an optical analogue to ^{18}FDG and that both NIR-glucosamine and free NIR dye provide enhanced tumor contrast over normal tissues in reasonably sized tumors. Although the mechanism of uptake and accumulation remains unknown, the increased rate of NIR-glucosamine clearance from the normal tissue due to increased polarity may prove beneficial for imaging of vascular permeability and could result in less toxicity. However, additional animal studies are necessary to evaluate the potential advantages of NIR-glucosamine over free NIR dye for tumor labeling.

Future Work

In addition to determining the limitations of these probes (such as the maximum intracranial depth and/or minimum tumor size detectable using NIR-conPK11195) and answering the remaining mechanistic questions regarding NIR-glucosamine uptake and accumulation, the future goals of this research are focused on two main objectives: (1) imaging multiple physiological readouts simultaneously in small animal models and (2) obtaining biologically relevant pharmacokinetic information from dynamic optical image acquisition. Some preliminary efforts towards these aims have recently been completed, but much work remains to accomplish these goals.

The ability to simultaneously monitor multiple optical reporters with different spectroscopic profiles is one major advantage of optical imaging. In an effort to exploit this multicolor capability, our laboratory has developed a toolbox of molecular imaging (MI) compounds targeted to various cellular and intracellular receptors and biological processes. These MI agents target the peripheral benzodiazepine receptor (PBR), epidermal growth factor receptor (EGFr), and vascular endothelial growth factor (VEGF) as well as apoptosis (Annexin-V) and DNA replication (deoxythymidine). By conjugating these ligands or proteins to different near infrared (NIR) fluorophores and capitalizing on the spectral discrimination capabilities of the recently acquired Maestro In Vivo Imaging System (CRi; Woburn, MA), monitoring of multiple physiological readouts becomes possible.

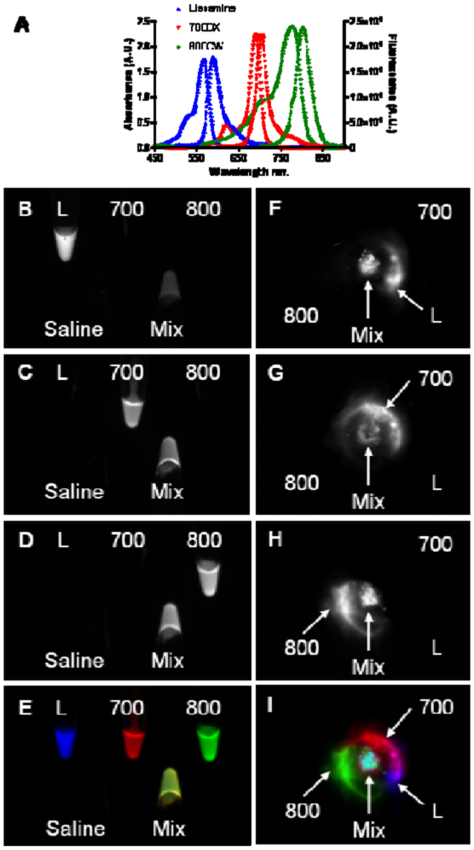

Figure 6.1. Multicolor fluorescence imaging of spectrally overlapping dyes in solution-based and tissue-like phantoms. (A) Optical spectra for Lissamine (L), IRDye 700DX, and IRDye 800CW. (B, F) Lissamine signal, (C,G) 700 signal, (D, H) 800 signal, (E, I) False color composites. Note: Each dye is also resolved in the mixture.

In a preliminary effort to illustrate our spectral discrimination capabilities, a group of solution-based and tissue-like phantoms (1) containing spectrally overlapping fluorescent dyes were imaged on the CRi Maestro. Figure 6.1 shows the excitation and emission spectra for the three dyes used in this study, which included Lissamine, IRDye^{TM} 700DX (LI-COR Biosciences), and IRDye^{TM} 800CW (LI-COR Biosciences). The solution-based (Figure 6.1B-E) and tissue-like phantoms (Figure 6.1F-I) of each dye were imaged separately and as mixtures simultaneously in the Maestro. Using spectral unmixing techniques, we were able to completely resolve the Lissamine (Figure 6.1B,F), IRDye^{TM} 700DX (Figure 6.1C,G), and IRDye^{TM} 800CW fluorescence signal (Figure 6.1D,H) separately and within the mixture in both experiments. The individual signals were subsequently false colorized and overlaid to yield the multi-color composite images seen in Figure 6.1E,I. In a similar study, five NIR dyes (Alexa Fluor 680 (Invitrogen), AlexaFluor 700, Alexa Fluor 750, IRDye^{TM} 700DX, and IRDye^{TM} 800CW) were imaged simultaneously in collaboration with Randy Scherer and Dr. J. Oliver McIntyre. These dyes are more suited for *in vivo* imaging than Lissamine and have considerably overlapping spectroscopic profiles (Figure 6.2A). However, the Maestro's spectral discrimination algorithm was able to distinguish each of these NIR dyes independently (Figure 6.2B, false colorized composite). Given these results, we hypothesize that it will be possible to image multiple optical imaging

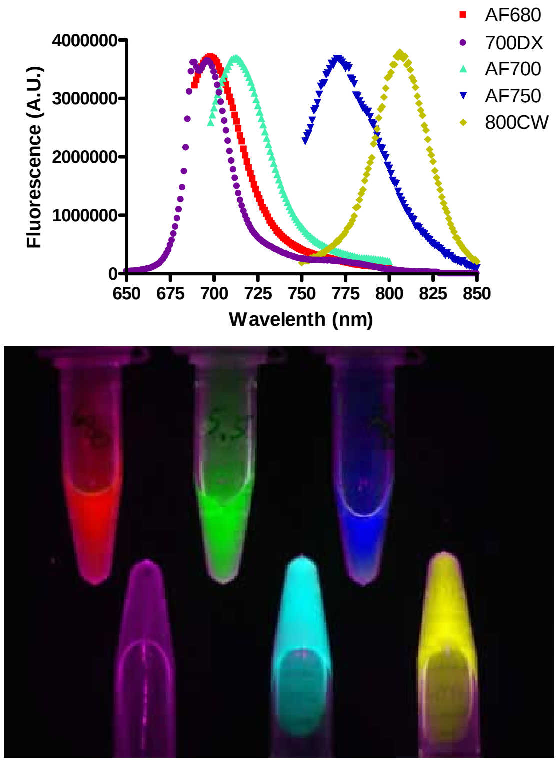

Figure 6.2. Spectral discrimination of five NIR dyes. The fluorescence spectra are color coded according to the spectrally resolved signal in the fluorescence image (one dye per tube; the 6th tube = saline)

probes simultaneously *in vivo*. However, the quantitative implications of this endeavor and the actual performance in a mouse model of disease have not yet been determined.

Another advantage of optical imaging is the short time required to obtain a useful image (on the order of seconds). Capitalizing on this rapidity and the increased photon penetration depth in the near infrared (NIR) tissue transparency window has allowed analysis of indocyanine pharmacokinetics by several groups [for ex. (2, 3)]. Although the determination of true pharmacokinetic parameters represents a technically and mathematically challenging problem, some initial experiments have been completed to investigate the capabilities of obtaining pharmacokinetic data here at the Vanderbilt University Institute of Imaging Science. First, the IVIS Imaging System 200 software was modified to allow image acquisition at an approximately nine-second temporal resolution; a significant improvement over the original 45 seconds – 1 minute duration between images due to filter movement and lamp warm-up. Next, a 12V computer battery was connected to a PicoPlus syringe pump (Harvard Apparatus), which could fit in the IVIS system and was calibrated to deliver 100 μL over 30 seconds. This time frame was chosen based on Dr. Tom Yankeelov’s experience with dynamic contrast enhanced magnetic resonance imaging (DCE-MRI) studies. Micro-renathane tubing was connected from the syringe pump to the jugular vein catheter in the mouse for agent delivery. A carotid artery catheter was also available for blood draws, which allow for input function curve determinations. Figure 6.3 shows an example of dynamic data taken over approximately an hour and a half post-injection of NIR-glucosamine. It is important to note that these data have not been corrected (ie. flat-field, background, dark current, cosmic), but I am currently working with Drs. Brad Rice and Bill Rathbun at Xenogen

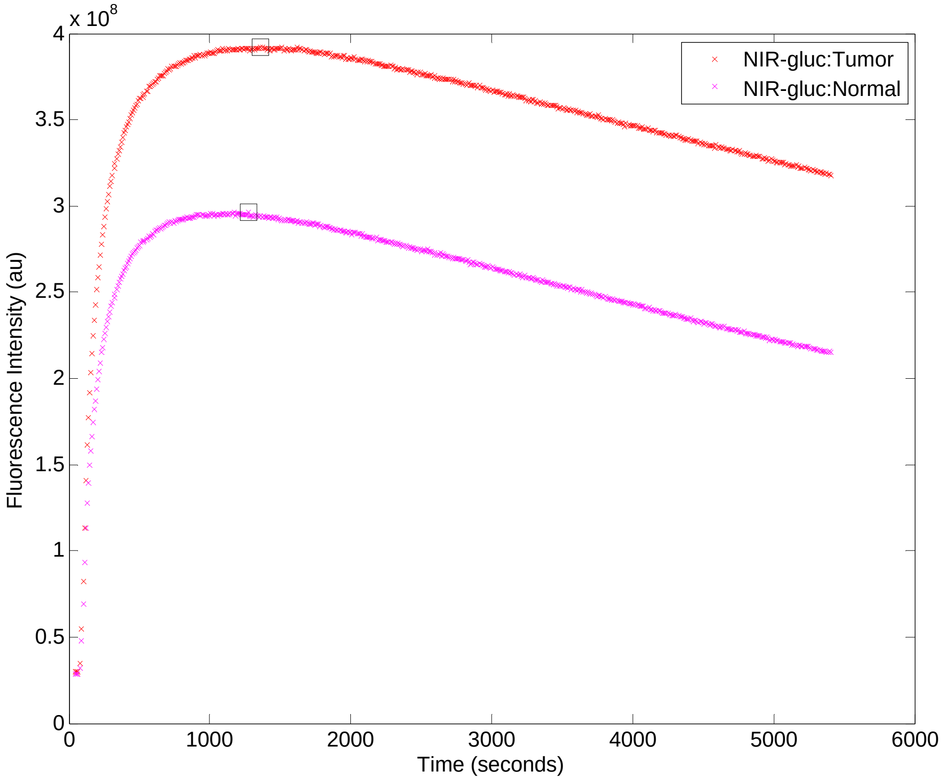

Figure 6.3. Example of dynamic optical imaging obtained in the IVIS Imaging System following syringe-pump assisted injection of NIR-glucosamine.

Corporation/Caliper Life Sciences as well as Dr. Tuhin Sinha to convert these images to calibrated units. Figure 6.4 illustrates an input function curve generated by withdrawing blood from the carotid artery catheter as quickly as possible for the first ~ 4-5 minutes and then approximately every 30 minutes thereafter. Since the blood volume drawn at each time point is only 10 μL, the sample would have to be diluted at least 100-fold to obtain UV-VIS absorption measurements for concentration determination. Thus, I developed a method to use 384-well plates to image the blood samples on the Odyssey Infrared Imaging System (800 nm channel). The fluorescence intensity at each time point can then be converted to approximate blood concentration using a known calibration curve. Although these results are preliminary and do not allow for precise pharmacokinetic data determinations, they may provide a stepping stone for future pharmacokinetic work here at VUIIS.

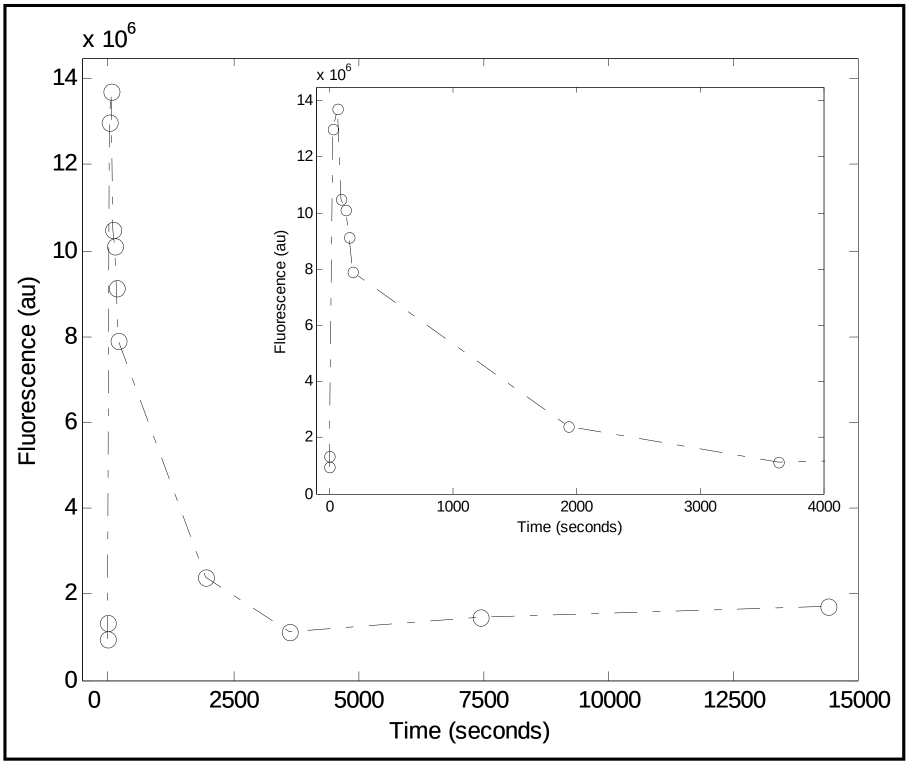

Figure 6.4. Example input function curve obtained from successive carotid artery blood draws following syringe-pump assisted injection of NIR-glucosamine.

References

1. De Grand, A. M., Lomnes, S. J., Lee, D. S., Pietrzykowski, M., Ohnishi, S., Morgan, T. G., Gogbashian, A., Laurence, R. G., and Frangioni, J. V. Tissue-like phantoms for near-infrared fluorescence imaging system assessment and the training of surgeons. Journal of Biomedical Optics, *11:* -, 2006.

2. Gurfinkel, M., Thompson, A. B., Ralston, W., Troy, T. L., Moore, A. L., Moore, T. A., Gust, J. D., Tatman, D., Reynolds, J. S., Muggenburg, B., Nikula, K., Pandey, R., Mayer, R. H., Hawrysz, D. J., and Sevick-Muraca, E. M. Pharmacokinetics of ICG and HPPH-car for the detection of normal and tumor tissue using fluorescence, near-infrared reflectance imaging: A case study. Photochemistry and Photobiology, *72:* 94-102, 2000.

3. Alacam, B., Yazici, B., Intes, X., and Chance, B. Extended Kalman filtering for the modeling and analysis of ICG pharmacokinetics in cancerous tumors using NIR optical method. Ieee Transactions on Biomedical Engineering, *53:* 1861-1871, 2006.